OH-NO Scattering at the Quantum Level

Am Fritz-Haber-Institut
der Max-Planck-Gesellschaft
entstandene und

im Fachbereich Physik
der Freien Universität Berlin
eingereichte Dissertation
von

Moritz Kirste

Berlin, 2012

Erstgutachter:	Prof. Dr. Gerard Meijer Fritz-Haber-Institut der Max-Planck-Gesellschaft Freie Universität Berlin
Zweitgutachter:	Prof. Dr. Drs. h.c. Ludger Wöste Freie Universität Berlin
Disputation:	3. Dezember 2012

Kurzfassung

Während meiner Promotion in der Abteilung Molekülphysik am Fritz-Haber-Institut der Max-Planck-Gesellschaft arbeitete ich im Bereich der Molekülstöße. Molekülstöße sind ein fundamentaler Bestandteil chemischer Prozesse, deren Untersuchung seit Beginn des zwanzigsten Jahrhunderts bis heute dazu beigetragen hat, unser Verständnis der physikalischen Chemie und Molekülphysik zu erweitern und voranzutreiben. In meiner Arbeit habe ich die Methode der sogenannten Stark-Abbremsung mit der wohlbekannten Technik von Kreuzstrahlen kombiniert, um neue Erkenntnisse über inelastische Stöße zwischen Radikalen zu gewinnen.

Zur Stark-Abbremsung benötigt man polare - aber elektrisch neutrale - Moleküle. Diese werden durch Überschallexpansion ins Vakuum expandiert, d.h. in einen Molekülstrahl verwandelt, und einzelne Pakete des Molekülstrahls werden durch periodische, elektrische Felder mittels des Starkeffekts abgebremst. Das Prinzip eines Stark-Abbremsers ist analog zu einem Linearbeschleuniger für geladene Teilchen, mit dem Unterschied, dass die Starkenergie statt der Coulombenergie zur Geschwindigkeitsmanipulation eingesetzt wird. Die besonderen Vorzüge der Stark-Abbremsung sind die Durchstimmbarkeit der mittleren Endgeschwindigkeit und somit der Stoßenergie, die schmale Geschwindigkeitsverteilung, d.h. die hohe Energieauflösung, die Möglichkeit bei sehr langsamen Geschwindigkeiten Stöße mit geringer Energie zu untersuchen und die Selektion eines einzelnen Molekülzustands.

Zu Beginn meiner Dissertation war der Stark-Abbremser bereits vorhanden. In einem ersten Experiment untersuchte ich die Stöße von Hydroxyl-Radikalen (OH) im oberen Λ-Doublet des Grundzustands ($X\,^2\Pi_{3/2}, v = 0, J = 3/2, f$) mit Helium-Edelgasatomen (He), und verglich diese mit den Stößen von Hydroxyl-Radikalen mit Deuterium-Molekülen (D_2). Für dieses Kreuzstrahlexperiment baute ich eine He- bzw. D_2-Molekülstrahlquelle unter 90° zum Abbremser auf und untersuchte die inelastische rotationelle Anregung der Hydroxyl-Radikale zustandsaufgelöst mittels Laser-induzierter-Fluoreszenz (LIF). Die gewonnenen experimentellen, relativen und integralen Streuquerschnitte verglich ich mit ab-initio Streurechnungen. Aufgrund der hohen Stoßenergieauflösung reproduzierte ich den Verlauf und das Schwellwertverhalten der theoretischen Streuquerschnitte. Durch den Vergleich der OH-Stöße mit He bzw. mit D_2 wies ich unterschiedliches Verhalten der beiden Stoßpartner nach. Durch die Analyse der Interaktionspotentiale beschrieb ich diese Unterschiede qualitativ.

Parallel zu meinen ersten Stoßexperimenten konstruierte ich einen elektrostatischen Hexapol für Stickstoffmonoxid-Radikale (NO). Aufgrund des kleinen Dipolmoments des NO (0,16 Debye) legte ich besonderes Augenmerk darauf, hohe elektrische Spannungen (±15 kV) anlegen zu können und den Hexapol gleichzeitig möglichst kurz und kompakt zu dimensionieren. Zu diesem Zweck entwickelte ich ein neues Hexapol-Design, das NO-Moleküle mit einer Zustandsreinheit von 99% im oberen Λ-Doublet des Grundzustands ($X\,^2\Pi_{1/2}, v = 0, J = 1/2, f$) nach nur 30 cm fokussiert, während herkömmliche Hexapol-Designs hierzu mehrere Meter benötigen.

Nach diesen Vorbereitungen wendete ich mich dem Hauptthema meiner Dissertation zu: Inelastische Stöße zwischen Stark-abgebremstem OH ($X\,^2\Pi_{3/2}, v = 0, J = 3/2, f$) und Hexapol-selektiertem NO ($X\,^2\Pi_{1/2}, v = 0, J = 1/2, f$). Hierzu kombinierte ich den vorhandenen Abbremser mit dem neuen Hexapol unter einem Winkel von 90°. Ich variierte die Stoßenergie zwischen 70 und 300 cm^{-1}, und beobachtete das zustandsaufgelöste Schwellwertverhalten von vier Stoßkanälen. Mit der Detektionsmethode der zustandsaufgelösten Laser-induzierter-Fluoreszenz (LIF) bestimmte ich die Partikeldichte der Stoßpartner und zusammen mit Monte-Carlo-Trajektorien-Simulationen beider Molekülstrahlen konnte ich absolute Streuquerschnitte bestimmen. In herkömmlichen Kreuzstrahlexperimenten ist die Dichte und räumliche Verteilung eines der beiden Stoßpartner meist unbestimmt. Trotzdem ist die Bestimmung von absoluten Streuquerschnitten von besonderer Wichtigkeit, da absolute Streuquerschnitte ein essentieller Bestandteil der theoretischen Modelle im Bereich der Verbrennungschemie, Atmosphärenchemie und Astrochemie sind. Die experimentellen Streuquerschnitte verglich ich mit Modellrechnungen über die Stöße zweier $^2\Pi$ Radikale und stellte gute Übereinstimmung fest.

Für das Gelingen dieses Stoßexperiments zweier Moleküle war die hintergrundfreie Detektion von extremer Wichtigkeit. Meine Analyse des Hintergrundsignals im unteren Λ-Doublet des OH-Grundzustands ($X\,^2\Pi_{3/2}, v = 0, J = 3/2, e$) führte zu einem überraschenden Ergebnis: Magnetische Dipolübergänge des gut charakterisierten $A\,^2\Sigma^+ \leftarrow X\,^2\Pi$ Systems des Hydroxyl-Radikals sind zwei Größenordnungen stärker als üblicherweise angenommen. In einem neuen Experiment verglich ich die relative Stärke der magnetischen Dipolübergänge mit der Stärke der elektrischen Dipolübergänge und schloss den Einfluss von elektrischen Quadrupolübergängen aus. Diese experimentellen Erkenntnisse stimmen sehr gut mit neuen theoretischen Rechnungen überein.

Als Abschlussexperiment meiner Dissertation bremste ich das bisher noch nicht Stark-abgebremste NO-Molekül ab. Aufgrund des kleinen Dipolmoments war dies bisher unmöglich. Durch Laseranregung des $A\,^2\Sigma^+ \leftarrow X\,^2\Pi$ Übergangs aus dem Grundzustand ($X\,^2\Pi_{1/2}, v = 0, J = 1/2, f$) und spontane Emission $A\,^2\Sigma^+ \rightarrow X\,^2\Pi$ in das andere Spin-Orbital des Grundzustands ($X\,^2\Pi_{3/2}, v = 0, J = 3/2, f$) wurde dieser Nachteil teilweise ausgeglichen, da die höhere spin-orbit Anregung zu einer größeren Starkenergie führt. Ich verringerte die kinetische Energie der NO-Moleküle um ca. 50%. In Zukunft wird es möglich sein, das wichtige NO-Molekül in Stark-Abbremsern zu manipulieren und z.B. in weiteren Stoßexperimenten zu untersuchen.

In meiner wissenschaftlichen Arbeit ist es mir gelungen, zum ersten Mal zwei Radikale zustandsselektiert zu streuen und deren rotationelle Anregung zustandsaufgelöst zu detektieren. Dieses wichtigste Ergebnis meiner Dissertation wird sicher dazu beitragen, unser Verständnis der physikalischen Chemie und Molekülphysik zu erweitern und voranzutreiben.

Contents

Chapter 1

General introduction

A fellow physicist of mine once asked in front of an audience of pupils the following question: "What would be the most simple way to find out about the nature of any object, presuming you have no tools whatsoever at hand". The answer to this question was, that by taking the object and throwing it on the ground you would learn about the inner structure and the physical properties of the object. This anecdote illustrates the basic idea behind collision studies. A collision is defined as a short duration interaction between two or more bodies, which causes a change in the internal energy of these bodies. The nature of this change of internal energy is defined by the properties of the bodies and therefore by observing - which in an experimental context means measuring - a change of internal energy, much is learned about these properties. The internal energy is divided in translational energy and potential energy. If the magnitude of the translational energy is constant in a collision it is defined as elastic, whereas an inelastic collision is defined as one in which some amount of the energy is interchanged between the translational energy and the potential energy.

One might ask the question how useful are collision experiments for physics research? I believe collisions are one of the most fundamental tools we use to study nature. Even when we are looking at an object, we are conducting a scattering experiment, observing how visible light photons are scattered off the object. Hence, the answer to the question whether collision experiments are useful is a definite yes. Since collision experiments are so useful and have been used in such large numbers, it seems like an impossible endeavour to cover all kinds and applications of collision experiments. Therefore this introduction is restricted to molecular collision experiments.

The term collision and the term scattering are both used to describe the same event. Historically it is more correct to use the term collision for colliding bodies in general, whereas scattering refers to radiation, sound or particles, which are forced to deviate from a straight trajectory by passing through some kind of medium. Still the underlying process is always of the same kind and therefore the term collision and the term scattering are used interchangeably throughout this thesis.

1.1 The early work

Molecular collision experiments rely on the technique of molecular beams. A very interesting review about the early work was written by Immanuel Esterman, who was among the first scientist working with molecular beams in the 1920s [1]. He intended on writing a book on the history of molecular beams before he died in 1973. According to Esterman the technique of molecular beams was pioneered by Dunoyer already in the 1910s [2]. In 1912 Walter Gerlach tried to repeat Dunoyer experiments in Tübingen but did not succeed. But in the 1920s a revival of interest was established by Otto Stern and Walter Gerlach in Frankfurt [3] and independently by Hartmut Kallmann and Fritz Reiche [4] at the Kaiser Wilhelm Institute for Physical Chemistry and Electrochemistry in Berlin; the latter is the predecessor institute to the Fritz Haber Institute, where this thesis is written. No further reports on the work by Kallmann and Reiche are to be found in the literature, while Stern and Gerlach performed their famous experiment in 1922, proving space quantization.

In the early 1930s Stern and co-workers conducted a series of experiments, in which molecular beams of He, H_2 and H were diffracted by single-crystal surfaces [5]. Their interest stemmed from the discussion about the dualism between corpuscles and waves and they managed to confirm the de Broglie formula with an accuracy of about 1%. Within the same group and time the first gas-phase molecular beam scattering experiment was performed [6]. Knauer and Stern measured differential cross sections for the scattering of He, O_2, H_2 and H_2O from their respective gases. In the meantime Broadway conducted an experiment on the scattering of Na and K atoms from Hg vapor effusing from an oven [7], which is regarded as the first crossed beam experiment. In the mid 1930s, due to the political development, the work on molecular beams was delayed or even ceased in Germany. Instead it moved to Columbia University in the US, where experiments on the scattering of alkali atoms with gases were conducted, until the beginning of the second world war [8, 9, 10].

1.2 Classic state-selection and velocity selection

In the 1950s a new era of molecular beams started with the groundbreaking work by Gordon, Zeiger, and Townes [11, 12] and independently Bennewitz, Paul and Schlier [13]. They demonstrated, that an electric quadrupole field can be used to focus a molecular beam by creating a local field minimum on the molecular beam axis. Due to the Stark interaction the molecules are forced either to the field minimum or maximum, depending on their quantum state. In general, any multipole focusing device such as quadrupole [11, 12, 13], hexapole [13, 14] or octupole [15] focusers can be used to increase the local absolute number of molecules, that exhibit a positive Stark shift. But not only did this new technique make more sensitive collision experiments feasible, due to the increased number of molecules, but it also introduced a new method: The state-selection. State-selection is the relative enhancement of a specific quantum state in a molecular beam. Since the collision process does not only depend on the collision energy, but also on the quantum states of the collision partners, it is of interest to study the collision process as a function of the quantum states before and after the collision. In 1961 Toennies measured collision-induced, state-to-state, rotational, inelastic-scattering cross sections for the $\Delta J = 1$ transitions such as $(J, M_J) = (1,0) \rightarrow (2,0)$ and even for $\Delta J = 2$ transitions of Thallium Fluoride (TlF) molecules in collisions with 14 different target atoms and molecules [16, 17]. Toennies used tandem electrostatic quadrupoles before and after the collision to measure, for the first time, quantum state resolved molecular collision processes.

The method of state-selection was immediately combined with the method of orienting molecules in strong electric fields and in 1964 Bennewitz, Kramer, Toennies and Paul measured [18] the angular dependence of the intermolecular potential using preferentially oriented molecules. The new methods of state-selecting and orienting molecules led to a series of experiments studying steric effects in chemical reactions [14, 19, 20, 21]. The steric effect is how the orientation of a colliding molecule effects its chemical reaction. An idealized experiment measuring steric dependencies could for instance be performed in a reaction of an atom and a diatomic molecule: $A + BC$. Orienting the molecule in the experiment with either the B or C end to the colliding atom can lead to different outcomes of the chemical reaction:

$$\begin{aligned} A + BC &\rightarrow AB + C \\ A + CB &\rightarrow AC + B \end{aligned}$$

Prominent collision experiments, using state-selected molecular beams, have been performed on the collisions of hexapole-selected NO radicals by Stolte, Reuss and Schwartz [22, 23]. These experiments revealed the orientational anisotropy in the total collision cross section.

In the 1960s and 1970s a number of techniques, combining or replacing the multipole focusing devices, were studied to focus and state-select molecules in a molecular beam. Moerken et al. applied a RF field to H_2 [24], passing through an arrangement of fields, producing a beam of preferentially oriented molecules. Unfortunately, the absolute number of molecules in this experiment was small compared to the one in the multipole focusing devices. Everdij et al. [25] used a combination of quadrupole and hexapole focusers to compensate for the lens error in a quadrupole, which is caused by the imperfect quadratic Stark effect. But not only molecules with positive Stark shifts were focused, also molecules with negative Stark shifts were focused and selected in different approaches. The technique of alternated gradient focusing was proposed by Auerbach et al. [26] and experimentally realised by Kakati et al. [27]. Other approaches were the crossed-wire focuser by Lainé et al. [28] and a ring type selector by Al-Amiedy et al. [29]. Bobbio et al. used a coaxial beam of electrons to focus a beam of neutral molecules [30].

Not only the quantum state but also the collision energy has been controlled in molecular beam scattering experiments. One approach is to vary the angle of incidence between the colliding particles [31, 32]. Another approach, which has been extensively used, is to select a certain velocity out of the velocity distribution of the molecular beam. For this purpose different types of selectors have been developed [33]. In these velocity selectors a rotating mechanical part is chopping the molecular beam. This mechanical part consists of an arrangement of plates with slits. Only molecules with matching velocities can pass the velocity selector. It is important to note, that these velocity selectors decrease the number density of transmitted molecules.

1.3 Modern crossed molecular beam scattering experiments

A great leap forward in molecular beam scattering came from the development of better hexapole-selectors, increasing the level of state-selection and the absolute number of molecules [34]. Stolte and co-workers for instance have studied the orientation dependence in the reaction $N_2O+Ba\rightarrow BaO^{*}+N_2$, with the use of these improved hexapole-selectors [35]. A wealth of studies using hexapoles to state-select, focus and orient molecules in crossed beam reactive scattering experiments [36] was performed in the 1970s and 1980s, aiming at experiments at the ultimate level at which every reactant and product variable is specified [37].

With the application of laser detection techniques in crossed molecular beam scattering experiments, a versatile, efficient and state-specific detection method was introduced. In particular NO and OH rare gas collision experiments benchmark the scattering of state-selected molecules with rare gas (Rg) atoms [38], and these experiments have strongly influenced our present understanding of how intermolecular potentials govern molecular collision dynamics [39]. Both molecules, the NO radical [40,41,42] and the OH radical [43,44,45,46] have been extensively studied in inelastic collision experiments, revealing for instance quantum interference effects [47,48].

Lasers have not only been used for detection but also for the preparation of molecular states prior to the collision. Bergmann et al. were the first to use a laser for the state-selection in crossed beam scattering experiments [49]. They measured state-resolved differential cross sections for rotational transitions in Na_2+Ne (He) collisions. Recently Wodtke and co-workers introduced a scheme to optically state-select and orient NO molecules without the use of a hexapole selector [50]. And the same group reported experiments in which they combined hexapole focusing with stimulated emission pumping [51,52]. This combination provides control over the molecule's rovibronic quantum state, its velocity and its transverse divergence. Liu and co-workers used a polarized infrared laser to align CH_4 in the reaction $Cl + CH_4(v_3 = 1) \rightarrow HCl + CH_3$ [53]. The direction of the laser polarization leads to end-on attack and side-on attack of the molecules, revealing the stereospecific chemistry of the reaction $Cl + CHD_3(v_1 = 1) \rightarrow HCl + CD_3$ [54].

1.4 Detection methods in crossed molecular beam scattering experiments

Nowadays lasers are routinely used in crossed molecular beam scattering experiments, for the state-specific detection of molecules. The first application of lasers for the detection of reaction products was done by Zare and co-workers [55], on the reaction of $Ba+O_2 \rightarrow BaO+O$. The Laser Induced Fluorescence (LIF) detection technique [56] and the Resonance Enhanced Multi-Photon Ionization (REMPI) detection technique, are the most commonly used detection methods. They both offer the unique abilities of high sensitivity and high selectivity of the detected molecule and its quantum state.

Other laser based detection methods such as ion imaging [57,58,59,60], Rydberg H-atom time of flight (HRTOF) [61,62,63,64], Doppler selected time of flight [65], as well as the photoloc technique [66, 67] are used to analyze the state, angular and velocity distributions of the products after the collision. In these experiments the state-to-state integral and differential cross sections provide a very sensitive probe of the scattering event.

In a scattering experiment one of the most desired quantities to measure is the post-collision velocity of the scattering partners, not only in its magnitude but also in its direction. In 1998, Eppink and Parker [58] developed the velocity mapped ion imaging (VMI) technique. This novel method opened the possibility to measure full velocity distributions. A standard VMI apparatus consists of a molecular beam source, a probe laser and the VMI detector. The laser ionizes the molecules state-selectively, using REMPI, and the ion cloud is transformed to an optical image by the VMI detector. All ions that have the same initial velocity are focused at identical positions in the image, independent of the initial position where they have been ionized. For a system with cylindrical symmetry, the 3D velocity distribution is recovered, using a mathematical transformation known as the Abel inversion. By using time-sliced ion velocity-mapped imaging, the full 3D scattering distribution is retrieved [68]. The VMI technique led to the observation of scattering resonances [69] in the reaction of $F + H_2 \rightarrow HF + H$ [70, 71].

1.5 A new technique of state-selection and velocity manipulation: The Stark decelerator

In classic approaches to state-select and focus molecules, the quadrupole, hexapole and octupole focuser act as a spatial filter or as a lens for particles, influencing only the transversal velocity of the molecular beam. It was not until 1999, that it was experimentally demonstrated that also the longitudinal velocity of a molecular beam can be influenced by electric fields, using a so-called Stark decelerator [72].

The principle of a Stark decelerator [72, 73, 74, 75, 76, 77] is similar to that of a LINAC for charged particles, but instead of the Coulomb energy the Stark energy is used to influence the particles. In a Stark decelerator a molecular beam passes through an array of high voltage electrode pairs. The Stark interaction results in a longitudinal and transversal confining force for the molecules that exhibit a positive Stark shift. The longitudinal force is also used to decelerate or accelerate the molecules, thus resulting in a velocity controlled molecular beam with a narrow velocity distribution. The slope of the Stark shift depends on the quantum state of the molecules, thus similar to a quadrupole, hexapole or octupole focuser, a Stark decelerator is state-selective.

First, Stark decelerators were mainly used for the deceleration and trapping of molecules [75,78]. The long observation time facilitated by these traps was used to directly measure the radiative lifetime of the OH ($X\,^2\Pi_{3/2}, v = 1, J = 3/2$) state, benchmarking the Einstein A coefficients in the Meinel system of OH [79] and for CO the radiative lifetime of metastable CO ($a^3\Pi, v = 0$) [80] was measured. In the near future, comparison of high-resolution spectroscopic data on decelerated and magnetically trapped OH radicals in the laboratory with interstellar megamaser observations may reveal the time variation of fundamental constants [81].

Stark deceleration offers the unique combination of state-selection and a continuous variation of the molecular beam velocity. This offers interesting prospects for collision studies. In the first scattering experiment using a Stark decelerator [82], OH radicals were scattered with a supersonic beam of Xe atoms under 90° angle of incidence. Recently a new, superior Stark decelerator was built [83], and with this decelerator experiments on the system OH-Ar were performed with a better sensitivity [84]. In both systems OH-Xe and OH-Ar the relative inelastic cross sections as a function of the collision energy were measured and clear threshold behavior was observed. The experimental cross sections were compared with cross sections determined by quantum close-coupling calculations based on high-quality ab initio OH-Xe and OH-Ar potential energy surfaces, and excellent agreement was obtained.

In another experimental approach, a Stark decelerator was combined with a static magnetic trap [85] and additional with a hexapole guide [86], measuring OH-He and OH-D_2 collisions and OH-ND_3 collisions, respectively.

The still young technique of Stark deceleration yields unprecedented control over both the internal and external degrees of freedom of polar molecules in a molecular beam. Its combination with state-of-the-art laser detection methods makes crossed molecular beam scattering experiments possible at the ultimate quantum level. In this thesis the technique of Stark deceleration is used for crossed molecular beam scattering experiments.

1.6 This thesis

The ultimate goal of my PhD research project was to conduct an experiment on quantum state resolved collisions of two molecules. Molecule-molecule interactions are of particular fascination, since they are a feature element of most chemical processes. Needless to say, that many chemical reactions need two molecules.

The study of molecule-molecule collisions at the ultimate quantum level has been a quest in molecular collision physics since it was established in the 1950s [87]. Opposed to an atomic target, a molecular scattering partner possesses internal degrees of freedom of its own. A full characterization of bi-molecular collisions offers unique prospects to bring a quantitative description of molecular reaction dynamics from the relatively well understood atom-molecule interactions into the realm of more complex and chemically relevant systems.

The main challenge of state-to-state bi-molecular scattering is the need for reagent beams with sufficient quantum state purity at the densities necessary to observe population transfer in one, or both, reagent beam(s). Thus far, experiments of this kind have only been possible using cryogenically cooled H_2 molecules as a target beam [43, 88].

The theoretical study of molecule-molecule collisions has been equally challenging. Whereas atom-molecule scattering cross sections can now be calculated routinely in excellent agreement with experiment [84, 89], much less is known about rotational energy transfer in molecule-molecule collisions [90]. As opposed to an atomic target, a molecular scattering partner possesses internal degrees of freedom of its own, adding a level of complexity that can easily render ab initio quantum scattering calculations extremely challenging, if not impossible. Experimental data on bi-molecular state-to-state cross sections is generally lacking, and kinetic models often use collision rate coefficients that are expected to be inaccurate [91].

Based on the interest in molecule-molecule collisions, it was decided to conduct a bi-molecular scattering experiment during my PhD, using a Stark decelerator.

1.7 Outline

This thesis is organized as follows. In Chapter 2 the theoretical and experimental methods are discussed. The following five Chapters report on the experiments I conducted during my PhD.

At the beginning of my PhD the Stark decelerator was already present. In first experiments, the collisions between OH radicals in the upper Λ-doublet of the electronic ground state ($X\,^2\Pi_{3/2}, v = 0, J = 3/2, f$) with He are compared with collisions between OH ($X\,^2\Pi_{3/2}, v = 0, J = 3/2, f$) and D_2. This experiment in reported in Chapter 3. For this experiment a molecular beam source is set up under 90° to the decelerator and the rotational excitation of the OH radicals is studied, using Laser Induced Fluorescence. The cross sections are compared with ab-initio close-coupled scattering calculations.

Simultaneously to the OH-He and OH-D_2 scattering experiments a electrostatic hexapole for NO has been designed. The new hexapole design is reported in Chapter 4. It focuses and state-selects NO radicals with a state purity of 99% in the upper Λ-doublet of the electronic ground state ($X\,^2\Pi_{1/2}, v = 0, J = 1/2, f$) after only 30 cm.

After these preparations, the main topic of this thesis is reported in Chapter

5: The inelastic scattering of Stark-decelerated OH $(X\,^2\Pi_{3/2}, v = 0, J = 3/2, f)$ and hexapole-selected NO $(X\,^2\Pi_{1/2}, v = 0, J = 1/2, f)$. For this experiment the Stark decelerator is combined with the new hexapole under an angle of incidence of 90°. The collision energy is varied by tuning the OH velocity with the Stark decelerator. The OH collision products are state-selectively detected using Laser Induced Fluorescence. With the help of Monte-Carlo trajectory simulations of both molecular beams an absolute scattering cross section is determined.

In a follow-up experiment, reported in Chapter 6, the ratio between electric dipole allowed and magnetic dipole allowed transitions in the well characterized $A\,^2\Sigma^+ \leftarrow X\,^2\Pi$ system of the important OH radical is measured and compared to the outcome of theoretical calculations.

The last experiment, reported in Chapter 7, is the first deceleration of NO radicals. For this purpose the NO radicals are pumped from the lower Λ-doublet of the electronic ground state $(X\,^2\Pi_{1/2}, v = 0, J = 1/2, e)$ to the lowest rotational level $(X\,^2\Pi_{3/2}, J = 3/2)$ of the other spin-orbit manifold.

Chapter 2

Methods

For a good understanding of the experimental results a thorough understanding of the theoretical and experimental methods is essential. This chapter contains a general discussion of the energy level structure of diatomic molecules. The concepts are then applied to the OH and the NO radical, and their Stark effect is described. After this introduction of the theoretical methods all experimental methods used in this thesis are discussed. Each part of the molecular beam apparatus is described in a unique section, structured from the production of a molecular beam to the detection. The theoretical and experimental background introduced in this chapter is used in the entire thesis.

2.1 Energy levels of a diatomic molecule

Following the Born-Oppenheimer approximation, the total wavefunction of a diatomic molecule can be written as the product of an electronic wavefunction and a wavefunction describing the nuclear motion [92]. The movement of the electron distribution leads to an electronic orbital angular momentum $\boldsymbol{L}$ and electronic spin angular momentum $\boldsymbol{S}$. In a diatomic molecule the internuclear axis acts as a symmetry axis and the projections of $\boldsymbol{L}$ and $\boldsymbol{S}$ on the internuclear axis are defined as Λ and Σ, respectively [93]. The electronic state of a molecule is described by the term symbol ${}^{2\Sigma+1}\Lambda$. Both angular momenta $\boldsymbol{L}$ and $\boldsymbol{S}$ depend on the orbital angular momentum and spin of each individual electron in the molecule, i.e. the molecular orbitals these electrons occupy. Two equivalent approaches exist to describe how electrons occupy the molecular orbitals: the united atom picture and the seperated atom picture. Both lead to the same electronic state of the molecule. In addition to the electronic motion, a molecule exhibits vibrational and rotational motion of the nuclei, described by ν and the rotational angular momentum $\boldsymbol{R}$ respectively. The vibration and the total rotation are coupled. This is incorporated by the vibration dependence of the rotational constants. All angular momenta couple together to a total angular momentum describing the total rotation of the molecule. The coupling of the rotation of the nuclei and the angular momenta of the electronic state are described by the so called Hund's cases [94]. In general five Hund's cases, i.e. case (a) to (e), can be defined by their good quantum numbers, but this work is limited to the most important ones: Hund's cases (a) and (b), Figure 2.1.

2.1.1 Hund's case (a) coupling scheme

In Hund's case (a) the orbital angular momentum $\boldsymbol{L}$ and electronic spin angular momentum $\boldsymbol{S}$ are each strongly coupled to the internuclear axis. Their projections on the internuclear axis form the total electronic angular momentum $\boldsymbol{\Omega} = \boldsymbol{\Lambda} + \boldsymbol{\Sigma}$, which takes the values $\pm\Omega$. The nuclear angular momentum $\boldsymbol{R}$ couples to the orbital angular momentum $\boldsymbol{L}$ and the spin angular momentum $\boldsymbol{S}$ to form the total angular momentum $\boldsymbol{J}$:

$$\boldsymbol{J} = \boldsymbol{R} + \boldsymbol{L} + \boldsymbol{S}. \tag{2.1}$$

Now the good quantum numbers are defined: $\nu, \Lambda, S, \Sigma, J, \Omega$. The Hund's case (a) wavefunctions are separated in four parts. The electronic orbital part $|n\Lambda\rangle$, the electronic spin part $|S\Sigma\rangle$, the vibrational part $|\nu\rangle$, and the rotational part $|J\Omega M\rangle$ [93]:

$$\left|\Psi(n^{2S+1}\Lambda_\Omega\, \nu J M)\right\rangle = |n\,\Lambda\rangle\, |S\,\Sigma\rangle\, |\nu\rangle\, |J\,\Omega\,M\rangle = |n\,\Lambda; S\,\Sigma; \nu; J\,\Omega\,M\rangle\,, \tag{2.2}$$

where n denotes all other quantum numbers not expressed explicitly and M represents the projection of J on an external quantization axis. Such an external quantization axis could be given, for instance, by the direction of an electric or

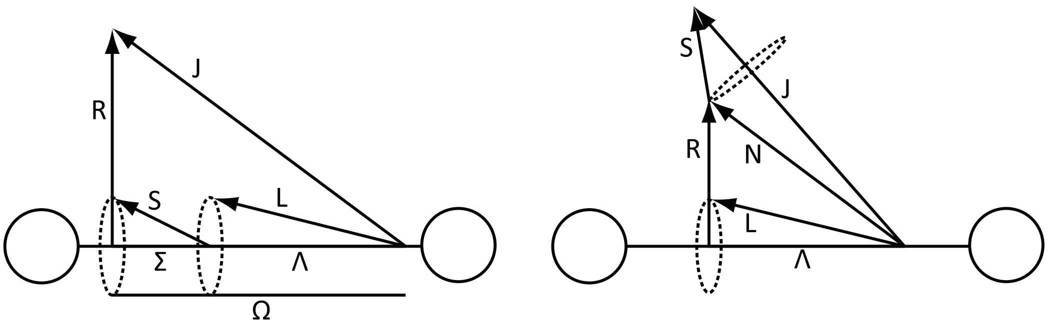

Figure 2.1: Hund's case (a) (left panel) Hund's case (b) (right panel) coupling schemes of a diatomic molecule.

magnetic field and is commonly space fixed. When no external quantization axis is present, the wavefunctions are degenerate in M. To calculate the energy of the rotational part, the rotational Hamiltonian has to be established:

$$\boldsymbol{H}_\nu^{rot} = B_\nu(\boldsymbol{J} - \boldsymbol{L} - \boldsymbol{S})^2 + A_\nu \boldsymbol{L} \cdot \boldsymbol{S}. \tag{2.3}$$

The first term represents the rotation while the second considers the spin-orbit coupling. The two constants B_ν and A_ν are called rotational constant and spin-orbit coupling constant, respectively. For each electronic state a set of these constants exists, that depends on the vibrational state, represented by the vibrational quantum number ν. The diagonalization of $\boldsymbol{H}_\nu^{rot}$ leads to the correct eigenstates and energies of the rotational states. For a diatomic molecule these eigenstates can be expressed as the rigid body rotational basis wavefunctions [95]:

$$|J\Omega M\rangle = \sqrt{\frac{2J+1}{8\pi^2}} D^{J*}_{\Omega,M}(\phi,\theta,0), \tag{2.4}$$

where $D^{J*}_{\Omega,M_J}(\phi,\theta,0)$ is the Wigner function in terms of the Euler angles ϕ and θ. The third Euler angle χ is set to zero to account for the fact that the molecule-fixed y-axis lies in the plane of rotation while the molecule-fixed x-axis is perpendicular to the plane of rotation.

2.1.2 Hund's case (b) coupling scheme

If the coupling of the spin $\boldsymbol{S}$ to the internuclear axis is weak, or in the case $\Lambda = 0$, the spin-orbit coupling vanishes and Ω is not defined anymore. Now $\boldsymbol{\Lambda}$ and $\boldsymbol{R}$ couple to form the angular momentum $\boldsymbol{N}$, which then couples with $\boldsymbol{S}$ to form the total angular momentum $\boldsymbol{J}$.

$$\boldsymbol{J} = \boldsymbol{N} + \boldsymbol{S}. \tag{2.5}$$

The good quantum numbers are: ν, Λ, N, S, J, and the Hund's case (b) wavefunctions take the form:

$$\left|\Psi(n^{2S+1}\Lambda\,\nu JM)\right\rangle = |n\,\Lambda\rangle\,|\nu\rangle\,|N\,\Lambda\,S\,J\,M\rangle = |n\,\Lambda;\nu;N\,\Lambda\,S\,J\,M\rangle\,. \tag{2.6}$$

The rotational energy of a Hund's case (b) molecule is calculated from the sum representing the rotational energy and the spin-rotation coupling:

$$\boldsymbol{H}_\nu^{rot} = B_\nu \boldsymbol{R}^2 + \gamma_\nu \boldsymbol{N} \cdot \boldsymbol{S} = B_\nu [\boldsymbol{N} - \boldsymbol{L}]^2 + \gamma_\nu \boldsymbol{N} \cdot \boldsymbol{S}. \tag{2.7}$$

B_ν is again the rotational constant and γ_ν the spin-rotation coupling constant. For the special case of $S = \frac{1}{2}$ the influence of the spin-rotation coupling results in a splitting of each rotational level, which is referred to as ρ-doubling.

2.1.3 Intermediate coupling

For most molecules the Hund's cases are idealized descriptions and in general strictly apply to only a few specific electronic states of a molecule. Moreover, the best description of the coupling often changes when the molecular rotation changes. In these cases an intermediate coupling, that involves more than one Hund's case has to be chosen. Nevertheless it simplifies the analysis to label the energy levels of a molecule with the most appropriate coupling case and to calculate its energy in a basis set, in which the Hamiltonian is closest to being diagonal. It is always possible to express one Hund's case in terms of another one [93].

2.1.4 Symmetry in a diatomic molecule

In the description and analysis of molecular spectra and energy levels the concept of symmetry has proven to be very powerful [96]. By labeling molecular energy levels with their symmetry, it is for example possible to quickly distinguish between electric-dipole allowed and electric-dipole forbidden transitions between these levels. Although the concept of symmetry has proven to be so powerful, much confusion arises from the different symmetry operations and the notation of the property of these symmetry operations, the so called parity. There are many different types of parity, such as g/u, +/-, e/f, and s/a [93], but this analysis is restricted to only +/- parity and e/f spectroscopic parity, because they apply to diatomic molecules. The concept of symmetry is the following: If a symmetry operator $\boldsymbol{S}$ commutes with the Hamiltonian $\boldsymbol{H}$ of a molecule, i.e. $[\boldsymbol{H}, \boldsymbol{S}] = 0$, then a set of simultaneous eigenfunctions can be found [96]. If the eigenvalues of these operators are:

$$\boldsymbol{H} \left|\Psi_\pm\right\rangle = E \left|\Psi_\pm\right\rangle \tag{2.8}$$

$$\boldsymbol{S} \left|\Psi_\pm\right\rangle = \pm \left|\Psi_\pm\right\rangle \tag{2.9}$$

then the symmetry operator $\boldsymbol{S}$ is called a parity operation, and its eigenvalues are used to label the energy levels of the molecule. Total parity, that is +/- parity, is defined as the symmetry of the total electronic wavefunction upon inversion of the coordinates of all particles, in a space fixed coordinate system, with the origin in the center of mass. The total electronic wavefunction is the product of the vibrational, rotational and electronic part, hence the total parity depends on the symmetry of each part. The nuclear spin is not included in this symmetry operation. The operator of this space fixed inversion is $\boldsymbol{E}^*$, with the relations:

$$\boldsymbol{E}^* f(x,y,z) = f(-x,-y,-z) \tag{2.10}$$

$$\boldsymbol{E}^* \left|\Psi_\pm\right\rangle = \pm\left|\Psi_\pm\right\rangle . \tag{2.11}$$

With these properties the effect of $\boldsymbol{E}^*$ on the Hund's case (a) and (b) wavefunctions is studied. For this purpose the effect of $\boldsymbol{E}^*$ on each part of Ψ in the product basis set has to be calculated [93]. Here only the results are given. For a Hund's case (a):

$$\boldsymbol{E}^* \left|n\,\Lambda; S\,\Sigma; \nu; J\,\Omega\,M\right\rangle = (-1)^p \left|n\ -\Lambda; S\ -\Sigma; \nu; J\ -\Omega\,M\right\rangle \tag{2.12}$$

with $p = J - S + s$, and for Hund's case (b):

$$\boldsymbol{E}^* \left|n\,\Lambda; \nu; N\,\Lambda\,S\,J\,M\right\rangle = (-1)^{N+s} \left|n\ -\Lambda; \nu; N\ -\Lambda\,S\,J\,M\right\rangle . \tag{2.13}$$

Note that for a Σ^- electronic state $s = 1$ and for Σ^+ and all other electronic states with $\Lambda > 0$, $s = 0$. From these equations it is obvious, that the Hund's case (a) and (b) wavefunctions are not eigenfunctions of $\boldsymbol{E}^*$, i.e. they do not have a defined parity. Instead, a linear combination of these wavefunctions is more convenient. For Hund's case (a):

$$\begin{aligned} \left|n\,\Lambda; S\,\Sigma; \nu; J\,\Omega\,M; \pm\right\rangle =& \frac{1}{\sqrt{2}}(\left|n\,\Lambda; S\,\Sigma; \nu; J\,\Omega\,M\right\rangle \\ & \pm (-1)^p \left|n\ -\Lambda; S\ -\Sigma; \nu; J\ -\Omega\,M\right\rangle), \end{aligned} \tag{2.14}$$

and for Hund's case (b):

$$\begin{aligned} \left|n\,\Lambda; \nu; N\,\Lambda\,S\,J\,M; \pm\right\rangle =& \frac{1}{\sqrt{2}}(\left|n\,\Lambda; \nu; N\,\Lambda\,S\,J\,M\right\rangle \\ & \pm (-1)^{N+s} \left|n\ -\Lambda; \nu; N\ -\Lambda\,S\,J\,M\right\rangle). \end{aligned} \tag{2.15}$$

Note that these wavefunctions are not labeled with the total parity but with the sign in the linear combination. The total parity of these wavefunctions, which can be used to label the molecular levels is given by:

$$\text{total parity} = (-1)^p \qquad \text{Hund's case (a)} \tag{2.16}$$

$$\text{total parity} = (-1)^{N+s} \qquad \text{Hund's case (b).} \tag{2.17}$$

Since the factor $(-1)^p$ in Equation 2.14 alternates with J, the spectroscopic parity labels e and f are introduced [97]. The convention is the following: For integral J, levels with parity $(-1)^J$ and for half integral J levels with $(-1)^{J-1/2}$ are labeled with e, whereas f is designated to levels with parity $(-1)^{J+1}$ for integral J and $(-1)^{J+1/2}$ for half integral J levels, respectively.

Up to this point the levels described with the $\left|n\,\Lambda; S\,\Sigma; \nu; J\,\Omega\,M; \pm\right\rangle$ basic wavefunctions for the Hund's case (a) are degenerate. As will be seen later, this degeneracy is lifted if second order effects in the Hamiltonian are taken into account, creating the so-called Λ-doublet splitting.

2.2 Application to OH and NO

After this general introduction to diatomic molecules, in this section these concepts are applied to two very prominent diatomic molecules: the OH and the NO radical.

2.2.1 The electronic ground state $^2\Pi$

The OH radical has nine electrons. The ground state forms, in the united atom picture, a $(1s\sigma)^2$ $(2s\sigma)^2$ $(2p\sigma)^2$ $(2p\pi)^3$ configuration. The missing electron to a closed $(2p\pi)$ shell results in a nonzero electronic orbital angular momentum $\boldsymbol{L}$ and electronic spin angular momentum $\boldsymbol{S}$. The resulting term symbol is $^2\Pi$. For low rotational states OH is almost a clear Hund's case (a) [92], hence Ω can take the values $\frac{3}{2}$ and $\frac{1}{2}$, and the ground state consists of two spin-orbit states $^2\Pi_{3/2}$ and $^2\Pi_{1/2}$, separated by approximately 126 cm^{-1}. These two manifolds are in the literature often designated as F_1 and F_2, respectively. According to Hund's rules the $^2\Pi_{3/2}$ (F_1) manifold is lower in energy, leading to an absolute ground state labeled: $^2\Pi_{3/2}, J = 3/2$, Figure 2.2. For higher rotational states the OH molecule is better described as an intermediate Hund's case molecule.

The NO radical has fifteen electrons, forming, in the ground state, a $(1s\sigma)^2$ $(2s\sigma)^2$ $(2p\sigma)^2$ $(2p\pi)^4$ $(3s\sigma)^2$ $(4s\sigma)^2$ $(3p\pi)^1$, again open shell configuration. Consequently the ground state has also two spin-orbit states: $^2\Pi_{3/2}$ and $^2\Pi_{1/2}$. They are separated by approximately 125 cm^{-1}, and more importantly: in contrast to OH, the $^2\Pi_{1/2}$ spin-orbit manifold is lower in energy, which results for NO in a ground state with $^2\Pi_{1/2}, J = 1/2$. Similar to the labeling in OH, the $^2\Pi_{1/2}$ manifold, i.e. the one being lower in energy, is labeled with F_1, and $^2\Pi_{3/2}$ with F_2, Figure 2.3.

For both molecules the Hamiltonian $\boldsymbol{H}_\nu^{rot}$ mixes basis wavefunctions with different values of Ω, i.e. the parity adapted Hund's case (a) wavefunctions from Equation 2.14 are no longer eigenfunctions. The Hamiltonian no longer diagonalizes. Instead, new eigenfunctions of $\boldsymbol{H}_\nu^{rot}$ are given by a sum of the parity adapted wavefunctions from Equation 2.14, with the mixing coefficients C_1 and C_2:

$$
\begin{aligned}
|^2\Pi; F_1, \nu, J, M; \pm\rangle =& C_1(J)\, |n\, 1; \frac{1}{2}\, \frac{1}{2}; \nu; J\, \frac{1}{2}\, M; \pm\rangle \\
&+ C_2(J)\, |n\, 1; \frac{1}{2}\, \frac{1}{2}; \nu; J\, \frac{3}{2}\, M; \pm\rangle \\
|^2\Pi; F_2, \nu, J, M; \pm\rangle =& - C_2(J)\, |n\, 1; \frac{1}{2}\, \frac{1}{2}; \nu; J\, \frac{1}{2}\, M; \pm\rangle \\
&+ C_1(J)\, |n\, 1; \frac{1}{2}\, \frac{1}{2}; \nu; J\, \frac{3}{2}\, M; \pm\rangle\,. \qquad (2.18)
\end{aligned}
$$

The mixing coefficients take the values:

$$C_1(J) = \sqrt{\frac{X_\nu + Y_\nu - 2}{2X_\nu}} \tag{2.19}$$

$$C_2(J) = \sqrt{\frac{X_\nu - Y_\nu + 2}{2X_\nu}} \tag{2.20}$$

with

$$X_\nu = \sqrt{4(J + \frac{1}{2})^2 + Y_\nu(Y_\nu - 4)} \tag{2.21}$$

and

$$Y_\nu = \frac{A_\nu}{B_\nu}. \tag{2.22}$$

For low values of J the degree of mixing is low, which explains the almost Hund's case (a) behavior of the OH ground state and justifies the labeling of the eigenfunctions with F_1 and F_2 following Hund's case (a) nomenclature. The NO ground state $^2\Pi_{1/2}, J = 1/2$ is a pure Hund's case (a) state with $C_1 = 1$ and $C_2 = 0$. Note that if $Y_\nu = 2$, the mixing coefficients are independent of J, with $C_1 = C_2 = 1/2\sqrt{2}$. This is nearly the case, for instance, for the electronic ground state $X\,^2\Pi$ of the CH radical, which has $Y_0 \approx 1.99$.

The energies of the $^2\Pi$ rotational states are [95]:

$$E(^2\Pi, F_1, \nu, J, \pm) = B_\nu[(J - \frac{1}{2})(J + \frac{3}{2}) - \frac{1}{2}X_\nu] \tag{2.23}$$

$$E(^2\Pi, F_2, \nu, J, \pm) = B_\nu[(J - \frac{1}{2})(J + \frac{3}{2}) + \frac{1}{2}X_\nu], \tag{2.24}$$

with X_ν as defined in 2.21. The rotational constant B_ν and the spin-orbit coupling constant A_ν for the ground state $^2\Pi$ of both molecules, OH and NO, are found in table 2.1, together with other important parameters .

As mentioned above, each rotational level with the parity ± or e/f is still doubly degenerate. The degeneracy is lifted by taking the gyroscopic effect of $\boldsymbol{J}$ on $\boldsymbol{S}$ and $\boldsymbol{L}$ into account, which leads to non-zero off-diagonal elements in the Hamiltonian [98]. These additional second order effects originate from a mixing between the electronic ground state $^2\Pi$ and the first electronically excited state $^2\Sigma^+$ [93]. Each rotational level in a $^2\Sigma^+$ state has a defined parity and interacts therefore with only one of the two degenerate components with the same parity, shifting it upwards or downwards in energy. This shift results in the Λ-doublet with the lower state having always e-parity and the upper f-parity. The Λ-doublet splitting is much smaller than the rotational spacing. For OH in the ground state $^2\Pi_{3/2}, J = 3/2$ the splitting is 0.055 cm^{-1} [99], and for NO in the ground state $^2\Pi_{1/2}, J = 1/2$ the splitting is 0.0118 cm^{-1} [100, 101].

2.2.2 The first excited electronic state $^2\Sigma^+$

For the OH and the NO radical the first electronically excited state is a $A^2\Sigma^+$ state, where the $^+$ indicates the symmetry of the electronic orbital function [93]. This state with $\Sigma = \frac{1}{2}$ and $\Lambda = 0$ is of type Hund's case (b). Using the basic case (b) wavefunctions from Equation 2.15 and with the help of the Hamiltonian of a Hund's case (b) molecule, Equation 2.7, which involves spin rotation coupling the energies are calculated [95]:

$$E(^2\Sigma^+; \nu, N; +) = B_\nu N(N+1) + \frac{1}{2}\gamma_\nu N, \tag{2.25}$$

when $J = N + \frac{1}{2}$, and

$$E(^2\Sigma^+; \nu, N; -) = B_\nu N(N+1) - \frac{1}{2}\gamma_\nu (N+1), \tag{2.26}$$

when $J = N - \frac{1}{2}$. The levels with $J = N + \frac{1}{2}$ are called F_1 and the levels with $J = N - \frac{1}{2}$ are called F_2. Note that this is a different labeling from the one in the ground state. The splitting between F_1 and F_2 of $\frac{1}{2}\gamma\nu(2N+1)$ is called the ρ-doubling. In the excited state the parity serves again as a useful labeling for the molecular levels. The parity of the rotational levels is given by:

$$^2\Sigma^+\text{-total parity} = (-1)^N. \tag{2.27}$$

For the vibrational ground state of OH ($^2\Sigma^+$), the rotational constant B_0 and the spin rotation coupling constant γ_0 take the values 16.961 cm^{-1} [102] and 0.226 cm^{-1} [103,104], respectively. For the vibrational ground state of NO ($^2\Sigma^+$) these constants take the values $B_0 = 1.986289$ cm^{-1} and $\gamma_0 = -2.37 \cdot 10^{-3}$ cm^{-1} [105].

2.2.3 Hyperfine structure

The nuclei of the molecules can exhibit a non-vanishing total nuclear spin $\boldsymbol{I}$. The nuclear spin couples with the total angular momentum $\boldsymbol{J}$ to the total angular momentum $\boldsymbol{F}$:

$$\boldsymbol{F} = \boldsymbol{J} + \boldsymbol{I} \tag{2.28}$$

For OH and NO in the electronic ground state, the hyperfine interaction leads to a splitting of each Λ-doublet component. For both radicals the eigenfunctions $|^2\Pi; F_{1,2}, J, M; \pm\rangle$ of $\boldsymbol{H}_\nu^{rot}$ given in Equation 2.18 need to be expanded by a hyperfine part:

$$|^2\Pi; F_{1,2}, J, M, I, F, M_F; \pm\rangle \tag{2.29}$$

^{16}OH is the most abundant isotopomer of the OH radical. The oxygen has no nuclear spin and the hydrogen has a nuclear spin of $I = 1/2$. For the $^2\Pi_{\frac{3}{2}}$, $J = 3/2$

ground state this leads to a total angular momentum of $F = 1$ and $F = 2$, with a M_F degeneracy of $(2F + 1)$. Hence, the OH ground state splits in a set of four hyperfine levels, two for each Λ-doublet component. The splitting between the different OH hyperfine levels is found in [106] and with improved accuracy in [81].

In NO the most abundant isotopomer is $^{14}N^{16}O$. Nitrogen has a nuclear spin of $I = 1$. The total angular momentum of the $^2\Pi_{1/2}, J = 1/2$ ground state takes the values $F = 1/2$ and $F = 3/2$. Similar to OH the NO ground state also splits in a set of four hyperfine levels and these splitting have been measured in [101].

2.2.4 The $A\,^2\Sigma^+ \leftarrow X\,^2\Pi$ transition

The $A\,^2\Sigma^+ \leftarrow X\,^2\Pi$ transition is often used for the detection of OH and NO. For an electric dipole allowed (EDA) transition the selection rules are [92]:

$$\Delta J = 0, \pm 1 \quad J = 0 \not\leftrightarrow J = 0 \tag{2.30}$$

$$\Delta N = 0, \pm 1, \pm 2, \pm 3 \quad \text{for } \Sigma\text{-}\Sigma \text{ transitions: } \Delta N \neq 0 \tag{2.31}$$

$$\Delta\Lambda = 0, \pm 1 \tag{2.32}$$

$$\Delta S = 0 \tag{2.33}$$

$$\Delta\Sigma = 0 \tag{2.34}$$

$$(+) \leftrightarrow (-) \quad \text{total parity has to change} \tag{2.35}$$

$$\Delta F = 0, \pm 1 \quad F = 0 \not\leftrightarrow F = 0 \tag{2.36}$$

Note that Equation 2.30, 2.36 and 2.35 are independent of Hund's cases. Because of historic reasons, in this thesis the electric dipole allowed transitions in OH are labeled using the nomenclature of Dieke and Crosswhite [102],

$$\Delta N_{F'F''}(N'') \quad \text{(labeling for OH EDA transitions)}, \tag{2.37}$$

where P, Q and R are used to label transitions with $\Delta N = -1, 0, +1$, respectively. N'' is the value of the quantum number N in the $X\,^2\Pi$ state, F' denotes the ρ-doublet in the $A\,^2\Sigma^+$ state and F'' the spin-orbit manifold in the $X\,^2\Pi$ state. This F' and F'' should not be confused with the hyperfine quantum number F. As a convention, only one subscript is used, when $F' = F''$.

The labeling for the EDA transitions in NO is different from the one in OH, although the transitions are similar. Instead of the quantum number N in NO the quantum number J is used for the labeling. EDA transitions are labeled by:

$$\Delta J_{F'F''}(N'') \quad \text{(labeling for NO EDA transitions)}, \tag{2.38}$$

where P, Q and R are used to label transitions with $\Delta J = -1, 0, +1$, respectively. N'', F' and F'' are used equivalent to OH, and when $F' = F''$ one subscript is dropped.

In addition to electric dipole transitions a molecule also exhibits magnetic dipole allowed (MDA) transitions and even electric quadrupole (EQA) allowed transitions. In Chapter 6 of this thesis the measurement of magnetic dipole allowed transitions in OH is discussed. Generally MDA and EQA transitions are believed to be at least five orders of magnitude smaller than EDA transitions [107]. Nevertheless they have been observed [108, 109, 110, 111, 112] and in some examples affected the interpretation of population measurements [113, 114]. The selection rules for an MDA transition are [92, 115]:

$$\Delta J = 0, \pm 1 \quad J = 0 \not\leftrightarrow J = 0 \tag{2.39}$$

$$\Delta N = 0, \pm 1, \pm 2, \pm 3 \quad \text{for } \Sigma\text{-}\Sigma \text{ transitions: } \Delta N \neq 0 \tag{2.40}$$

$$\Delta \Lambda = 0, \pm 1 \tag{2.41}$$

$$\Delta S = 0 \tag{2.42}$$

$$\Delta \Sigma = 0 \tag{2.43}$$

$$(+) \leftrightarrow (+), (-) \leftrightarrow (-) \quad \text{total parity is conserved} \tag{2.44}$$

$$\Delta F = 0, \pm 1 \quad F = 0 \not\leftrightarrow F = 0. \tag{2.45}$$

And for an EQA transition the selection rules are [92, 115]:

$$\Delta J = 0, \pm 1, \pm 2 \quad J = 0 \not\leftrightarrow J = 0, 1 \quad J = \frac{1}{2} \not\leftrightarrow J = \frac{1}{2} \tag{2.46}$$

$$\Delta N = 0, \pm 1, \pm 2, \pm 3 \quad \text{for } \Sigma\text{-}\Sigma \text{ transitions: } \Delta N \neq 0 \tag{2.47}$$

$$\Delta \Lambda = 0, \pm 1, \pm 2 \tag{2.48}$$

$$\Delta S = 0 \tag{2.49}$$

$$\Delta \Sigma = 0 \tag{2.50}$$

$$(+) \leftrightarrow (+), (-) \leftrightarrow (-) \quad \text{total parity is conserved} \tag{2.51}$$

$$\Delta F = 0, \pm 1, \pm 2 \quad F' + F'' \geq 2. \tag{2.52}$$

The labeling of the MDA and EQA transitions in OH or NO follows Equations 2.37 and 2.38, respectively. To distinguish EDA, MDA and EQA transitions from each other one prime for MDA transitions and two primes for EQA transitions are added to the label. For example in OH a $P_1''(1)$ transition is an EQA transition which involves $\Delta N = 1$, coupling the F_1 ρ-doublet in the excited $A\,^2\Sigma^+$ state to the F_1 spin-orbit manifold in the $X\,^2\Pi$ ground state and starting in absorption from, and ending in emission, in the level with $N = 1$.

	OH		NO	
ground state	$^2\Pi_{3/2}, J = 3/2$		$^2\Pi_{1/2}, J = 1/2$	
total mass (u)	17		30	
dipole moment (Debye)	1.67	[116]	0.159	[117]
rotational constant B_0 for $^2\Pi$ (cm^{-1})	18.515	[102]	1.67195	[117]
spin-orbit coupling constant A_0 for $^2\Pi$ (cm^{-1})	-139.73	[102]	123.8949	[118]
rotational constant B_0 for $^2\Sigma^+$ (cm^{-1})	16.961	[102]	1.986289	[105]
spin rotation coupling constant γ_0 for $^2\Sigma^+$ (cm^{-1})	0.226	[103]	-0.00237	[105]
ground state Λ-doublet splitting (cm^{-1})	0.055	[99]	0.0118	[100]
C_1(ground state)	0.17		1	
C_2(ground state)	0.98		0	
Ω_{eff} (ground state)	1.46		0.5	
nuclear spin I	0.5		1	

Table 2.1: Molecular parameters of OH and NO for their most abundant isotopomers, ^{16}OH and ^{14}N^{16}O.

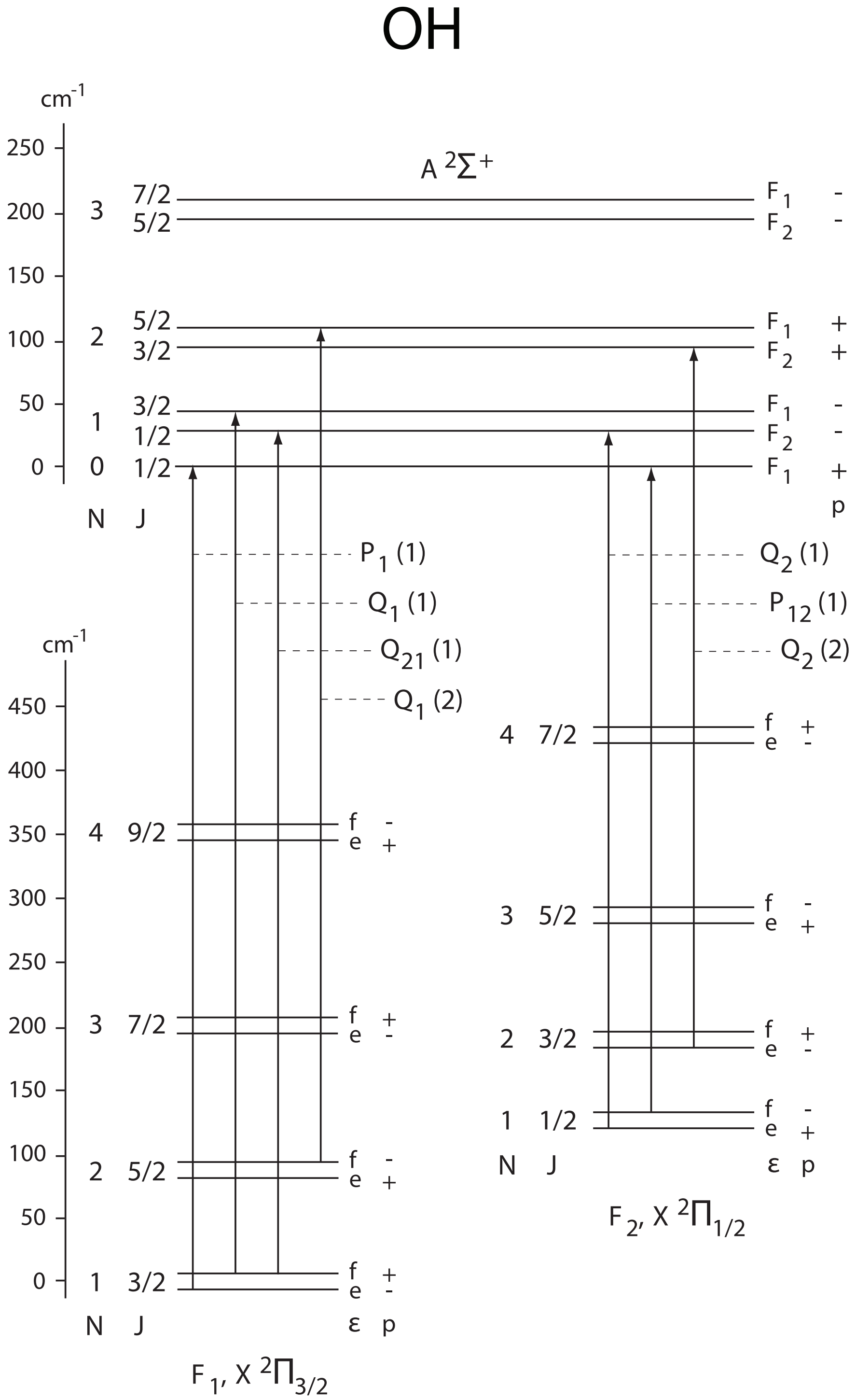

Figure 2.2: Energy level diagram of the electronic ground state $X\,^2\Pi$ and the first excited state $A\,^2\Sigma^+$ of OH. Both electronic states are in the vibrational ground state. The Λ-doublet and the ρ-doublet splitting are exaggerated for reasons of clarity. Some electric dipole allowed transitions for the detection of OH are indicated.

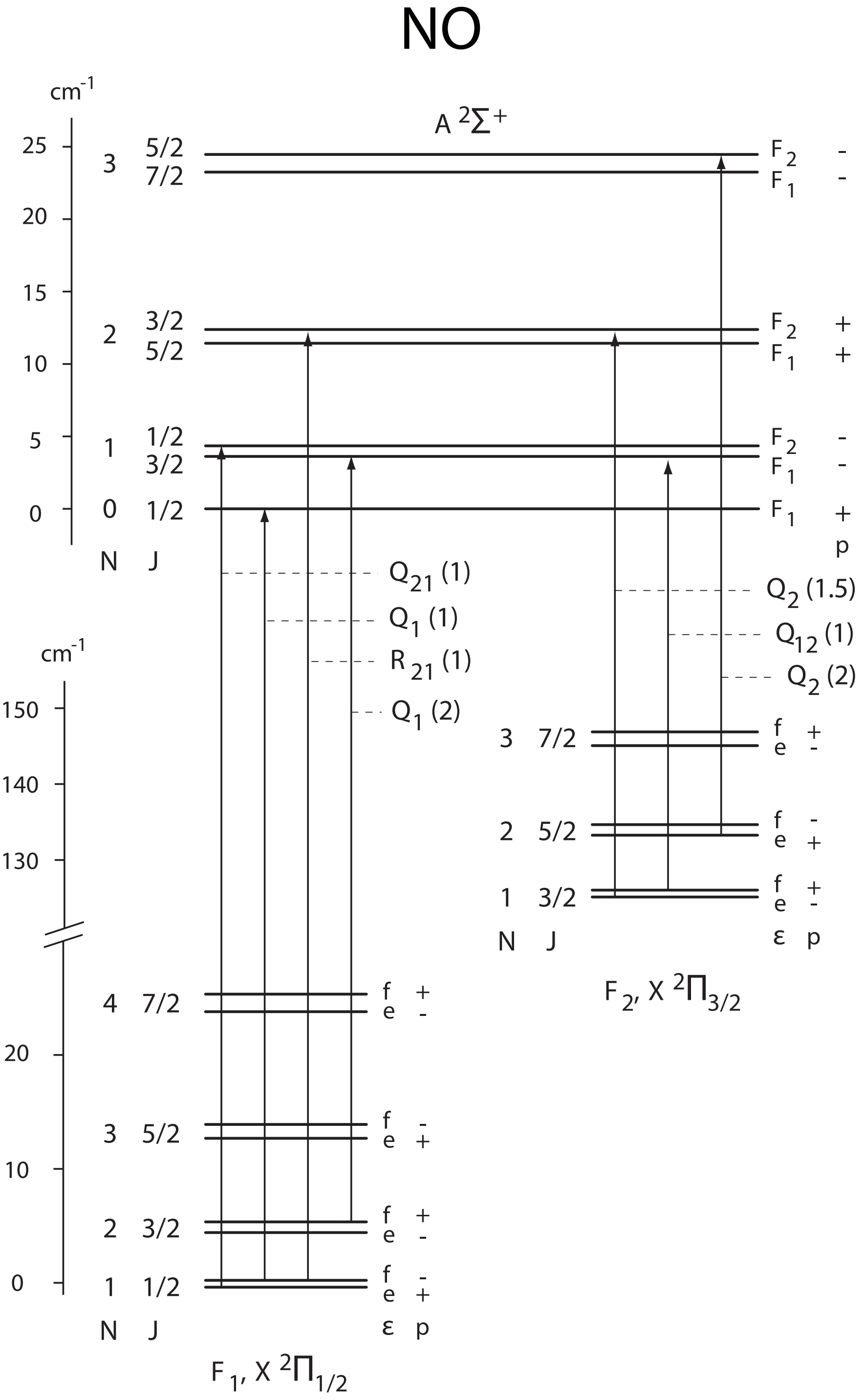

Figure 2.3: Energy level diagram of the electronic ground state $X\,^2\Pi$ and the first excited state $A\,^2\Sigma^+$ of NO. Both electronic states are in the vibrational ground state. The Λ-doublet and the ρ-doublet splitting are exaggerated for reasons of clarity. Some electric dipole allowed transitions for the detection of NO are indicated.

2.3 The molecular Stark effect

2.3.1 General formalism

The interaction of a polar molecule with an external electric field is called the Stark interaction. This interaction adds a Stark term $\boldsymbol{H}_{Stark} = -\boldsymbol{\mu} \cdot \boldsymbol{E}$ to the Hamiltonian, where $\boldsymbol{\mu}$ is the body-fixed electric dipole moment of the molecule and $\boldsymbol{E}$ is the space fixed electric field. For the following analysis it is convenient to define spherical irreducible tensor operators $T(k,p)$ of rank k with components $q = -k, -k+1, ...k$ [95]. The dipole moment and the electric field vectors are described in the space fixed frame by such spherical tensor operators $T(1,p)$ of rank 1 [76]. The Stark term in the Hamiltonian takes the form:

$$\boldsymbol{H}_{Stark} = -\boldsymbol{\mu} \cdot \boldsymbol{E} = -\sum_{p=-1}^{1} (-1)^p \, T_\mu(1,-p) \, T_E(1,p) \tag{2.53}$$

If the electric field is chosen such that its vector is parallel along the space fixed z-axis, i.e. $p = 0$ and $T_E(1,0) = E$, then the Stark term reduces to:

$$\boldsymbol{H}_{\text{Stark}} = -T_\mu(1,0) \, E. \tag{2.54}$$

Equation 2.54 describes the Stark effect in the space fixed frame, but the electric dipole moment $\boldsymbol{\mu}$ is defined in the body-fixed frame and therefore rotates with the molecule. To transform from space fixed to body fixed frame the Wigner rotation matrices are used [95]:

$$T_\mu(1,0) = \sum_{q=-1}^{1} D^{1*}_{0,q}(\phi,\theta,\chi) \, \widetilde{T}_\mu(1,q). \tag{2.55}$$

ϕ, θ, and χ are the Euler angles and $\widetilde{T}_\mu(1,q)$ are the components of $\boldsymbol{\mu}$ in the body-fixed frame. For a diatomic molecule there is an important simplification for Equation 2.55. Since Ω is defined along the internuclear axis only $q = 0$ needs to be considered. Now the Stark effect is calculated in the basis set of the symmetrized Hund's case(a) wavefunctions, Equation 2.14. From Equation 2.2 and 2.14 it is obvious, that this will result in matrix elements of the type:

$$\langle J\,\Omega\,M | \, \boldsymbol{H}_{Stark} \, | J'\,\Omega'\,M' \rangle \,. \tag{2.56}$$

Note that $\boldsymbol{H}_{Stark}$ only affects the rotational part of the wavefunction. The $|J'\,\Omega'\,M'\rangle$ are the rigid body rotational basis wavefunctions, Equation 2.4. Following the analysis in [76] the Stark matrix elements are evaluated:

$$\begin{aligned}\langle J\,\Omega\,M | \, \boldsymbol{H}_{Stark} \, | J'\,\Omega'\,M' \rangle = &-\delta(M,M')\mu E\sqrt{(2J+1)(2J'+1)}(-1)^{M-K} \\ &\times \begin{pmatrix} J & 1 & J' \\ M & 0 & -M \end{pmatrix} \begin{pmatrix} J & 1 & J' \\ \Omega & 0 & -\Omega' \end{pmatrix}\end{aligned} \tag{2.57}$$

The Wigner 3-J symbols give rise to the following selection rules:

$$J = J', \quad J = J' \pm 1, \quad M = M', \quad \Omega = \Omega' \tag{2.58}$$

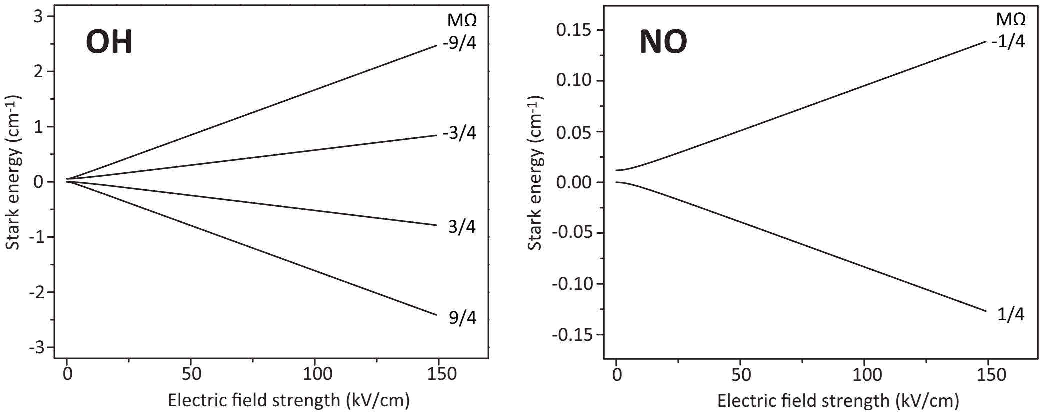

Figure 2.4: Left panel: Stark shift of the OH ground state $^2\Pi_{\frac{3}{2}}, J = 3/2$ as a function of the electric field strength. Right panel: Stark shift of the NO ground state $^2\Pi_{\frac{1}{2}}, J = 1/2$ as a function of the electric field strength. Note the different scales on the y-axes.

2.3.2 Stark effect of OH and NO

For both radicals, OH and NO, the rotational spacing is relatively large compared to the Stark energy, and therefore the coupling between states with $J = J' + 1$ is relatively weak. At small electric field strengths, like the ones typically used in this thesis, the mixing between different rotational states is therefore neglected. It is now time to set up the Stark matrix in the basis set of the OH and NO eigenfunctions $|^2\Pi; F_{1,2}, J, M; \pm\rangle$ of $\boldsymbol{H}_{\nu}^{rot}$ given in Equation 2.18. The Stark effect mixes levels with different parity [95]. Thus the Stark effect matrix contains non-zero off-diagonal elements:

$$\begin{pmatrix} E_\Lambda & Q \\ Q & 0 \end{pmatrix}. \tag{2.59}$$

E_Λ is the zero-field Λ-doublet splitting and Q is calculated with the help of Equation 2.57:

$$Q = \langle ^2\Pi; F_{1,2}, J, M; \pm | \, \boldsymbol{H}_{Stark} \, |^2\Pi; F_{1,2}, J, M; \mp\rangle = -\mu E \frac{M_J \Omega_{\text{eff}}}{J(J+1)}, \tag{2.60}$$

where Ω_{eff} is the effective value of Ω:

$$\Omega_{\text{eff}} = \left(\frac{1}{2} C_1(J)^2 + \frac{3}{2} C_2(J)^2 \right) \tag{2.61}$$

For the Stark shift of the energy levels the eigenvalues of the Stark matrix have to be calculated:

$$E_{\text{Stark}} = \frac{E_\Lambda}{2} \pm \sqrt{\left(\frac{E_\Lambda}{2} \right)^2 + Q^2}. \tag{2.62}$$

The plus and minus sign is for the upper and lower Λ-doublet respectively. Figure 2.4 shows the Stark shifts of the OH ground state $^2\Pi_{\frac{3}{2}}, J = 3/2$ and of the NO ground state $^2\Pi_{\frac{1}{2}}, J = 1/2$. For low electric fields the Stark shift is quadratic and for high electric fields it becomes linear. Levels with positive Stark shift are called low-field-seeking and levels with negative-stark-shift are called high-field-seeking. The low-field-seeking molecules are suited for the confinement with electric fields, for instance in a hexapole or Stark decelerator.

2.3.3 Hyperfine Stark effect

With the help of the new eigenfunctions, that are expanded by the hyperfine part, the hyperfine Stark energy is calculated. Analogous to the description in Section 2.3 the matrix elements of $\boldsymbol{H}_{Stark}$ are calculated in the new basis set of the hyperfine structure. The full analysis is found in [101], here only the result from [116] is given:

$$\begin{aligned}
&\langle {}^2\Pi; F_{1,2}, J, M, I, F, M_F; \pm |\, \boldsymbol{H}_{Stark}\, |{}^2\Pi; F_{1,2}, J, M, I, F, M_F; \pm \rangle \\
&= f\delta(\Omega, \Omega')\delta(M_F, M_F')\mu E(-1)^{2J+I+F+F'-M_F-\Omega} \\
&\times \sqrt{(2J+1)(2J'+1)(2F+1)(2F'+1)} \\
&\times \begin{Bmatrix} J & F & I \\ F' & J' & 1 \end{Bmatrix} \begin{pmatrix} F & 1 & F' \\ -M_F & 0 & M_F' \end{pmatrix} \begin{pmatrix} J & 1 & J' \\ \Omega & 0 & -\Omega' \end{pmatrix},
\end{aligned} \tag{2.63}$$

where the factor f is zero if $|J - J'| = 0$ and equal parity or if $|J - J'| = 1$ and unequal parity.

2.4 Production of molecular beams

In a molecular beam the thermal energy of the molecules in the beam source is converted into kinetic energy of the molecules along the beam direction. This is done either in continuous or pulsed sources, called the nozzle [119]. This analysis is restricted to pulsed sources as they are used in Stark-decelerators and all experiments described in this thesis. After the supersonic expansion from the nozzle the final velocity v_0 of the molecular beams follows the equation [119]:

$$v_0 = \sqrt{\frac{2k_B T_0}{m}\frac{\gamma}{\gamma - 1}}, \tag{2.64}$$

where k_B is the Boltzmann constant, T_0 the temperature in the source, m the mass of the molecule, and

$$\gamma = \frac{C_p}{C_V} = \frac{f+2}{f}, \tag{2.65}$$

is the ratio of the heat capacity and volume at constant pressure of that molecule. f is the degree of freedom of the particle. For a rare gas atom $\gamma = 5/3$, with

$f = 3$. The final velocity v_0 is the mean velocity of the Gaussian distribution of velocities of the molecular packet.

The formation of clusters limits the minimal temperature, that can be reached in pure molecular beams. This can be circumvented by seeding the molecular species in an inert carrier gas, e.g. He, H_2, N_2, Ne, Ar, Kr, or Xe. The final velocity is then defined by an average value for m and γ, depending on the seed concentration. Light carrier gases produce higher velocities (He ≈1800 m/s) and heavy carrier gases produce lower velocities (Xe ≈350 m/s). With a sophisticated mix of these carrier gases a wide range of collision energies is covered. In a supersonic expansion, due to inelastic collisions the vibrational and rotational populations are shifted to lower quantum levels. Temperatures in the mK regime are reached. The mass of the carrier gas and the interaction potential of the carrier gas and molecule also defines the state purity of the molecular beam [39, 119].

2.5 Manipulation of polar molecules using the Stark effect

After the introduction of the energy structure of the OH and the NO radicals and their Stark effect, it is explained in this section how the Stark effect is exploited to manipulate the motion and the quantum states of these two polar molecules.

The general idea is, that in an inhomogeneous electric field polar molecules experience, depending on their quantum state, a force which drives them to a field minimum or maximum. Therefore, these molecules are called low-field seeking or high-field seeking. In the 1950s Gordon, Zeiger, and Townes [11, 12] and independently Bennewitz, Paul and Schlier [13] demonstrated that an electric quadrupole field can be used to focus a molecular beam. They designed a so-called quadrupole guide or quadrupole selector. A quadrupole selector creates a local field minimum and molecules in low-field seeking quantum states are driven towards this minimum (focused), while high-field seeking quantum states are driven away (defocused). For OH such selectors have been used for instance for the measurement of the population inversion of the two Λ-doublet states [15], but the maybe most famous example of a quadrupole guide remains its first application which led to the invention of the maser [11, 12].

Bennewitz et al. already suggested the use of a hexapole field, but the first experimental realization was not until 1965 by Kramer and Bernstein [14]. The main difference between a hexapole field and a quadrupole field is the dependence of the electric field strength E on the distance r from the center, i.e. the molecular beam axis. For a quadrupole field E depends linearly on r and for a hexaopole field E depends quadratically on r. The focusing force for polar molecules in the electric field is the negative gradient of the Stark energy. If the guide or selector is used as a focusing device or lens the focusing force has to be harmonic. Thus in case of a quadratic Stark effect a linear dependence on r, and in case of a linear Stark effect a quadratic dependence on r is required. Quadrupole selectors are

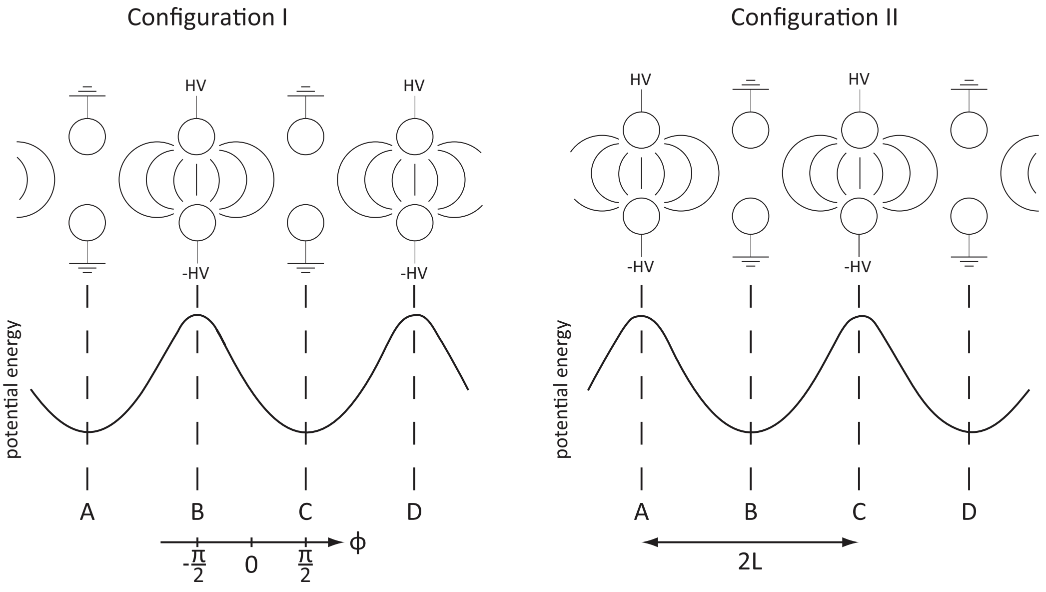

Figure 2.5: Operating principle of a Stark decelerator

best suited for molecules with a quadratic Stark effect and hexapole devices are best suited for molecules with a linear Stark effect.

Since the work by Kramer and Bernstein, there have been many applications using hexapole fields. In Chapter 4 of this thesis, a detailed overview of the applications and an analysis of the physics and designs of hexapole devices will be given.

In both approaches to state-select molecules, either the quadrupole or the hexapole device acts as a spatial filter or as a lens for particles, influencing only the transversal velocity of the molecular beam. It was not until 1999, that it was experimentally demonstrated that also the longitudinal velocity of a molecular beam can be influenced by electric fields, using a so-called Stark decelerator [72].

2.5.1 Stark deceleration

Here a short overview of Stark deceleration is given. Full length articles and reviews are found in [72, 73, 74, 75, 76, 77].

A Stark decelerator consists of an array of high voltage electrode pairs. A pulsed molecular beam passes between these electrode pairs and a computer controlled switching sequence switches the high voltages to obtain a certain desired velocity for the molecules. Figure 2.5 sketches the electrode array and the potential energy of the low field seeking molecules in the two configurations. The potential energy, i.e. the Stark energy, depends on the electric field strength. Low-field-seeking molecules exhibit a minimum in potential energy at each electrode pair on ground and a field maximum at each electrode pair on high voltage. If a molecule is traveling from position A to B in field configuration I (Figure 2.5) it feels a force in opposite direction and is therefore slowed down, i.e. looses kinetic energy.

Without switching it continues to position C and regains all its kinetic energy. Instead, before reaching the top of the potential, the Stark decelerator is switched to configuration II. Now the molecule has lost its energy and continues to position C where the whole procedure is repeated. The amount of energy that is removed per stage is small, e.g. for OH around 1% of the initial kinetic energy. Therefore the decelerator consist of many stages, in order to be able to slow down molecules to a standstill.

Phase angle and the synchronous molecule

For the description of the longitudinal motion in a Stark decelerator the concept of the phase angle ϕ and the synchronous molecule have proven to be very useful. The distance between two electrode pairs is defined as L. The minima and maxima of the potential energy have a periodicity of $2L$. The phase angle ϕ is the reduced position $\frac{2\pi}{L}$ of the molecule with $\phi = 0$ being the position between two adjacent electrode pairs and $\phi = \pi/2$ the position at the electrode pair switched to ground (Figure 2.5). The synchronous molecule is the molecule whose phase angle ϕ_0 remains constant at each time the fields are switched, i.e. whose relative position in the potential remains constant. In each switching cycle a constant amount of kinetic energy is removed from the synchronous molecule and due to the reduced velocity the time between switching becomes longer in order to keep ϕ_0 constant. In most Stark deceleration applications the velocity v_0 of the synchronous molecule is the very same as the mean velocity of the molecular beam passing through the decelerator. $\phi_0 = 0$, in general called "guiding", does not change the velocity of the synchronous molecule, while positive phase angles decelerate the molecules until the maximal deceleration of $\phi_0 = 90°$. The whole concept works equivalent for the acceleration of molecules with negative phase angles.

Non-synchronous molecules have a slightly different position or velocity from the synchronous molecule and thus feel a stronger (weaker) force if they are in front (behind) the synchronous molecule. They are driven towards the synchronous molecule and start to oscillate around the synchronous molecule in space and velocity. Thus the decelerator keeps the molecular packet longitudinally together. The molecular trajectories are best understood looking at the 2D longitudinal phase space. The separatrix, that is the region in phase space where molecules are phase stable, gives the longitudinal acceptance of the decelerator. Figure 2.6 shows different regions of stability for different values of the phase angle ϕ_0 , i.e for different amounts of deceleration. Larger phase angles lead to a smaller separatrix and simultaneously fewer molecules.

Transverse stability in a decelerator

In the transverse direction the molecules also exhibit a force which keeps the molecular packet together. The transverse potential energy is always minimal at the central axis of the decelerator, independent of the switching cycle. Therefore,

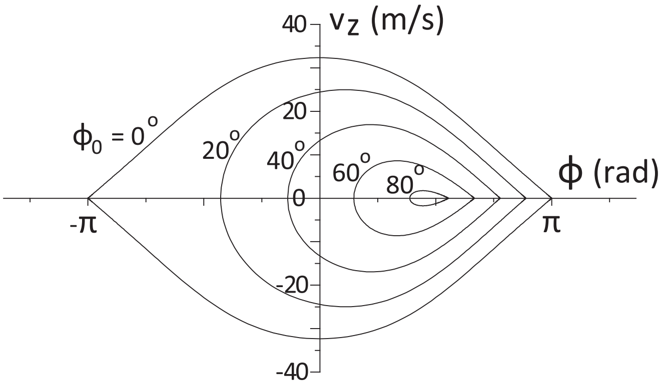

Figure 2.6: Longitudinal acceptance of the decelerator for different values of the phase angle ϕ_0, calculated for OH ($^2\Pi_{3/2}, J = 3/2, M_J = 3/2$).

in principle, the molecules are always transversally focused. However, depending on the longitudinal position these focusing forces can be very small or in the worst case the longitudinal and transverse motion are coupled such that the transverse motion is increased in each switching cycle, leading to unstable trajectories. This parametric amplification can be circumvented when, instead of switching the decelerator in every stage, the decelerator is switched after the molecules passed a number of s stages [76, 83, 120]. In $s = 3$, for instance, the molecules travel a distance of three stages before the decelerator is switched from one configuration to the other. The amount of removed energy per switching cycle is the same for $s = 3$ and $s = 1$, but with the difference that $s = 3$ uses one additional pair of electrodes only for transverse focusing. Hence, a decelerator using $s = 3$ has to be three times longer to reach the same final velocity. Scharfenberg et al. [83] demonstrated that in $s = 3$ mode the acceptance of the decelerator approaches the optimum value. Below 50 m/s for $s = 1$ and below 150 m/s for $s = 3$ mode, significant losses are expected due to transverse over focusing. These effects have been observed experimentally [83,121], and new schemes to attenuate these losses have been proposed and implemented [121, 122, 123].

The Stark decelerator used in this thesis it the longest built to date. It is 2.6 m long and consist of 316 deceleration stages. It was exclusively designed for use in the $s = 3$ mode in order to increase the number density of particles. The same apparatus was used by Scharfenberg et al. for the detailed study of a Stark decelerator operating with optimum acceptance [83].

2.5.2 Stark deceleration of OH molecules

From the Stark shift in Figure 2.4, it can be seen that the OH radical is decelerated in the upper Λ-doublet of its $^2\Pi_{3/2}, J = 3/2$ ground state. Both M_J components are decelerated, but with different efficiency depending on the phase angle [76]. Before the decelerator the two Λ-doublet components of the $^2\Pi_{3/2}, J = 3/2$ rotational ground state are equally populated. After the decelerator ≥99.999% of

OH radicals in the $^2\Pi_{3/2}, J = 3/2$ rotational ground state reside in the upper Λ-doublet component of f parity; the lower Λ-doublet component of e parity is effectively depopulated in the Stark-deceleration process. Depending on the carrier gas used in the production of the molecular beam, higher rotational and vibrational states are still present in the beam after the deceleration process. In all experiments in this thesis the OH radicals are produced by photolysis of nitric acid (HNO_3) at 193 nm. The nitric acid is seeded in an inert carrier gas. Jacobs et al. showed that OH radicals produced from photolysis of nitric acid at 193 nm exhibit very little vibrational excitation [124]. Scharfenberg et al. measured background populations of OH produced from nitric acid and estimated, that for the carrier gases Xe and Ar the quantum state purity of the OH radicals approaches 100% [125]. Only for the carrier gases He and Ne it drops below 99% but never below 97%. The populations of low-field-seeking states of e parity are always negligible.

2.5.3 Stark deceleration of NO molecules

Due to the small NO dipole moment of only 0.159 Debye, Stark deceleration of the NO ground state $^2\Pi_{1/2}, J = 1/2$ has not been accomplished to date. The force on the molecules per stage is too weak to efficiently decelerate NO. A different approach is to pump molecules to the lowest rotational state of the other spin-orbit manifold $^2\Pi_{3/2}, J = 3/2$, and to use the factor 1.8 larger Stark shift. With the increased force it is possible to also decelerate the important NO radical. This approach will be discussed in detail in Chapter 7 of this thesis.

2.6 Crossed beam scattering

The principle of crossed beam scattering is very simple: Two reagent beams are crossed under a certain angle and the scattering occurs at the point of intersection [39, 119, 126]. The collision products are scattered at an angle and are detected by a detector. If the detector is sensitive to this scattering angle it probes the differential cross section (DCS). If the detector covers all scattering angels at once it probes the integral cross section (ICS). The collision energy is defined by the velocity of the two collision partners, their masses, and by their angle of incidence α. In a collision experiment the velocity [82] or the angle of incidence α [31, 32] can be varied to change the collision energy.

2.6.1 Kinematics

The kinematics of two colliding particles can be fully understood using classical mechanics. It is convenient to transform the coordinate system from the lab frame to the center-of-mass (CM) system. Figure 2.7 shows the transformation to the CM system and the parameters of the transformation. The relative distance $\boldsymbol{r}$,

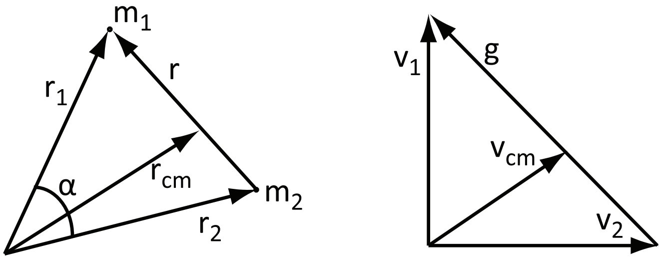

Figure 2.7: Definition of coordinates and velocities in the lab frame and the center-of-mass system.

the relative velocity $\boldsymbol{g}$, the total mass M, and the reduced mass μ are defined by:

$$\boldsymbol{r} = \boldsymbol{r}_1 - \boldsymbol{r}_2 \tag{2.66}$$

$$\boldsymbol{g} = \boldsymbol{v}_1 - \boldsymbol{v}_2 \tag{2.67}$$

$$M = m_1 + m_2 \tag{2.68}$$

$$\mu = \tfrac{m_1 m_2}{M}. \tag{2.69}$$

The center-of-mass is defined as:

$$M\boldsymbol{r}_{cm} = m_1\mathbf{r}_1 + m_2\mathbf{r}_2, \tag{2.70}$$

and therefore the position $\boldsymbol{r}_{cm}$ of the center of mass is:

$$\boldsymbol{r}_{cm} = \tfrac{m_1\mathbf{r}_1 + m_2\mathbf{r}_2}{M}. \tag{2.71}$$

The combination of equation 2.66, 2.69, and 2.71 and their derivatives result in four equations, relating the positions and velocities of both particles in both systems:

$$\boldsymbol{r}_1 = \boldsymbol{r}_{cm} + \tfrac{\mu}{m_1}\boldsymbol{r} \tag{2.72}$$

$$\boldsymbol{r}_2 = \boldsymbol{r}_{cm} - \tfrac{\mu}{m_2}\boldsymbol{r} \tag{2.73}$$

$$\boldsymbol{v}_1 = \boldsymbol{v}_{cm} + \tfrac{\mu}{m_1}\boldsymbol{v} \tag{2.74}$$

$$\boldsymbol{v}_2 = \boldsymbol{v}_{cm} - \tfrac{\mu}{m_2}\boldsymbol{v}. \tag{2.75}$$

The kinetic energy in the lab frame is: $T = \frac{1}{2}m_1\boldsymbol{v}_1^2 + \frac{1}{2}m_2\boldsymbol{v}_2^2$. Inserting equation 2.74 and 2.75 into this expression leads to a expression for the kinetic energy:

$$T = \frac{m_1 + m_2}{2}\mathbf{v}_{cm}^2 + \frac{\mu}{2}\mathbf{g}^2. \tag{2.76}$$

The first part of this expression is the total kinetic energy in the CM system, which is always constant. The second part is the relative kinetic energy which is also called the collision energy.

$$T_{rel} = E_c = \frac{\mu}{2}\mathbf{g}^2 = \frac{\mu}{2}(v_1^2 + v_2^2 - v_1 v_2 \cos\alpha). \tag{2.77}$$

For 90° angle between the two collision partners 2.77 simplifies to:

$$E_c = \frac{\mu}{2}(v_1^2 + v_2^2). \tag{2.78}$$

For an elastic collision the relative velocity g and the relative kinetic energy remain constant, for an inelastic collision the relative kinetic energy changes by ΔE_{int}. This change of energy is either positive or negative depending on the change of internal energies of both collision partners, i.e. in a molecule the change of the quantum state. Because of the conservation of energy $\frac{\mu}{2}g'^2 = \frac{\mu}{2}g^2 + \Delta E_{int}$ the relative velocity g' after the collision is expressed by:

$$g' = g\sqrt{\frac{T_{rel} + \Delta E_{int}}{T_{rel}}} \tag{2.79}$$

The magnitude of the relative velocity g' after the collision is fixed, but the orientation in respect to the orientation of g before the collision, is defined by the initial conditions and the intermolecular potential, i.e. the potential energy surface (PES), of the scattering system. Thus by measuring the orientation of g' for instance with a velocity-map-ion-imaging detector [47, 53] much is learned about the PES. In an elastic collision the magnitude of g and g' is equal. In an inelastic collision g' is smaller or larger than g depending on the energy difference between the initial state and the final state after the collision. How strong each final state is populated after the collision is also described by the PES. Hence, measuring the state population before and after the collision is another possibility to learn about the PES. This approach of measuring inelastic collisions is followed in this work, reported in Chapter 3 on the collision of OH-He and OH-D_2 and in Chapter 5 on the collision of OH-NO.

2.7 Detection methods

2.7.1 Laser Induced Fluorescence

The most convenient detection method for OH and NO radicals is Laser Induced Fluorescence (LIF) on the $A\,^2\Sigma^+ \leftarrow X\,^2\Pi$ transition. The applications for LIF in modern science are countless, making an overall overview an almost impossible endeavor. Also in the field of molecular collisions, which is closely related to this work, LIF [56] had a great impact on the investigation of chemical reactions [127], molecular beam diagnostics [128] and (non)-reactive scattering.

Let the quantum numbers α, ν and J denote the electronic, vibrational and rotational state, respectively. In general there will be three states involved in a LIF process: An initial state $|i\rangle = |\alpha''\nu''J''\rangle$, an excited state $|e\rangle = |\alpha'\nu'J'\rangle$, and a final state $|f\rangle = |\alpha\nu J\rangle$ (Figure 2.8). A LIF experiment consist of two steps: First the excitation $|\alpha'\nu'J'\rangle \leftarrow |\alpha''\nu''J''\rangle$ of the molecule from its probed initial state to a higher electronic state and second the detection of the fluorescence $|\alpha'\nu'J'\rangle \rightarrow |\alpha\nu J\rangle$ to one or a number of final states. The initial state is in most cases the

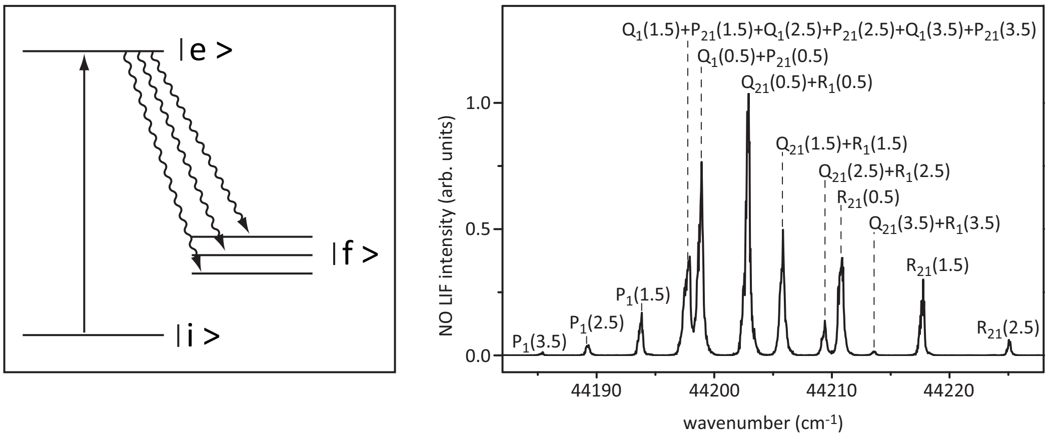

Figure 2.8: Left panel: Principle of LIF, showing the three involved states and the two LIF steps. Right panel: Unsaturated LIF spectra of NO of the $A\,^2\Sigma^+ \leftarrow X\,^2\Pi$ transition. Different rotational transitions are assigned. The experiment is performed in a supersonic jet. The NO is cooled, due to the supersonic expansion, Chapter 2.6.

ground state. For many LIF processes the final state or one of the final states is the same as the initial state, i.e. $|\alpha''\nu''J''\rangle = |\alpha\nu J\rangle$. Excitation is done with a short laser pulse and fluorescence is measured with a photo multiplyer tube (PMT). In an ideal LIF experiment the laser pulse is much shorter than the lifetime τ of the excited state, the excited state is unpopulated prior to the excitation and other decay mechanisms like predissociation, collisional quenching, or ionization can be neglected. Following these assumptions the total rate $R(p_a, p_f)$, at which a molecule absorbs laser light with the polarization p_a and emits fluorescence of polarization p_f can be expressed by a molecular Breit formula [129, 130]: Let m'' be the magnetic sublevels of the initial state $|i\rangle$. Let both M and M' be magnetic sublevels of the excited state $|e\rangle$ and m those of the final state $|f\rangle$:

$$R(p_a, p_f) = \sum_{\alpha}\sum_{\nu}\sum_{J}\sum_{M}\sum_{M'} \frac{A_{MM'}F_{MM'}}{\frac{1}{\tau} - i(E_{\nu'J'M'} - E_{\nu'J'M})/h} \tag{2.80}$$

$$A_{MM'} = \sum_{m''} \langle \nu'J'M \,|\mu \cdot \epsilon_{p_a}|\, \nu''J''m''\rangle \langle \nu''J''m'' \,|\mu \cdot \epsilon_{p_a}|\, \nu'J'M'\rangle \tag{2.81}$$

$$F_{M'M} = \sum_{m} \left\langle \nu'J'M' \,\middle|\mu \cdot \epsilon_{p_f}\middle|\, \nu J m\right\rangle \left\langle \nu J m \,\middle|\mu \cdot \epsilon_{p_f}\middle|\, \nu'J'M\right\rangle . \tag{2.82}$$

$$\tag{2.83}$$

$E_{\nu'J'M'} - E_{\nu'J'M}$ is the energy gap between the magnetic sublevels of the excited state and $A_{MM'}$ and $F_{MM'}$ are the absorption and fluorescence matrices, respectively. Equation 2.80 is in all its detail quite complicated. It is used, for instance to determine product population and alignment using LIF [131]. Fortunately in most experiments it can be significantly simplified.

Unsaturated LIF

A much simpler equation for the line intensity within a LIF-spectrum, is achieved under two assumptions. First: Polarization effects of the excitation laser and the fluorescence do not play a role. Let the laser light and the fluorescence light be unpolarized and let the fluorescence be emitted homogeneously, i.e. the orientation of the PMT and the laser beam path do not need to be considered. Second: The laser power is small enough to neglect saturation. This situation is called the unsaturated LIF condition. The absorption and fluorescence matrices are simplified to Einstein coefficients and the total fluorescence line intensity I in (W m^{-3}) is expressed by [56, 96, 132]:

$$I(e,i,t) = k\Big\{N_i\, \rho(\lambda_i^e)\, B_i^e\Big\} \sum_{\alpha}\sum_{\nu}\sum_{J} A_f^e\, P(\lambda_f^e)\, h\, \nu_f^e\, \tau(1-e^{-\frac{t}{\tau}}) \tag{2.84}$$

$$B_i^e = \frac{2\pi^2}{3h^2\epsilon_0 c}\,\frac{S_i^e}{2J''+1} \tag{2.85}$$

$$A_f^e = \frac{16\pi^3}{3h\epsilon_0}\,\frac{S_f^e}{2J'+1}(\nu_f^e)^3. \tag{2.86}$$

The term in brackets represents the absorption, the term after the sums the emission, and k is a dimensionless proportionality constant which includes the geometric factors of the PMT setup. N_i is the population of the probed initial state in cm^{-3}, $\rho(\lambda_i^e)$ is the radiation field energy density, i.e. the laser, at the wavelength λ_i^e of the $|e\rangle \leftarrow |i\rangle$ excitation transition in energy per unit volume per unit wavenumber, $P(\lambda_f^e)$ is the dimensionless sensitivity of the PMT at the wavelength λ_f^e of the $|e\rangle \rightarrow |f\rangle$ transition, h is the Planck constant, ν_f^e the frequency of the $|e\rangle \rightarrow |f\rangle$ fluorescence transition, τ is the lifetime of the excited state in seconds and t is the time at which the fluorescence is detected. B is the absorption coefficient in (s^{-1}) [133] and A the emission coefficient in (m^2 J^{-1} s^{-1}) [133]

Both Einstein coefficients take the degeneracy of the rotational states $(2J+1)$ into account. For most diatomic molecules the spin multiplicity does not need to be considered, because of the selection rule $\Delta S = 0$ (Equation 2.33). But $\Delta S = 0$ is not a rigorous selection rule and is violated for example when spin-orbit interaction is not negligible. In that case an additional factor $(2S+1)$ needs to be considered, with S being the total spin. The factor $S_{i,f}^e$ is the line strength which is approximately factored into a vibrational, electronic and rotational part:

$$S_i^e = R_e(\alpha'',\alpha')^2\, q(\nu'',\nu')\, S_{J''}^{\Delta J}, \tag{2.87}$$

where $R_e(\alpha'',\alpha')$ is the electronic transition moment, $q(\nu'',\nu')$ the Franck-Condon factor, and $S_{J''}^{\Delta J}$ the Hönl-London factor. Note that S_f^e is defined analogously.

In most LIF experiments the sensitivity of the PMT detector is constant within the detection range and therefore all the fluorescence is detected independent of the final states. Hence the line intensity will only depend on the absorption process and the lifetime of the excited state. For most applications it is reasonable to detect from $t = 0$ until $t \gg \tau$ and to use excited states which all have approximately the same lifetime τ. Furthermore the laser power should be kept constant. Equation 2.84 is then simplified to:

$$I(e,i) \propto N_i \, B_i^e. \tag{2.88}$$

With the help of Equation 2.88 the initial populations of different molecular states are measured. The absorption coefficients of selected diatomic molecules are well known and to be found, for instance, in the database of the LIFBASE program [134]. Figure 2.8 shows an example of an unsaturated LIF spectrum of NO. In this experiment different rotational levels of the NO ground state $X\,^2\Pi_{1/2}$ are populated. After the assignment of all rotational transitions, the populations N_i of the initial rotational levels are directly derived from the line intensities with the help of Equation 2.88. Another application for unsaturated LIF is the evaluation of the intensity of different transitions, i.e. the line strength, for example used in Chapter 6.

Saturated LIF

In some experiments it might be desirable to increase the laser power for instance to increase the detection signal. Above the saturation limit the signal does not increase, but power broadening occurs [135]. Equation 2.84 is then no longer correct. Under such conditions, absorption and stimulated emission distribute the population equally over the initial state and the excited state. For a two-level system the amount of molecules after the laser pulse in the initial state N_i' and the excited state N_e is distributed according to: $N_i' = N_e = \frac{1}{2}N_i$. N_i is the original number of molecules in the initial state before the laser pulse. This two level picture is too simplified. Instead the states consist of $(2J+1)$ degenerate M_J components. In saturation the signal intensity $I(i,e)$ is no longer proportional to the laser power and the absorbtion coefficients, but proportional to the amount of molecules in the initial state before the laser pulse and the so-called excitation factor ϵ, that includes the degeneracy g_e of the excited state and g_i of the initial state, i.e. the probed state [136, 137].

$$\begin{aligned} I(e,i) &\propto \epsilon \cdot N_i && \qquad (2.89) \\ \epsilon &= \frac{g_e}{g_e + g_i} \\ &= \frac{(2J'+1)}{(2J'+1)+(2J''+1)} && \text{(for } J \text{ degeneracy)} \qquad (2.90) \end{aligned}$$

This expression is correct when the sensitivity of the PMT is constant over the whole detection range, when $t \gg \tau$, and when the excited states all have approximately the same lifetime τ. When measuring in saturated condition it is essential to keep the detection volume and the laser power constant and to make sure that for each probed molecular level the transition is saturated. Yet for each molecule a profound analysis needs to be done which excitation factor has to be incorporated in the data analysis. If this is done incorrectly, wrong determination of populations are inevitable [45].

2.7.2 Laser Induced Fluorescence in OH and NO

For both molecules OH and NO the best suited transition for LIF, the $A\,^2\Sigma^+ \leftarrow X\,^2\Pi$ transition, lies in the UV. Because a PMT is in general sensitive from the UV to the near-IR one major problem in a LIF experiment is the scattered light. Scattered light is caused by the excitation laser and residual light in the visible range. In some experimental setups the scattered light is much more intense than the fluorescence light, making resonant fluorescence detection experimentally challenging, if not impossible. This problem is solved by either a sophisticated LIF-zone design to minimize the stray light or by using off-resonant fluorescence detection, which uses different vibrational bands for excitation and detection. In this approach the scattered light and the residual light in the visible are blocked by an optical filter. The fluorescence light is still detected, as the filter keeps a transmission window open in the range of the fluorescence light.

OH has been detected with resonant fluorescence detection after excitation of the $\nu' = 0 \leftarrow \nu'' = 0$ band around 308 nm. But in all experiments on OH presented in this thesis off-resonant fluorescence detection of the $\nu' = 1 \rightarrow \nu = 1$ band around 313 nm after excitation of the $\nu' = 1 \leftarrow \nu'' = 0$ band around 282 nm was used. A sophisticated filter minimized the stray light [125]. The radiative lifetime of the excited $A\,^2\Sigma^+, \nu = 1$ state of the OH radical is 717 ns [138].

For NO the situation is different since the off-diagonal Franck-Condon factors are much larger. After excitation of the $\nu' = 0 \leftarrow \nu'' = 0$ band around 226 nm, the fluorescence $\nu' = 0 \rightarrow \nu = 0, 1, 2, ...$ up to $\nu = 9$ around 353 nm is easily detected. In all experiments on NO presented in this thesis the scattered light was reduced by a SCHOTT UG-5 filter. For a detailed analysis of the reduction of fluorescence light by the filter a convolution of the Franck-Condon-factors with the transmission curve of the filter has to be done.

2.7.3 Measuring the absolute number of molecules

So far the described methods for unsaturated and saturated LIF are only used to determine the relative population of different molecular states. In some experiments it might be desirable to evaluate the absolute number of molecules, for example to know the absolute density, Chapter 5. For such an experiment the number of fluorescence photons has to be counted. The number of molecules in the initial state N_i depends on the number of detected photons $N_{photons}$ via

$$N_i = \frac{N_{photons}}{\Omega\, T\, Q\, \epsilon}, \tag{2.91}$$

where Ω is the solid angle observed by the PMT and T is the transmission efficiency of the windows and filters in front of the PMT. Q is the quantum efficiency of the PMT, and ϵ represents the fraction of the molecules that contribute to the fluorescence signal upon laser excitation. Under saturated LIF conditions ϵ becomes the excitation factor. In Chapter 5 this relation will be used to measure the absolute density of Stark-decelerated OH radicals and hexapole-focused NO radicals.

2.7.4 Resonance Enhanced Multi-Photon Ionization

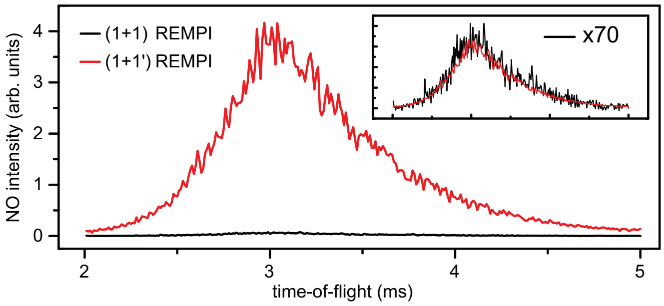

Figure 2.9: Comparison of (1+1) and (1+1') REMPI schemes in NO. The NO is excited from the ground state via the $A\,^2\Sigma^+ \leftarrow X\,^2\Pi$ transition and then ionized. The inset shows the same measurements where the (1+1) REMPI scheme is multiplied by a factor 70. The experiment is performed in a supersonic jet and the detection time is varied. The x-axis shows the detection time for the NO molecules and the y-axis the NO intensity in arbitrary units. The (1+1) REMPI scheme was performed with one focused pulsed dye laser (PDL) at 226 nm. The (1+1') REMPI scheme was performed with the same PDL but unfocused and a high power Nd:YAG laser at 266 nm.

An alternative to LIF is Resonance Enhanced Multi-Photon Ionization (REMPI). In many aspects REMPI is akin to LIF since it is also a two step process. In the first step the molecules are excited to an excited state and in the second step they are ionized into the continuum. In a time-of-flight mass spectrometer the ions are extracted and accelerated by ion optics, guided along a flight tube, and mapped onto microchannel plates (MCPs). The REMPI scheme is labeled by the number of photons required to reach the excited state and the number of photons required to ionize. Although the probability for multi photon excitation is small, (2+1) and even (3+1) REMPI schemes have been implemented.

OH is detected using REMPI via the $D\,^2\Sigma^-$ or the $3\,^2\Sigma^-$ state using the 225 to 246 nm spectral region [139,140]. Beames et al. reported a new REMPI detection scheme for OH, via the well characterized $A\,^2\Sigma^+ \leftarrow X\,^2\Pi$ system in combination with vacuum ultraviolet ionization via autoionizing Rydberg states that converge on the OH$^+$ $A\,^3\Pi$ ion state [141]. However in this thesis REMPI was not used for the detection of OH.

For the NO molecule REMPI is a very efficient detection method using the same excitation as for LIF to the $A\,^2\Sigma^+$ state at 226 nm. State-of-the-art lasers provide enough power to drive both, the excitation and ionization step in such (1+1) REMPI scheme. But also (1+1') REMPI schemes are established using two lasers. The prime denotes the different wavelength in use, i.e. different lasers, to excite or ionize the molecules. (1+1') REMPI can be more efficient when the ionization laser is either a fixed wavelength laser with more pulse energy than the tunable excitation laser, or when the ionization laser is set at a wavelength at the ionization threshold. Another benefit of two lasers, if these two lasers are shot from different directions, is the more precise definition of the detection region than for one laser. Figure 2.9 shows an example of two REMPI schemes for NO. The (1+1') REMPI shows a signal increase of almost two orders of magnitude.

Chapter 3

Scattering of OH radicals with He atoms and D_2 molecules

In this chapter the results on the scattering of Stark-decelerated OH ($X\,^2\Pi_{3/2}$, $J = 3/2, f$) radicals with He atoms and D_2 molecules in a crossed beam experiment are presented. At the end of the chapter a short outlook is given on how the collision energy can be reduced, and the energy resolution can be improved, in future experiments.

Based on:
Low-energy inelastic collisions of OH radicals with He atoms and D_2 molecules,
M. Kirste, L. Scharfenberg, J. Kłos, F. Lique, M. H. Alexander, G. Meijer, and S. Y. T. van de Meerakker, Phys. Rev. A **82**, 042717, 2010.

3.1 Introduction

The crossed molecular beam method has played an important role in the development of molecular reaction dynamics [126]. Ingenious methods for the detection and preparation of molecular collision partners have been developed to study molecular encounters under single collision conditions [39]. The molecular interaction or chemical reaction is in general governed by the potential energy surface (PES). Thus the experimental probe of potential energy surfaces and their theoretical calculation have been a challenging but nevertheless fertile approach for the present understanding of how intermolecular potentials govern molecular collision dynamics.

Different laser based detection methods such as ion imaging [57, 58, 59, 60] Rydberg H-atom time of flight (HRTOF) [61, 62, 63, 64], Doppler selected time of flight [65], as well as the photoloc technique [66, 67] have been used to analyze the state, angular and velocity distributions of the products after the collision. In these experiments the state-to-state integral (ICS) and differential cross section (DCS) provide a very sensitive probe of the PES.

In crossed molecular beam experiments not only the state, angle and velocity resolved detection of products, but also the preparation of molecules in single quantum states prior to the collision using electric, magnetic, or optical fields has been imperative to unravel the underlying mechanisms of molecular energy transfer. For atom-molecule collisions these methods have made scattering experiments possible at the full state-to-state level, and have resulted in the understanding of propensity rules for rotational energy transfer [82, 84, 142], the stereodynamics of molecular collisions [37, 143], and quantum interference effects [47, 48, 53, 70, 71, 88, 144, 145].

Recently, the well known technique of cross beam scattering has been combined with the technique of Stark deceleration [82, 84]. Compared to conventional molecular beams, Stark-decelerated beams have a narrower velocity spread, perfect quantum state purity, and a computer controlled velocity. The latter allows for a continuous variation of the collision energy. In the first scattering experiment using a Stark decelerator [82], OH radicals were scattered with a supersonic beam of Xe atoms under 90° angle of incidence. Recently a new, superior Stark decelerator was built [83], and with this decelerator experiments on the system OH-Ar were performed with a better sensitivity [84]. In both systems, OH-Xe and OH-Ar, the relative inelastic cross sections as a function of the collision energy were measured and clear threshold behavior was observed. The experimental cross sections were compared with cross sections determined by quantum close-coupling calculations based on high-quality ab initio OH-Xe and OH-Ar potential energy surfaces, and excellent agreement was obtained [82, 84].

In another experiment, magnetically trapped OH radicals were scattered with supersonic beams of He atoms and D_2 molecules [85]. By changing the temperature of the He and D_2 beam source, the collision energy was varied from 65 to 230 cm^{-1} for collisions with He and from 145 to 510 cm^{-1} for collisions with D_2.

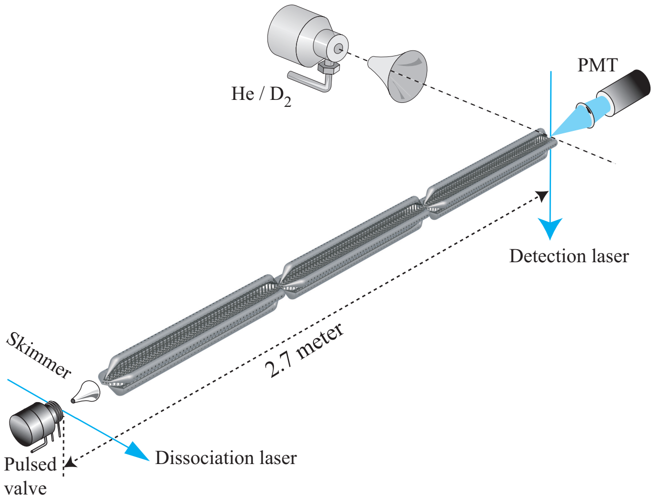

Figure 3.1: Scheme of the experimental setup. A pulsed beam of OH radicals is produced via photodissociation of HNO_3 seeded in an inert carrier gas. The OH radicals pass through a 2.6-m-long Stark decelerator, and are scattered with a pulsed beam of He atoms or D_2 molecules. The OH radicals are state-selectively detected via laser-induced fluorescence, that is recorded with a photomultiplier tube (PMT).

In this experiment information on the total collision cross sections was inferred from the beam-induced trap loss that occurs through elastic as well as inelastic collisions.

In this chapter an experiment on the collisions of Stark-decelerated OH ($X\,^2\Pi_{3/2}, J = 3/2, f$) radicals with He atoms and D_2 molecules in a crossed beam experiment is presented.

3.2 Experimental setup

The experiments are performed in a crossed molecular beam machine that is schematically shown in Figure 3.1. The exact same machine has been used to study the rotational energy transfer in collisions between state-selected OH ($X\,^2\Pi_{3/2}, J = 3/2, f$) radicals and Ar atoms and in collisions between state-selected OH ($X\,^2\Pi_{3/2}, J = 3/2, f$) radicals and Xe, Ne, and Kr atoms [84,146]. A detailed description of the apparatus, its design, and all its components is given elsewhere [125]. Here a brief summary is given.

A pulsed supersonic beam of OH radicals in the $X\,^2\Pi_{3/2}, J = 3/2$ state is produced by photolysis (193 nm) of nitric acid seeded in an inert carrier gas. Due to the expansion the molecules are cooled to the lowest rotational and vibrational levels of the $X\,^2\Pi$ ground state. The lowest rotational level ($J = 3/2$) consists of two Λ-doublet components labeled e and f. After passing a 2 mm diameter skimmer the OH radicals enter a 2.6 m long decelerator consisting of 317 parallel pairs of high-voltage electrodes. The OH radicals that reside in the upper Λ-

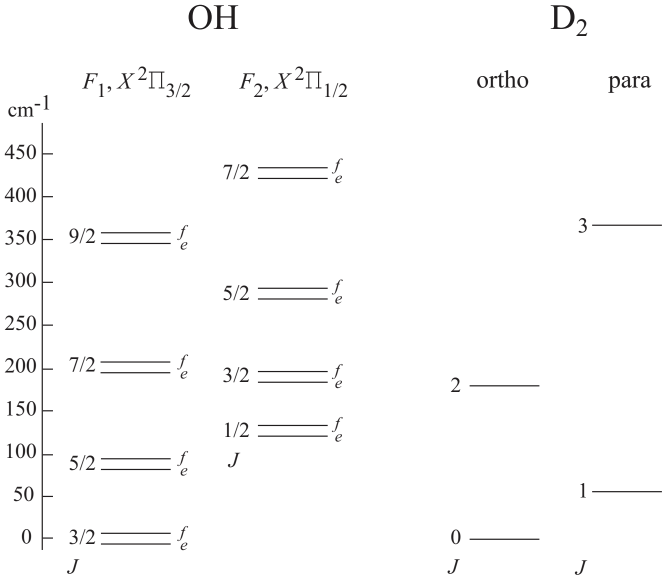

Figure 3.2: Rotational energy level diagram of the OH radical (left) and the D_2 molecule (right). The rotational states are labeled with the rotational quantum number J. The spectroscopic symmetry labels e and f are used to denote the two Λ-doublet components that exist for every rotational state of OH. The splitting between both components is largely exaggerated for reasons of clarity.

doublet component of f parity are decelerated, guided, or accelerated with the use of the Stark decelerator running in the so-called $s = 3$ operation mode [83, 147]. The OH radicals are scattered with a neat beam of He atoms or D_2 molecules at a distance of 16.5 mm from the exit of the decelerator. The He and the D_2 beams are produced by supersonic expansion from a solenoid valve residing 90 mm from the point of intersection. The He and the D_2 beams are skimmed with a 2 mm diameter skimmer. The beams scatter under 90° angle of incidence and collisions take place in a field free region. The density of the He and D_2 molecular beams is kept sufficiently low to measure in single collision conditions. This is ensured by measuring the depletion of the incoming OH beam after scattering with the He and D_2.

The beam of D_2 molecules is produced using a gas of normal D_2, and both ortho-D_2 and para-D_2 molecules contribute therefore to the measured state-to-state inelastic cross sections. According to the statistical weights, 67% and 33% of the D_2 molecules are expected to reside in a rotational state belonging to ortho and para-D_2, respectively. The rotational energy level diagram of D_2 is schematically shown in Figure 3.2. The energy level spacing between the lowest rotational states is large, and the D_2 molecules are expected to predominantly reside in the $J = 0$ and the $J = 1$ levels.

The collision energy is varied by tuning the velocity of the OH radicals, and by choosing different temperatures for the solenoid valve used to produce the He and D_2 beams. The mean forward velocity of the He/D_2 beam is measured by two microphone based beam detectors placed 300 mm apart. For a given temperature of the valve, similar beam speeds are measured for He and D_2 as is to be expected for beam particles of identical mass (4 atomic units). The lowest collision energies are obtained when the solenoid valve is cooled to near liquid nitrogen temperatures, resulting in a minimum mean beam velocity of 996 m/s for He and 1042 m/s for D_2. The slightly higher speeds that are measured for D_2 beams are attributed to the extra degrees of freedom of the D_2 rotor compared to He, see Chapter 2.4.

The lowest collision energy is 120 cm^{-1} and 150 cm^{-1} for OH-He and OH-D_2, respectively. Collision energies up to 400 cm^{-1} for OH-He and 500 cm^{-1} for OH-D_2 are reached by tuning the velocity of the OH radicals between 168 and 741 m/s, and by using temperatures of 293 K, 253 K, 213 K, 173 K, 133 K, and 93 K for the valve producing the He/D_2 beam. The width (full width at half maximum) of the collision energy distribution depends on the velocity distribution and angular spreads of both beams. These are accurately known for the OH radicals from simulations of the deceleration process [76, 125]. These Monte Carlo trajectory simulations start with a Gaussian 6D phase space distribution. The equations of motions are calculated from the known Stark energy of the OH molecules. The simulation is performed with finite time steps and the equations of motions are approximated with RungeâĂŞKutta methods. For the He and D_2 beams the velocity distributions and angular spreads are estimated from the microphone measurements. The collision energy distribution is calculated by estimating the differential of Equation 2.77:

$$dE_c = \mu[(v_1 - v_2 \cos\phi)dv_1 + (v_2 - v_1 \cos\phi)dv_2 + v_1 v_2 \sin\phi d\phi]. \tag{3.1}$$

The collision energy distribution ranges from $\approx$ 20 cm^{-1} at the lowest collision energies to $\approx$60 cm^{-1} at the highest collision energies.

Collisional excitation of the OH radicals up to the $X\,^2\Pi_{3/2}, J = 9/2$ and the $X\,^2\Pi_{1/2}, J = 7/2$ state (data not shown) is measured. These rotational states are schematically shown in the rotational energy level diagram in Figure 3.2. Spin-orbit conserving and spin-orbit changing transitions are measured. The rotational levels are referred to as $F_{1,2}(Je/f)$, where F_1 and F_2 are used to indicate the $X\,^2\Pi_{3/2}$ and the $X\,^2\Pi_{1/2}$ spin-orbit manifolds, respectively. The inelastically scattered OH radicals are state-selectively detected via saturated Laser Induced Fluorescence (LIF) using different rotational transitions of the $A\,^2\Sigma^+, v = 1 \leftarrow X\,^2\Pi, v = 0$ band. The laser radiation at 282 nm is produced from a frequency doubled pulsed dye laser (PDL) with bandwidth of 0.06 cm^{-1}. The off-resonant fluorescence at 312 nm is collected at right angles and imaged into a photomultiplier tube (PMT). The laser radiation is linearly polarized. Scharfenberg et al. demonstrated that a rotation of the polarization axis does not change the measured intensities [84], i.e. the fluorescence is emitted isotropically. The diameter of the laser beam is approximately 8 mm, providing a detection volume that is larger than the intersection volume of both beams.

The experiment runs at a repetition rate of 10 Hz. The beam that provides the collision partner is operated every second shot of the experiment, and the

		e		f	
	J	transition	ϵ	transition	ϵ
F_1	$\frac{3}{2}$	P_1	$\frac{1}{3}$	$Q_1 + Q_{21}$	$\frac{3}{5}$
	$\frac{5}{2}$	P_1	$\frac{2}{5}$	Q_1	$\frac{1}{2}$
	$\frac{7}{2}$	P_1	$\frac{3}{7}$	Q_1	$\frac{1}{2}$
	$\frac{9}{2}$	P_1	$\frac{4}{9}$	Q_1	$\frac{1}{2}$
F_2	$\frac{1}{2}$	$Q_2 + Q_{12}$	$\frac{3}{4}$	P_{12}	$\frac{1}{2}$
	$\frac{3}{2}$	Q_2	$\frac{1}{2}$	$P_{12} + P_2$	$\frac{3}{5}$
	$\frac{5}{2}$	Q_2	$\frac{1}{2}$	P_{12}	$\frac{1}{2}$

Table 3.1: Excitation rates of selected transitions in the OH $A\,^2\Sigma^+, v = 1 \leftarrow X\,^2\Pi, v = 0$ band, adapted from [84]. The excitation rates can be calculated following Equation 2.90.

collision signal results as the signal intensity difference of alternating shots of the experiment. For cross section close to zero this sometimes results in negative values. The collision energy is varied in a quasi-continuous cycle for each temperature setting of the He/D2 valve. For each temperature an interval of different collision energies, i.e. different OH velocities and different phase angles ϕ in the decelerator, is measured. For each collision energy the Stark decelerator is operated at a certain phase angle ϕ and the OH LIF signal is recorded for the two alternating shots. To avoid long term drifts of the experiment, e.g. a drift of the beam intensity after the supersonic expansion, the intervals are cycled from low to higher collision energies and then back from higher to lower. Each cycle is measured for each scattering channel 500 to 1500 times.

For the strongest scattering channels, the fluorescence signals are recorded using an analog mode of detection; the weak signals are analyzed using photon counting. A linear relation is found between both modes of signal acquisition, by measuring those channels, in which the analog and the photon counting mode of detection is possible. The measured scattering signals are the arithmetic mean of all repetitions of the experiment. The error is estimated from the standard error of the mean: $u = \frac{s}{\sqrt{n}}$, with s being the standard deviation and n the number of observations. Note that u is also referred to as uncertainty. The measured scattering signals are transformed into relative populations by dividing the signal of each channel for each collisions energy by the sum of all channels at that same energy.

To relate the measured signal intensities to collision induced populations, the different excitation rates for the different branches of the optical transitions used to probe the different rotational levels are taken into account in the data analysis. The excitation rates are adapted from [84] and shown in Table 3.1. They can easily be calculated following Equation 2.90.

The measured relative populations in the various rotational states directly reflect inelastic cross sections. No density-to-flux transformation is required for crossed beam scattering experiments using a light particle as collision part-

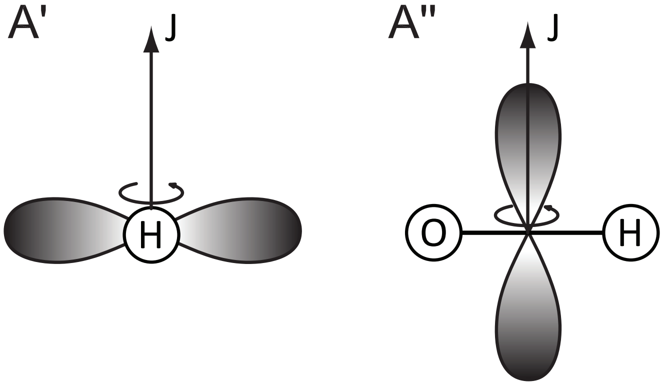

Figure 3.3: Schematic representation of the molecular orbital having A' and A'' symmetry. The figure is adapted from [39].

ner [148] (see Chapter 5 for the density-to-flux problem). The validity of this assumption is verified by a measurement of the variation of the relative collision signals as a function of time in the overlapping beams. No variation was recorded in the experiment.

3.3 Theoretical evaluation of OH-He cross sections

The interaction between the open shell OH($X\,^2\Pi$) radical and a spherical He atom is described by two PES's: $V_{A'}$ and $V_{A''}$, having A' and A'' reflection symmetry in the plane containing the OH radical and the He atom [149]. The PES of A' and A'' symmetry describes the OH-He interaction where the OH radical has its singly occupied π orbital in, and perpendicular, to the triatomic plane, respectively, as shown in Figure 3.3. In scattering calculations it is more convenient to construct the average potential $V_{\text{sum}} = 1/2(V_{A''} + V_{A'})$ and the half-difference potential $V_{\text{dif}} = 1/2(V_{A''} - V_{A'})$ of these PES's [149,150].

Fully quantum, close-coupling scattering calculations of inelastic collisions of OH radicals with He atoms have been performed recently by Kłos et al. [151] based on the RCCSD(T) potential energy surfaces of Lee et al. [152]. Kłos et al. present, cross sections for rotational transitions out of the $F_1(3/2e)$ state; for the present experiment transitions out of the $F_1(3/2f)$ state are of relevance. Therefore the HIBRIDON program suite was used to carry out fully-quantum, close-coupling calculations of integral state-to-state scattering cross sections [153]. The channel basis was chosen to ensure convergence of the integral cross sections for all $J, F_i \rightarrow J', F_i'$ transitions with $J, J' \leq 11.5$. The calculated inelastic cross sections were converged to within 0.01 Å^2 [154].

The calculations yield elastic as well as inelastic cross sections and absolute differential (DCS) as well as absolute integral cross sections (ICS). The ICS's are converted into relative cross sections and compared to the experiment.

3.4 Results

In Figures 3.4 and 3.4, the measured relative state-to-state inelastic scattering cross sections to levels in the F_1 manifold (spin-orbit conserving collisions) and the F_2 manifold (spin-orbit changing collisions), respectively, are shown. The cross sections that are obtained for the collision partners He and D_2 are displayed in the left and right hand side of these Figures. The scattering channels that correspond to excitation of the OH radicals to the two different Λ-doublet components of a given rotational state are grouped together. In the upper panels, the scattering channel that populates the $F_1(3/2e)$ state is shown together with the channels that populate both Λ-doublet components of the $F_1(5/2)$ rotational state. To facilitate a direct comparison between the scattering cross sections for OH-He and OH-D_2, identical axes are used in the panels that correspond to the same scattering channels. The theoretically calculated cross sections for the scattering of OH with He, convoluted with the experimental energy resolution, are included as solid curves in the left panels.

3.4.1 OH-He

In the collision energy range that is probed, the rotational inelastic scattering of OH ($F_1(3/2f)$) radicals with He atoms is dominated by excitation to the $F_1(5/2e)$ state. The $F_1(3/2e)$ channel, corresponding to collisions that induce the $J = 3/2, f \rightarrow J = 3/2, e$ Λ-doublet transition in the OH radical, appears rather weak. This is in contrast with the scattering of OH radicals with Ar and Xe atoms for which the $F_1(3/2e)$ channel is the dominant inelastic scattering channel [82, 83]. The scattering channel populating the $F_2(1/2e)$ state appears exceptionally large, also at variance with the corresponding cross sections for the collision partners Ar and Xe.

For spin-orbit manifold conserving collisions, there is a strong propensity for final states of e parity. For spin-orbit manifold changing collisions populating the $J = 1/2$ and $J = 3/2$ states, very strong propensities are observed, showing a near symmetry selection rule. Collisions that populate the $F_2(1/2e)$ and $F_2(3/2f)$ states are approximately two orders of magnitude more effective than collisions populating the $F_2(1/2f)$ and $F_2(3/2e)$ states, respectively.

At high collision energies, the relative state-to-state cross sections and the propensities are consistent with the observations by Schreel *et al.* [44]. In that experiment, however, the strong propensities were partially concealed due to a sizable initial population in the $F_1(5/2f)$ state [44]. The almost perfect quantum state purity of the packets of OH radicals that are used in the present experiment enables the unambiguous measurement of the cross sections of transitions to final states that are only weakly coupled to the $F_1(3/2f)$ initial state.

The energy range that is probed encompasses the energetic thresholds for scattering into all rotationally excited states, except for the scattering into the $F_1(5/2e)$ and $F_1(5/2f)$ states which open at a collision energy of 84 cm^{-1}. Throughout the range of collision energies, a good agreement is found with the computed cross sections. The relative scattering cross sections, the propensities for transitions to one of the Λ-doublet components of the final rotational state, as well as the threshold behavior of the various channels are reproduced well. The largest difference between theory and experiment is found for the $F_2(1/2e)$ channel.

The scattering calculations provide quantitatively the state-to-state scattering cross sections, but do not reveal the physical origin of the general behavior of the scattering cross sections and in particular the Λ-doublet propensities. A general analysis of the scattering of $^2\Pi$ molecules with spherical objects has been developed by Dagdigian et al. [155], and can be used to qualitatively understand the inelastic scattering of OH radicals with atomic collision partners [46, 156]. From the formal quantum analysis of the scattering, it follows that the coupling between rotational states can be evaluated from

$$\sum_l K^l \left[A^l_{\Omega' J' \epsilon', \Omega J \epsilon} V_{l0} + B^l_{\Omega' J' \epsilon', \Omega J \epsilon} V_{l2}\right] \tag{3.2}$$

where J is the rotational quantum number of the OH radical, ϵ is the symmetry index of the rotational state, and Ω is the projection of J onto the internuclear axis. Primed quantum numbers indicate the post-collision conditions. The terms V_{l0} and V_{l2} are the expansion coefficients of the average and difference potentials in terms of regular and associated Legendre polynomials, respectively. The sum in equation (3.2) is performed over the expansion index l.

The factor K^l is only nonzero for states that are coupled by the interaction potential, and needs for this analysis no further discussion. Essential in the understanding of the inelastic cross sections are the values for the V_{l0} and the V_{l2} coefficients, and the role of the A^l and B^l factors. Both A^l and B^l are independent of the interaction potential, and are determined exclusively by the rotational energy level structure of the molecule. The values of A^l and B^l for OH radicals in the $X\,^2\Pi_{3/2}, J = 3/2, f$ level are tabulated in Ref. [155], and are reproduced in Table 3.2 for excitation into the four lowest lying rotational states.

For a pure Hund's case (a) molecule, the values for B^l are zero for spin-orbit manifold conserving collisions, whereas the factors A^l are zero for spin-orbit manifold changing collisions. Consequently, spin-orbit conserving and spin-orbit changing transitions are induced exclusively by V_{sum} and V_{dif}, respectively. Within each manifold, e/f parity changing collisions are governed by the terms for which $\Delta J + l = \text{odd}$, while e/f parity conserving collisions are described by the $\Delta J + l = \text{even}$ terms. The propensities for preferred excitation to the e or f component of a final rotational state originate from the different values for the relevant products $A^l V_{l0}$ or $B^l V_{l2}$ that govern these transitions.

For molecules like OH that cannot be described by a pure Hund's case (a) coupling scheme, both the factors A^l and B^l are nonzero, and interference between the average and difference potentials occurs. The $X^2\Pi$ electronic ground state of the OH radical originates from a π^3 electron occupancy, leading to predominantly positive values for V_{sum} and V_{dif} [155, 156]. As a result, final states for which the dominant A^l and B^l factors have equal signs are coupled more strongly to the $F_1(3/2f)$ initial state than final states for which A^l and B^l have opposite signs.

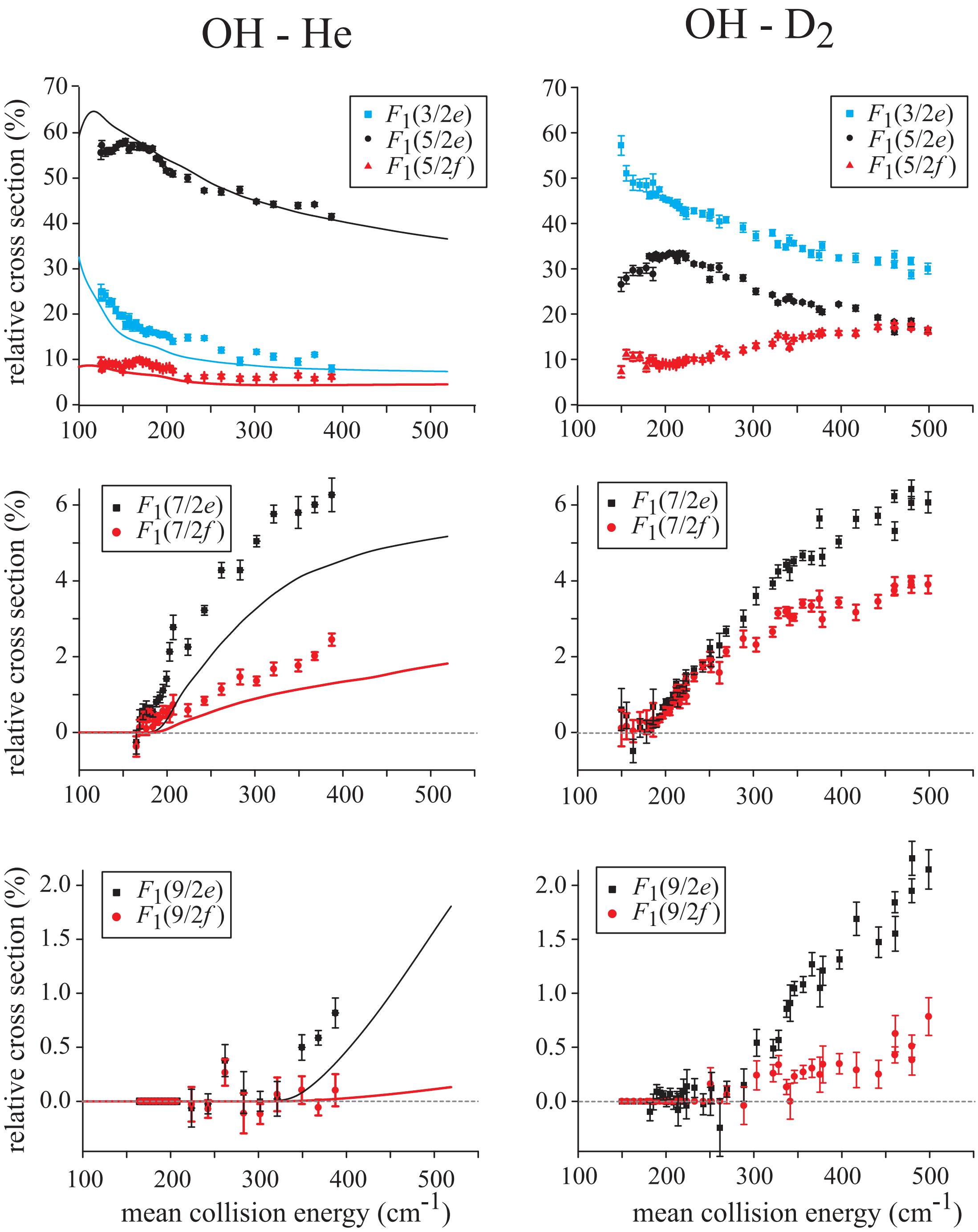

Figure 3.4: Relative state-to-state inelastic scattering cross sections for spin-orbit conserving ($F_1 \rightarrow F_1$) collisions of OH ($X\,^2\Pi_{3/2}, J = 3/2, f$) radicals with helium atoms (left) and D_2 molecules (right). The theoretically calculated cross sections for the scattering of OH with He from Ref. [151] are included as solid curves in the left panels.

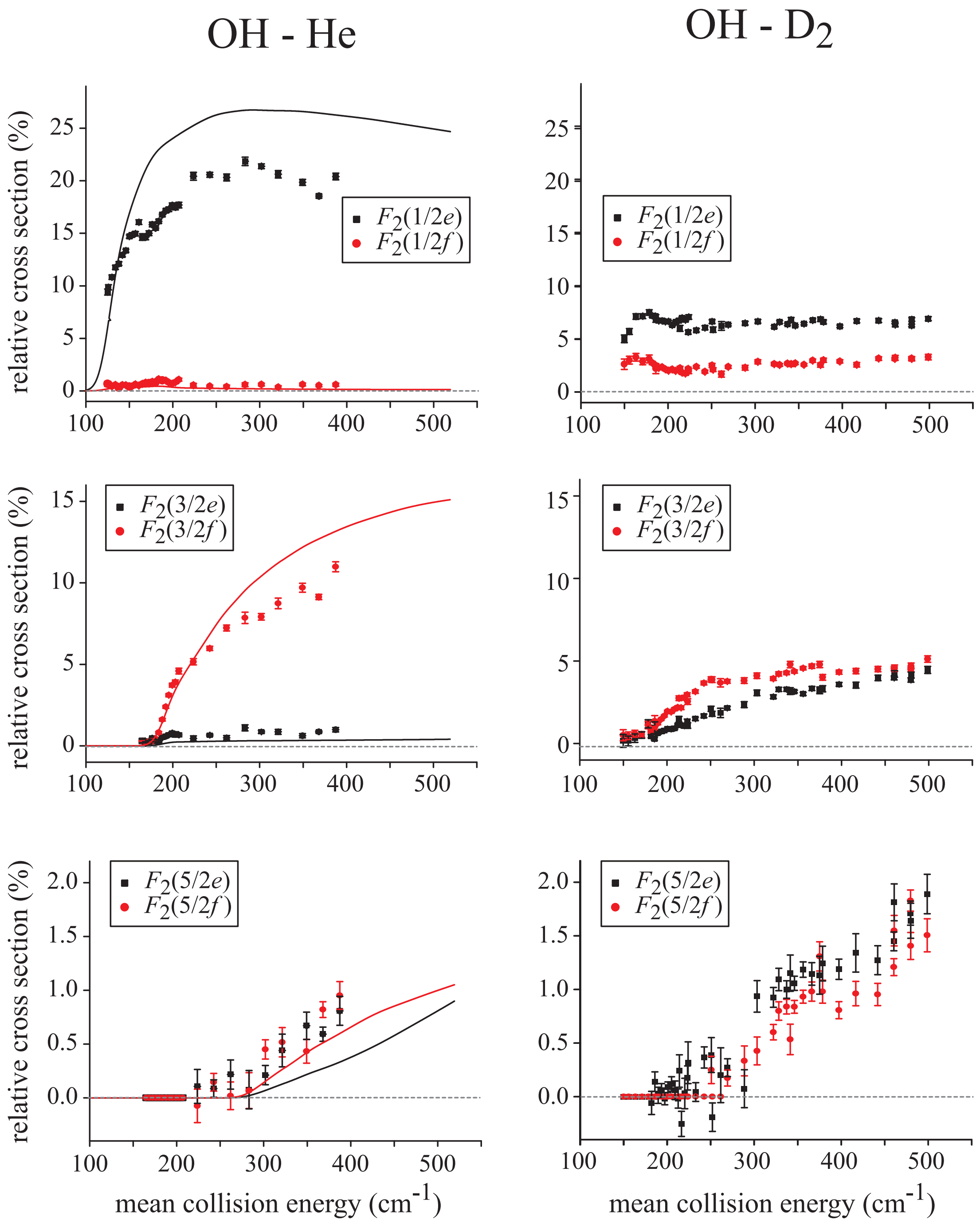

Figure 3.5: Relative state-to-state inelastic scattering cross sections for spin-orbit changing ($F_1 \rightarrow F_2$) collisions of OH ($X\,^2\Pi_{3/2}, J = 3/2, f$) radicals with helium atoms (left) and D_2 molecules (right). The theoretically calculated cross sections for the scattering of OH with He from Ref. [151] are included as solid curves in the left panels.

Final state			Λ-doublet transition			
			$f \rightarrow f$		$f \rightarrow e$	
	J	l	A^l	B^l	A^l	B^l
F_1	$\frac{3}{2}$	0	-0.50	0	0	0
		1	0	0	-0.38	0
		2	-0.21	0.11	0	0
		3	0	0	-0.07	0
F_1	$\frac{5}{2}$	1	0.26	0	0	0
		2	0	0	0.28	0.09
		3	0.19	-0.09	0	0
		4	0	0	0.07	0.01
F_2	$\frac{1}{2}$	1	-0.07	0	0	0
		2	0	0	-0.06	0.44
F_2	$\frac{3}{2}$	1	0	0	0.05	0
		2	0.08	0.30	0	0
		3	0	0	0.06	-0.27

Table 3.2: Values of the coefficients A^l and B^l for excitation of OH ($X\,^2\Pi_{3/2}, J = 3/2, f$) radicals into the lowest lying rotational states (values reproduced from Ref. [155]).

The former is the case for the final states of e parity in the F_1 spin-orbit manifold, and for final states of f parity in the F_2 manifold, contributing to the observed propensities. The anomalous propensity that is observed for the $F_2(1/2e)$ state can be understood from equation (3.2). Excitation into the $F_2(1/2f)$ state is governed exclusively by V_{10} in combination with a small value for A (A = -0.07), while the V_{22} term in combination with a large value for B (B = 0.44) dominates the excitation into the $F_2(1/2e)$ state [155, 156]. As pointed out by Espoti et al., the qualitative analysis given above works well for excitation into rotational states with low J only; for excitation to higher J a qualitative analysis based exclusively on the A^l and B^l coefficients is not straightforward [156].

The measured relative state-to-state cross sections directly yield qualitative information on the expansion coefficients of the potential energy surfaces that govern the scattering between OH and He. Collisions that populate the $F_1(3/2e)$ and $F_1(5/2f)$ states are governed by the coefficients for which l = odd, while the cross sections for excitation to the $F_1(5/2e)$ state is governed by the l = even coefficients. The observed ratio of the state-to-state cross sections indicates that the leading l = even terms V_{20}, V_{40}, and V_{22} contribute significantly to the interaction potential. The relatively large cross section for spin-orbit changing collisions populating the $F_2(1/2e)$ state, as well as the strong propensities that are generally observed, suggests that the V_{22} coefficient of the difference potential plays a significant role in the scattering between OH radicals and He atoms. These effects can be rationalized by the nature of the OH-He interaction potential. The interaction between OH and He is rather weak and the anisotropy of the potential energy surface is small. The $V_{A''}$ PES has two shallow and almost equally deep potential wells for the collinear OH-He and the HO-He geometry, with well depths of 27 cm^{-1} and 22 cm^{-1}, respectively [152]. Consequently, the $l =$ even coefficients that describe the head-tail symmetric parts of the potential energy surfaces contribute significantly to the scattering.

3.4.2 OH-D_2

The inelastic scattering of OH radicals with D_2 molecules shows interesting differences compared to OH-He. The largest cross section is observed for collisions that populate the $F_1(3/2e)$ state. For the channels that populate the $F_1(5/2)$ states, a propensity for the Λ-doublet component of e symmetry is observed for low collision energies, that vanishes for collision energies of about 500 cm^{-1}. The other scattering channels show only modest propensities. The spin-orbit changing collisions appear rather weak.

Although the formalism that was applied above to the scattering of OH with He does not strictly apply to non-spherical collision partners, the formalism can be used to obtain a physical interpretation of the differences between the scattering of OH with He and D_2. This comparison is particularly interesting, as both collision partners have equal mass, and mass effects in the dynamics cancel. The interaction of D_2 molecules with OH radicals is stronger and induction forces are more important than for the interaction between OH and He. This suggests that the PES is less head-tail symmetric in comparison to OH-He, and the coefficients of the potential for which $l =$ odd gain importance compared to the $l =$ even coefficients. This results in a larger cross section for Λ-doublet changing collisions populating the $F_1(3/2e)$ state, smaller spin-orbit changing transitions, and less pronounced propensities for preferred excitation to one of the two components of a Λ-doublet. Similar effects have been observed in state-to-state inelastic scattering experiments of OH radicals with polar collision partners such as HCl [157], HBr [158], and HI [159], and also CO_2 [160].

In the relative inelastic scattering cross sections, no effect is seen from the internal rotational degrees of freedom of the D_2 molecule. In contrast to the work by Sawyer et al. [85], no strong variation of the cross sections at collision energies around 300 cm^{-1} is observed, that could be indicative of resonant energy transfer between the OH and the D_2 rotors.

3.5 Conclusion

In this chapter the measurements of the state-to-state rotational inelastic scattering of Stark-decelerated OH ($X\,^2\Pi_{3/2}, J = 3/2, f$) radicals with He atoms and D_2 molecules are presented. The collision energy dependence of the relative inelastic scattering cross sections, in the collision energy range 100-500 cm^{-1}, the threshold behaviour of inelastic channels, and the energy dependence of the state-resolved propensities are accurately determined. For the scattering of OH with He, good agreement is found with the inelastic scattering cross sections determined from quantum close-coupled scattering calculations based on high-quality

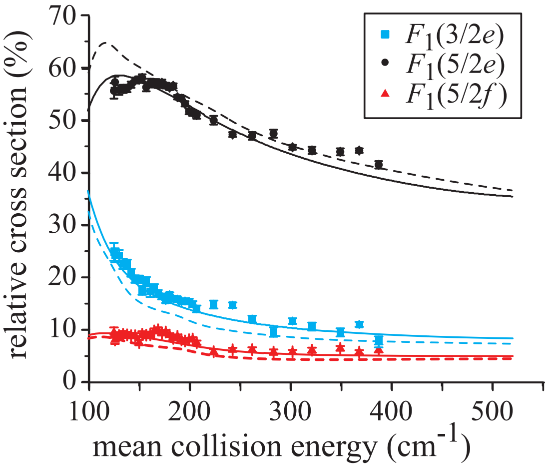

Figure 3.6: Relative state-to-state inelastic scattering cross sections for spin-orbit conserving ($F_1 \rightarrow F_1$) collisions of OH ($X\,^2\Pi_{3/2}, J = 3/2, f$) radicals with helium atoms. The theoretically calculated cross sections from Ref. [151] are included as dashed curves and the theoretically calculated cross sections from [161] are included as solid curves, with permission from Gubbels. The comparison shows an improved agreement between theory and experiment for the new ab initio PES's. The full comparison is found in [161].

ab initio OH-He PES's.

The almost perfect quantum state purity of the Stark-decelerated packets of OH radicals eliminates the contamination of the scattering signals by initial populations in excited rotational states. This facilitates a quantitative study of collision induced transitions to states that are only weakly coupled to the initial state, and enables the observation of the exceptionally strong propensities for the inelastic scattering between OH radicals and He atoms. The genuine relative state-to-state inelastic scattering cross sections that are measured allow for an accurate comparison with computed cross sections.

Significant differences are found between the inelastic scattering of OH-He and OH-D_2. Although no rigorous quantum calculations have been performed for OH-D_2, these differences can be understood from the different nature of the OH-D_2 interaction potential. No effect of the rotational degrees of freedom of the D_2 molecule has been observed in the relative inelastic scattering cross sections.

Recently, new ab initio PES's have been calculated for OH-He by Gubbels et al. [161]. The cross sections derived from these surfaces agree even better with the experimental findings, Figure 3.6, than what has been presented in this chapter. This improved agreement between theory and experiment demonstrates the importance of the study of the fully state resolved scattering.

OH-He is a well-suited system to improve the energy resolution in the scattering process, since scattering resonances are believed to be pronounced in this system [151,161]. Recently the possibilities to improve the energy resolution in a crossed beam study with a Stark decelerator have been investigated by Scharfenberg et al. [162]. Especially reducing the angle between the two beams can significantly improve the energy resolution down to a few wavenumbers. Scharfenberg et al. state, that for systems with a small reduced mass, absolute collision energy resolution ranging from 0.5 to 5 cm^{-1} are feasible. Currently (2012) an experiment with improved energy resolution on the scattering of OH-He is performed at the Fritz Haber Institute in Berlin. But even with high energy resolution, it remains experimentally challenging to observe scattering resonances. For OH-He the energy distribution has to be below 0.5 cm^{-1} to attribute a measured structure in the energy dependence of the scattering signal to scattering resonances [161]. As the authors pointed out in [161], an alternative approach to measure scattering resonances is the measurement of the DCS.

Chapter 4

A compact hexapole state-selector for NO radicals

This Chapter contains a short historical overview of molecular beam experiments using hexapoles. Afterwards a general discussion of hexapole focusing and detection is given. A new hexapole design, aimed at obtaining large focusing forces is introduced. Focusing and state-selection of NO radicals using this new hexapole design are reported.

Based on:
A compact hexapole state-selector for NO radicals,
M. Kirste, H. Haak, G. Meijer, and S. Y. T. van de Meerakker, unpublished manuscript.

4.1 Introduction

The technique of hexapole state-selection and focusing of polar molecules was pioneered by the groups of Bernstein and Brooks already in the 1960s [14,19,20]. Originally, their work aimed at observing and understanding steric effects in chemical reactions at the molecular level [21]. Over the years these techniques have been improved and applied in varies experiments. The hexapole technique has always been important in the general field of molecular beams [119]. It is well suited to state-select polar molecules that exhibit a linear Stark effect, reaching almost perfect selection of initial molecular states [36,163,164,165,166].

Because of this nearly perfect state-selection, the hexapole technique has been very successful in the investigation of collisions of polar molecules with rare gas atoms. In these crossed beam collision experiments the preparation of molecules in a single quantum state, prior to the collision, is essential for the measurement of state-to-state cross sections. Experiments in which hexapole state-selection has been used, lead to the understanding of propensity rules for rotational energy transfer [142], the stereodynamics of molecular collisions [143], dynamics of molecular stereochemistry [35], and quantum interference effects [47].

Prominent collision experiments have been performed already in the 1970s on the collisions of hexapole-selected open-shell radical species with rare gas atoms [22,23,34]. In particular NO and OH rare gas collision experiments benchmark the scattering of state-selected molecules with rare gas (Rg) atoms [38], and these experiments have strongly influenced our present understanding of how intermolecular potentials govern molecular collision dynamics [39]. Both molecules, the NO molecule [40,41,42] and the OH molecule [43,44,45,46] have been extensively studied in collision experiments, in which hexapole devices have been used. Overview articles about the state-selection and focusing of OH and OD radicals and of NO radicals with a hexapole, are found in [167] and [117], respectively.

Hexapoles have also been used to study molecule surface dynamics [36]. CF_3H was state-selected and scattered from a Ag surface [168], revealing a dependency on the surface temperature of the orientation of the molecules leaving the surface. A strong orientation dependency was shown when state-selected and oriented NO molecules scatter with Ag(111) [169,170], Pt(111) [171] and Ru-H [172] surfaces. Steric effects in the scattering of oriented CH_3F by graphite were measured [173]. And last, propensities for inversion symmetry change from antisymmetric to symmetric have been observed for the scattering of hexapole state-selected ND_3 molecules by graphite [174].

Wodtke and co-workers have reported experiments in which they combined hexapole focusing with stimulated emission pumping [51,52]. This combination provides control over the molecule's rovibronic quantum state, its velocity and its transverse divergence.

Recently hexapoles have been used to guide molecules in a so called molecular synchrotron [175]. In a molecular synchrotron the six hexapole rods are bent to a circle or two half circles forming a storage ring for polar molecules [176]. The molecules entering the ring are confined in the ring by the hexapole forces, for storage times on the order of seconds [177]. The half circles have been replaced by 40 small (40 mm long) hexapoles, in the newest molecular synchrotron design. In this molecular synchrotron multiple packets of neutral molecules have been stored for 13 sec, which corresponds to revolving a distance of over one mile in the synchrotron [178].

Not only electric fields can be used to state-select and focus polar molecules, but similar effects are achieved by exploiting the Zeeman interaction in a inhomogeneous magnetic field. Kurahashi et al. produced a single spin-rotational state-selected oxygen ($^3\Sigma_g^-$) beam with a hexapole magnet [179]. Their hexapole consists of six permanent magnets [180].

In this work, a new experiment on bi-molecular scattering was planned, namely to scatter a beam of Stark-decelerated OH ($X\,^2\Pi_{3/2}, v = 0, J = 3/2, f$) radicals with a beam of state-selected NO ($X\,^2\Pi_{1/2}, v = 0, J = 1/2, f$) radicals. For this purpose a new hexapole device was designed.

The new hexapole device is designed to state-select NO radicals in the ($X\,^2\Pi_{1/2}, v = 0, J = 1/2, f$) ground state. Due to the small dipole moment of the NO radical, of only 0.159 Debye, larger electric fields or longer focusing paths are needed to focus NO, than to focus for instance the OH radical, which has a dipole moment of 1.67 Debye. Thus far hexapoles of several meters in length have been used. For the OH-NO collision experiment it is essential to reach large number densities for both collision partners. The hexapole technique, in contrast to the technique of Stark deceleration, keeps the molecular packet only transversely but never longitudinally together. Thus in a collision experiment with a long distance from the source to the interaction region, the molecular packet blurs out along the beam path, reducing the number density in the interaction region. Hence the goal of the hexapole design described here, is to focus and state-select NO molecules in the distance that is as short as possible.

4.2 Hexapole focusing

Polar molecules experience a force in an inhomogeneous electric field, caused by the Stark interaction, which has been described in Chapter 2.3. Depending on their quantum state, the molecules are driven to a field minimum, when in a low-field seeking state, or a field maximum, when in a high-field seeking state. Focusing of high-field seeking molecules is technically challenging, because Maxwell's equations forbid a global electric field maximum with static field alone. Instead a scheme called alternating-gradient (AG) focusing [181] has been developed to focus [26,182,183] and guide high-field seeking molecules dynamically [184,185,186]. A detailed description of AG guiding and focusing of high-field seeking molecules can be found in [187,188].

Creating a field minimum for low-field seeking molecules is straightforward. Static electric fields are created by applying high voltages to a certain electrode geometry, which is aligned around the molecular beam axis. Either quadrupole

[11, 12, 13] or hexapole geometries have been developed [14, 19, 20]. The main difference between a hexapole and a quadrupole field, created by these geometries, is the dependence of the electric field strength E on the distance r from the center, i.e. the molecular beam axis. For a quadrupole field E depends linearly on r and for a hexapole field E depends quadratically on r. The Stark interaction, which results in a shift of the molecular energy, can in turn depend also linearly and quadratically on E. The focusing force for polar molecules in an electric field depends on the negative gradient of this Stark shift.

$$\boldsymbol{F} = -\nabla E_{\text{Stark}}. \tag{4.1}$$

To obtain a molecule optical element that exerts a harmonic force, i.e. a lens, the dependency of the electric field on r has to be linear for a quadratic Stark effect and quadratic for a linear Stark effect. Thus, inserting all dependencies into Equation 4.1, shows that a quadrupole field is best suited for molecules with a quadratic Stark effect and a hexapole field is best suited for molecules with a linear Stark effect.

The Stark shift of the NO molecule is given in Equation 2.62

$$E_{\text{Stark}} = \frac{E_\Lambda}{2} \pm \sqrt{\left(\frac{E_\Lambda}{2}\right)^2 + \left(\mu E \frac{M_J \Omega_{\text{eff}}}{J(J+1)}\right)^2}, \tag{4.2}$$

where the plus and minus sign are for the upper and lower Λ-doublet respectively. Note, that Equation 2.60 has been inserted in Equation 2.62 and that Ω_{eff} is given by Equation 2.61. For the NO ground state ($^2\Pi_{1/2}, v = 0, J = 1/2$), the value of Ω_{eff} is 1/2, see Table 2.1. For low electric fields the Stark shift is quadratic and for high electric fields it becomes linear, see Figure 2.4. In the high field limit the Stark shift becomes

$$E_{\text{Stark}} = \pm \mu E \frac{M_J \Omega_{\text{eff}}}{J(J+1)} \quad \text{(high field limit)}. \tag{4.3}$$

Thus a hexapole field, with its quadratic dependence on r, is best suited for the harmonic focusing of NO molecules.

The electrode geometry, which creates a hexapole field is called a hexapole. A hexapole consists of six cylindrical shaped electrodes, hereafter called rods, with a radius r_{rod} and a length l_{rod}. The six rods are aligned around the center with a distance r_0 from the rod's surfaces to the center. This distance is called the inner radius r_0 of the hexapole. The voltages are applied in alternating polarity to the six rods, see Figure 4.1, with $2V_0$ being the voltage difference between adjacent rods. For an ideal hexapole field the surface of the rods has to be hyperbolic [189], which is mechanically hard to achieve. An approximation to this ideal hexapole field has been given by Reuss [190], with a relation between rod radius and hexapole inner radius of $r_{rod} = r_0/2$. In two dimensional imaging experiments a deviation of this approximation from the ideal hexapole field has been observed [191]. Anderson [192] has calculated a better approximation of the

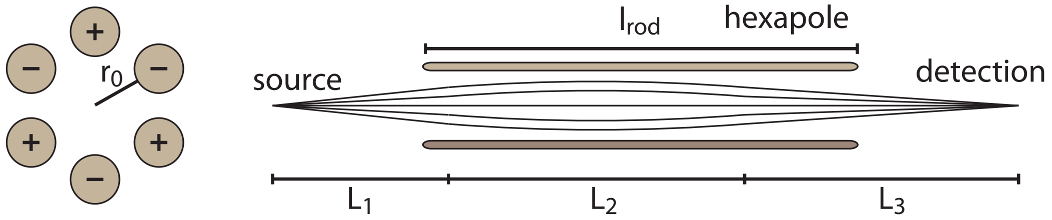

Figure 4.1: Left: Schematic representation of the six rods of a hexapole. The voltage $\pm V_0$ is applied to the rods in an alternating order. The inner radius r_0 of the hexapole spans from the center to the surface of the rods. Right: Schematic representation of the focusing curves of a hexapole, from the source to the focus. The first free-flight region, the focusing region and the second free-flight region are indicated by L_1, L_2, and L_3, respectively.

ideal hexapole field: $r_{rod} = 0.565 \cdot r_0$. In reference [189] and [77] a nice Figure is found, showing the difference between an ideal hexapole field, the design from Reuss, and the design from Anderson which is closest to the ideal case. The hexapole constructed in this thesis follows the design from Anderson.

An ideal hexapole acts as a perfect lens, imaging the molecular packet from the source to the detection. In a molecular beam experiment the source is a nozzle and the detection is performed by a detector for molecules, e.g. a PMT. The electric field inside the hexapole is created by the high-voltage, which is applied to the hexapole rods. The voltages are applied either static or via high-voltage switches. The trajectory of the molecules is strongly influenced, not only by the magnitude of the focusing force, but also by the temporal length and timings of the focusing force. In general the focusing force does not need to be applied during the entire flight of the molecules inside the hexapole. Instead the temporal length and timings of the focusing force are controlled via the timings of the high-voltage switches.

Three unique regions are defined along the molecular trajectory. In the first region of free-flight, the molecules do not yet experience the focusing force. The length of this region is the distance from the nozzle to the position where the hexapole is turned on, called L_1. The second region is within the hexapole. The molecules are within the second region, as long as they experience the focusing force. In contrast to an ideal thin lens in optics, the hexapole itself is not a thin lens, but has a certain focusing region, with length L_2. The last region is the second region of free-flight, when the hexapole is turned off, or the molecules left the hexapole field. The length of this region is called L_3, see Figure 4.1. Since the lengths L_1, L_2, and L_3 are the distances the molecules have traveled before, between, and after switching the hexapole on and off, respectively, they should not be confused with the physical distances of the experimental setup. For an identical 1:1 image one has $L_1 = L_3$.

The relation between L_1, L_2, and L_3 can be found in [22, 193]. Here, the so called matrix method, which is known from accelerator physics [194, 195], is used to derive the same relation. The matrix method has also been applied to polar molecules by Crompvoets [196] and Heiner [197], for the description of a molecular synchrotron. The idea of the matrix method is the following. The phase-space coordinates of a particle, i.e. its position and velocity, are transformed by transformation matrices from one point on the particle's trajectory to another. Each transformation matrix represents a certain region along the trajectory, e.g. a focusing region caused by a hexapole. The transformation matrix of the whole system is found by multiplying the transformation matrices of each individual region.

The most simple region is the free-flight of the molecules, represented by the following matrix

$$\begin{pmatrix} x_f \\ v_f \end{pmatrix} = \begin{pmatrix} 1 & t \\ 0 & 1 \end{pmatrix} \cdot \begin{pmatrix} x_i \\ v_i \end{pmatrix}. \tag{4.4}$$

The subscripts i and f denote the initial and final positions and velocities, respectively.

Because of the cylindrical symmetry of the hexapole field, one can transform the equation of motion into cylindrical coordinates with x being the longitudinal and r being the radial component. The longitudinal motion of the molecules is simple: $x = v_0 t$, with v_0 being the mean velocity of the Gaussian distribution of velocities of the molecular packet, see Chapter 2.4. This longitudinal velocity is not influenced by the hexapole. Therefore, the times t_1, t_2, and t_3, which are the time of free-flight before the hexapole, the time within the hexapole, and the time of free-flight after the hexapole, respectively, are defined by

$$t_1 = L_1/v_0, \quad t_2 = L_2/v_0, \quad t_3 = L_3/v_0. \tag{4.5}$$

The radial motion is best evaluated with the matrix method. The whole radial transformation matrix of molecules passing from a source through a hexapole to a detection, is given by a matrix for a region of free-flight, followed by a matrix M_{Hex}, representing the hexapole, and then followed by another matrix for a region of free-flight.

$$\begin{pmatrix} r_f \\ v_{r_f} \end{pmatrix} = \begin{pmatrix} 1 & L_3/v_0 \\ 0 & 1 \end{pmatrix} \cdot M_{Hex} \cdot \begin{pmatrix} 1 & L_1/v_0 \\ 0 & 1 \end{pmatrix} \cdot \begin{pmatrix} r_i \\ v_{r_i} \end{pmatrix}. \tag{4.6}$$

v_r is the radial velocity. For the evaluation of the matrix M_{Hex} one has to look at the radial force within the hexapole, which depends on the Stark shift. Instead of the gradient in Equation 4.1, the derivative, $F = -dE_{\text{Stark}}/dr$, of the Stark shift can be used to calculate the force on the molecules in the radial direction r. The Stark shift depends on the electric field of the hexapole via Equation 4.3, and the relation between the electric field magnitude and the voltage applied to the hexapole rods is for an ideal hexapole

$$E(r) = 3V_0 \frac{r^2}{r_0^3}. \tag{4.7}$$

Note that V_0 is the half of the voltage difference between two adjacent hexapole rods. Now the radial equation of motion can be derived:

$$\ddot{r} + \omega^2 r = 0, \tag{4.8}$$

with ω being the constant angular frequency

$$\omega = \sqrt{\frac{\mu}{m} \frac{M_J \Omega_{\text{eff}}}{J(J+1)} 6 \frac{V_0}{r_0^3}}, \tag{4.9}$$

and m the mass of the focused molecule. Knowing the differential equation for the radial motion, one can set up the matrix M_{Hex} describing the motion of the molecules in a harmonic potential [196]:

$$M_{Hex} = \begin{pmatrix} \cos \omega t_2 & \frac{1}{\omega} \sin \omega t_2 \\ -\omega \sin \omega t_2 & \cos \omega t_2 \end{pmatrix}. \tag{4.10}$$

Replacing t_2 with L_2/v_0 and inserting Equation 4.10 into 4.6 gives the full transformation matrix for the radial component:

$$\begin{pmatrix} r_f \\ v_{r_f} \end{pmatrix} = \begin{pmatrix} 1 & L_3/v_0 \\ 0 & 1 \end{pmatrix} \cdot \begin{pmatrix} \cos \omega L_2/v_0 & \frac{1}{\omega} \sin \omega L_2/v_0 \\ -\omega \sin \omega L_2/v_0 & \cos \omega L_2/v_0 \end{pmatrix} \cdot \begin{pmatrix} 1 & L_1/v_0 \\ 0 & 1 \end{pmatrix} \cdot \begin{pmatrix} r_i \\ v_{r_i} \end{pmatrix}. \tag{4.11}$$

When the nozzle is assumed as a point source a perfect focus is achieved and $r_i = r_f = 0$. With this the important equation given by Stolte [22] is derived for the relation between L_1, L_2, and L_3:

$$L_3 = \frac{L_1 + \frac{1}{\kappa} \tan(\kappa L_2)}{L_1 \kappa \tan(\kappa L_2) - 1}, \tag{4.12}$$

with

$$\kappa = \frac{\omega}{v_0} = \sqrt{\frac{\mu}{m} \frac{M_J \Omega_{\text{eff}}}{J(J+1)} 6 \frac{V_0}{r_0^3 v_0^2}}. \tag{4.13}$$

Equation 4.12 is an idealized description of a hexapole. The nozzle is never a point source, but molecules will be produced with a position and velocity spread, hence the focus blurs along the beam path. Another assumption, which is made in Equation 4.12, is the neglect of the Λ-doublet splitting. Close to the beam axis, where the hexapole fields are small, the Λ-doublet splitting can not be neglected, like it is done for the high field limit, in Equation 4.3. Crompvoets has mentioned the problem before [196]. Figure 4.2 (a), (b), and (c) show the focus of an ideal hexapole, one where the Λ-doublet splitting is not neglected and one in which also a longitudinal velocity spread of the molecular packet is taken into account, respectively. The focus is seen to blur, when the correct Λ-doublet splitting and especially when also a longitudinal velocity spread is assumed.

When the hexapole voltages are either increased, or the hexapole is turned on for longer than needed, to focus molecules at the originally desired focus, an effect called over-focusing is observed. This over-focusing effect is convenient to characterize and test a hexapole, see forthcoming Chapter 4.6.

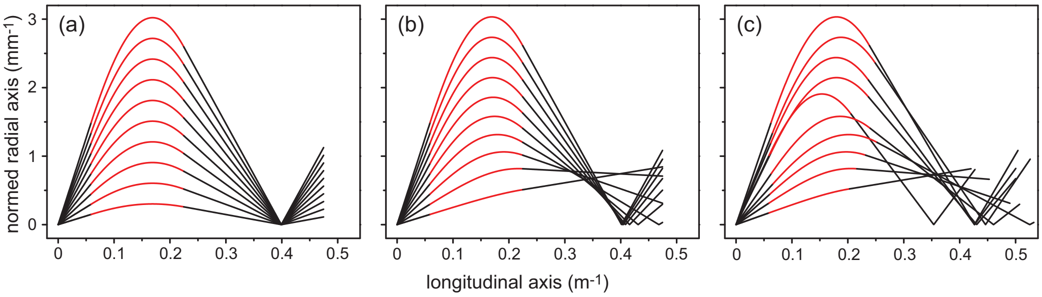

Figure 4.2: Calculated focusing curves of a hexapole for NO molecules in the $^2\Pi_{1/2}, J = 1/2, f$ state with a velocity of 280 m/s. The curves are colored black in the first and in the second region of free-flight and red in the focusing region, i.e. the hexapole is turned on/off when the curves change color. The molecules originate from a single point. Ten different radial velocities from 1 m/s to 5 m/s are simulated. In (a) a ideal hexapole is assumed with a linear force, where the Λ-doublet splitting is zero. A perfect focus is observed. In (b) the correct Λ-doublet splitting of the NO ground state of 0.0118 cm^{-1} is considered. A blurring of the focus is observed. In (c) a longitudinal velocity spread of 10% is considered, together with the Λ-doublet splitting. The focus blurs even stronger. Crompvoets has calculated similar images for ND_3 [196].

4.3 Hexapole state-selection

As it was mentioned in the introduction, a hexapole is not only well suited for focusing molecules, but also for the state-selection of a specific quantum state. High-field seeking molecules show a negative Stark shift, represented by the minus sign in Equation 4.2. The resulting defocusing force drives them away from the hexapole axis. Hence the amount of high-field seeking molecules is greatly decreased at the focus of the hexapole, see Figure 4.3.

In addition a hexapole can not only select low-field seeking molecules but also purifies the rotational state distribution. Since the force on each rotational level is different, the hexapole can be equipped with a combination of one or more beam-stops and diaphragms, creating a pathway which can only be followed by molecules in one specific rotational level. All other rotational levels are blocked by the beam-stop or diaphragm, see Figure 4.3. In most applications the selected state is the ground state, but in principle any rotational state could be selected with a sophisticated setup. Van Beek et al., for instance used two hexapoles with a diaphragm in between [46], selecting OH molecules in the $^2\Pi_{3/2}, J = 3/2, f$ state.

Last, the combination of beam-stop and diaphragm can also block the carrier gas. Especially in collision experiments the carrier gas is a serious problem, since the reagent beam will collide with carrier gas atoms and with the molecules seeded in the carrier gas. Thus a carrier gas free interaction region is required. With a beam-stop and a diaphragm a beam path is created, which allows no direct line-of-sight from the source to the detection. Thus the carrier gas atoms, which are

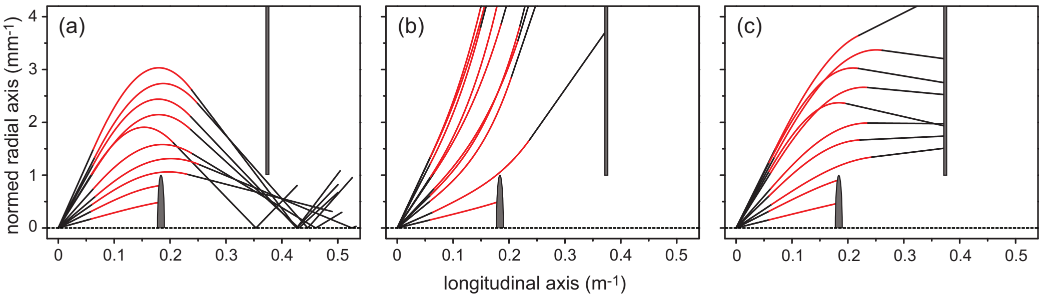

Figure 4.3: Calculated focusing curves of a hexapole for NO molecules in (a), the $^2\Pi_{1/2}, J = 1/2, f$ state, (b) the $^2\Pi_{1/2}, J = 1/2, e$ state, and (c) the $^2\Pi_{1/2}, J = 3/2, f$ state. In all calculations the molecules have a mean velocity of 280 m/s, the correct Λ-doublet splittings are considered and a longitudinal velocity spread of 10% is assumed. The molecules originate from a single point. Ten different radial velocities from 1 m/s to 5 m/s are simulated. The curves are colored black in the first and in the second region of free-flight and red in the focusing region, i.e. the hexapole is turned on/off when the curves change color. A beam-stop in the center and a diaphragm at the end of the hexapole are indicated by the shaded structures. In (a) many molecules pass the combination of beam-stop and diaphragm. In (b) the defocusing of high-field seekers is observed and in (c) the dilution of higher rotational levels by the combination of the beam-stop and the diaphragm is observed.

not influenced by the hexapole fields, hit either the beam-stop or the diaphragm on their direct path. Van Beek et al. followed this approach by putting a beam-stop in front of their first hexapole [46]. Their approach has one disadvantage. The beam-stop, being close to the source, blocks many molecules in the desired molecular state, since they have just left the nozzle and are therefore radially close to the beam axis. Instead the best position for a beam-stop is within the hexapole, where the radial component of all molecules is largest, but this approach is technically more challenging.

4.4 Hexapole construction

After this general description of hexapole focusing and state-selection the hexapole designed in this work is described. The hexapole is designed to select NO molecules in the $^2\Pi_{1/2}, J = 1/2, f$ state, with the shortest pathway as possible. Since it is designed for the OH-NO collision experiment the state-selection should be as perfect as possible and no carrier gas should enter the interaction region.

The low dipole moment of NO of only 0.159 Debye requires high electric fields. In "classic" hexapole designs the six rods are held by an insulating suspension. Although the rods are for the most part separated by vacuum, at least at one point they are connected via the suspension. In any high-voltage device a discharge can occur between electrodes with different voltage magnitudes or polarities. A dis-

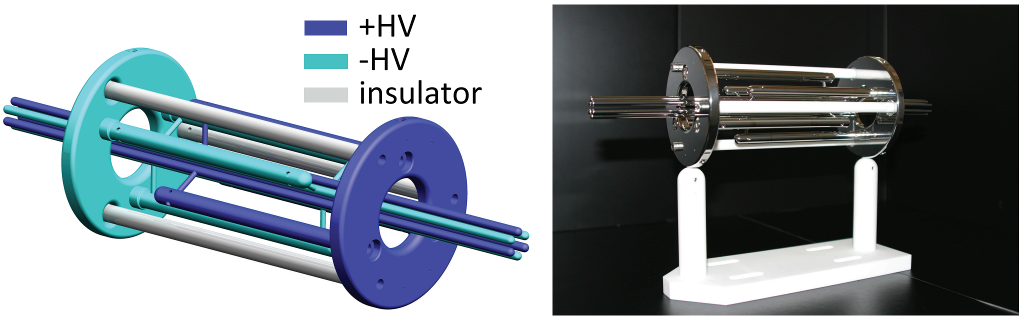

Figure 4.4: Left, schematic drawing of the hexapole and right a photograph. The suspensions for rods on different polarities are completely separated. Each suspension is holding only three rods of the same polarity, from the side of these rods. The rods and the two suspension are made from stainless steel. Suspensions and rods are on high voltage. In the left image the suspension and rods of the same polarity are indicated by the blue and cyan color and the suspension, which separates these two high voltage suspensions, is indicated with the gray color, respectively. The separating suspension is made from Macor, which is a machinable glass ceramic. In the right image the stainless steel parts and the Macor parts are recognized by their colors.

charge causes a voltage break down and leads therefore to unstable electric fields, making a proper functioning of the device impossible. Discharges might also lead to the worst-case for such a high-voltage device, which is the perforation of the electrode surface, increasing the possibility of more discharges. In the laboratory it has frequently been observed, that discharges in these "classic" hexapole designs mostly go over the suspension and not directly through the vacuum between adjacent rods. Hence by increasing the suspension distance the discharge possibility is reduced. In the "classic" hexapole design this is geometrically limited, because the six hexapole rods should also be as close to each other as possible to guarantee a small inner radius r_0 and hence a large focusing force. A convenient technical criterion to describe the high voltage abilities, is to estimate the maximum electric field strength in the high-voltage device. In a hexapole the maximum electric field strength is at the rod's surfaces.

The main innovative element of this new hexapole design, is to obtain a hexapole geometry without the need for ceramic suspensions that connect two neighboring hexapole rods. The suspensions in the new hexapole design are completely separated for rods on different polarities. Each suspension is holding only three rods of the same polarity, from the side of these rods, see Figure 4.4. The two suspension are also on high voltage, but are separated from each other by another insulating suspension. Therefore the pathway for a discharge over the insulating suspension is largely increased, while in the meantime the six hexapole rods are brought close to each other.

The hexapole is $l_{rod} = 30$ cm long and the rods have a radius of $r_{rod} = 2$ mm. The inner radius of the hexapole is $r_0 = 3.54$ mm, hence follows the relation from

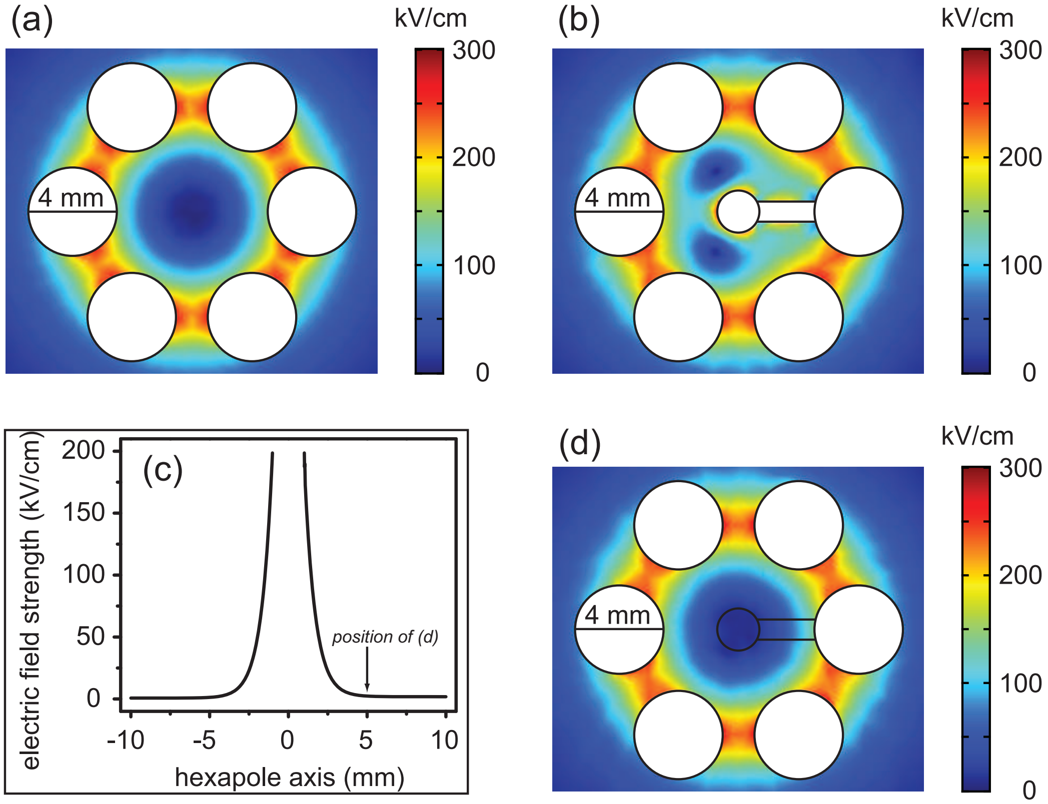

Figure 4.5: Electric field strength between the six hexapole rods. (a) shows a hexapole without the beam-stop. A homogeneous field distribution is seen. (b) is the distortion of the electric field strength at the center of the beam-stop. In (d) an image is seen, which shows that the distortion of the electric field strength at 5 mm distance from the center of the beam-stop can be neglected. (c) is the electric field strength along the center axis of the hexapole.

Anderson $r_{rod} = 0.565 \cdot r_0$, [192]. The smallest distance between adjacent rods is 1.54 mm. ±15 kV are applied to adjacent rods under normal operation, but it was tested that the hexapole can also be used up to ±18 kV. The maximum electric field strength in the hexapole is calculated with the COMSOL program [198], which uses the finite element method. At ±18 kV the maximum electric field strength is 260 kV/cm. Note that this is the maximum electric field strength at the rod's surfaces, not the electric field strength along the trajectory of the molecules. To my knowledge, this is the largest electric field strength, that has been reached in a hexapole so far. The voltages are switched by two commercial transistor based switches, which can be operated at a maximum voltage of 20 kV.

For the state-selection and carrier gas depletion a diaphragm with a diameter of 2 mm is mounted 20 mm behind the hexapole and a beam-stop with a diameter of 2 mm is mounted at the center, inside the hexapole. The beam-stop inside the hexapole is attached to one of the rods, i.e. the beam-stop is on high voltage. The electric field strength in the hexapole is calculated with the COMSOL pro-

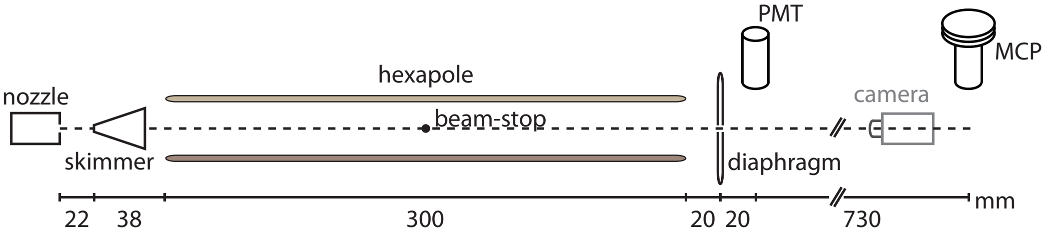

Figure 4.6: Scheme of the experimental setup. A pulsed beam of NO radicals is produced in a supersonic expansion. The NO radicals pass through a 30 cm long hexapole and are state-selectively detected via Laser Induced Fluorescence in the first detection region and via Resonance Enhanced Multi-Photon Ionization in the second detection region. The detection laser (not shown) is perpendicular to the molecular beam. A beam-stop is mounted in the center and a diaphragm at the end of the hexapole. The charge-coupled device camera which is used in a second experiment is also transparently displayed.

gram [198]. Figure 4.5 shows the result. It is seen from Figure 4.5 (c) and (d), that already at 5 mm distance from the center of the beam-stop the distortion of the electric field can be neglected. It is tested in the experiment, that the inhomogeneity in the electric field, created by the beam-stop, does not influence the trajectory of the molecules. Still, for a molecule with a large Stark shift, e.g. OH or ND_3, the inhomogeneity in the electric field close to the beam-stop can be a problem. This problem can always be circumvented by switching the hexapole off when the molecular packet is close tho the beam-stop. The hexapole acts then as two hexapoles aligned after each other.

4.5 Experiment

Figure 4.6 shows a scheme of the experimental setup. The molecular beam of NO radicals is produced in a supersonic expansion, by seeding 5% NO in Xe using a backing pressure of 2 bar. The nozzle is cooled to -70°C. The mean velocity v_0 of the Gaussian distribution of velocities of the NO molecules, is set between 280 m/s and 310 m/s, depending on the settings of the nozzle. The Gaussian shaped velocity spread is approximately 15%, full width at half max (FWHM). 22 mm from the nozzle the NO radicals pass through a 2 mm diameter skimmer. After the skimmer three experimental configurations are used, to characterize the hexapole.

In the first configuration the hexapole is not installed in the chamber and the NO molecules are detected at the first detection region after 37.8 cm of free flight, from the skimmer to the detection. In the second configuration, the hexapole is installed 38 mm behind the skimmer, and the molecules pass through the 30 cm long hexapole, while the beamstop and the diaphragm are not installed yet. The end of the hexapole is in 4 cm distance to the detection region. NO radicals that reside in the upper Λ-doublet component of the $J = 1/2$ rotational ground state are focused into the detection region, while molecules in the high-field-seeking lower Λ-doublet components are deflected from the beam axis. This configuration is used to analyze the functionality of the hexapole by measuring focusing and over-focusing effects. In the third configuration a 2 mm diameter beam-stop is installed in the center of the hexapole and a 2 mm diameter diaphragm is installed in the middle between the hexapole end and the first detection region, i.e. 2 cm downstream from the hexapole and 2 cm away from the first detection region. The skimmer, beam-stop, and diaphragm combination allows no direct line of sight from the source to the detection region, effectively filtering out the Xe atoms and higher rotational levels of the NO. In all experiments a voltage of ±15 kV is applied to the hexapole rods. Note that the first detection region is at the position, at which the NO beam is planned to intersect with the beam of a collision partner, thus the third experimental configuration is the same as for the planned experiment on the collision of OH-NO, reported in Chapter 5.

A pulsed dye laser, with a bandwidth 0.06 cm^{-1} is used to detect NO radicals in individual rotational levels by Laser Induced Fluorescence (LIF), using the $0-0$ band of the NO $A\,^2\Sigma^+ \leftarrow X\,^2\Pi$ transition around 226 nm. The fluorescence is mapped onto a PMT, which is mounted above the detection area. The laser wavelength is scanned around the $A\,^2\Sigma^+ \leftarrow X\,^2\Pi$ transition and individual rotational populations are estimated from the intensities in the spectra.

A second detection area is mounted 73 cm downstream from the first PMT. The pulsed dye laser is used to detect NO radicals by (1+1) Resonance Enhanced Multi-Photon Ionization (REMPI). The ions are focused by ion optics on a set of multi-channel plates (MCPs). The (1+1)REMPI detection is only used for the detection of NO molecules in the $X\,^2\Pi_{1/2}, J=1/2, f$ state. Since the distance between the two detection areas is well known, the velocity v_0 of the molecular packet is determined from time of flight measurements. The REMPI detector is also used for the small "on-the-side" experiment, described in Chapter 2.7, on the comparison of a (1+1)REMPI scheme and a (1+1')REMPI scheme for NO.

The experiment with the installed hexapole, beamstop and diaphragm, is repeated with and without the diaphragm, using a charge-coupled device camera. The camera is mounted behind the first detection area, replacing the second detection area, Figure 4.6. The camera is aligned with the molecular beam path. The fluorescence images of the NO molecules entering the first detection area, are recorded with the camera. The images are used to visualize the state-selectivity of the hexapole.

4.6 Results

Figure 4.7 shows measurements of NO molecules in the $X\,^2\Pi_{1/2}, J=1/2, f$ state in the first detection area (a) and second detection area (b), respectively. The measurement are performed in the second experimental configuration, where only the hexapole, but not the beam-stop and diaphragm are installed. In these measurements the time at which the hexapole is turned off is varied, while the time

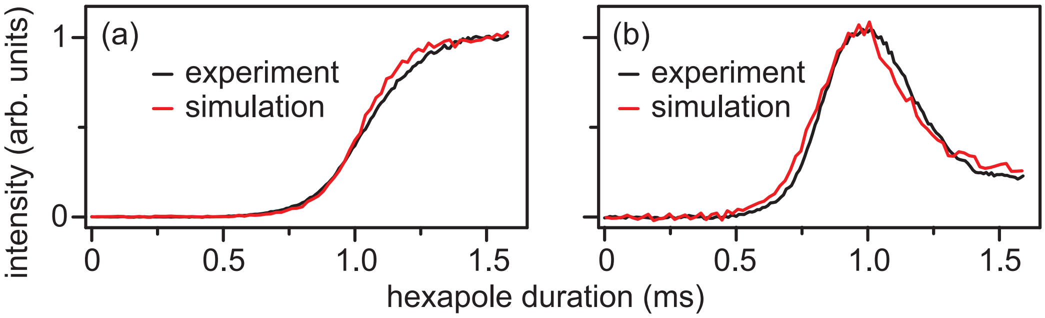

Figure 4.7: Variation of the duration of the applied hexapole fields. The black curves are NO molecules, which are detected in the $X\,^2\Pi_{1/2}, J = 1/2, f$ state in the first detection area (a) and second detection area (b), respectively. In (a) the molecules are detected constantly 1.59 ms after the nozzle is triggered, in (b) constantly at 4.03 ms. The red curve is the result of a Monte-Carlo trajectory simulation. The measurement and simulation in (a) reach a signal maximum shortly before the molecules are detected. In (b) a clear over-focusing is observed, when the duration is increased. A good overlap between simulation and measurement is seen.

the hexapole is turned on is kept constant. The hexaple is turned on at the same time as when the nozzle is triggered. Note, that the nozzle has an unknown response time on the order of hundreds of microseconds, thus the moment the nozzle opens is experimentally unknown. In (a) the molecules are detected constantly 1.59 ms after the nozzle is triggered, i.e. the hexapole is turned on. In (b) constantly at 4.03 ms. The duration of the applied hexapole fields is varied, while the time at which the molecules enter the hexapole field and the detection time is kept constant. Thus, increasing the duration time beyond the detection times of 1.59 ms in (a) and 4.03 ms in (b), does not change the signal, since the molecules are already detected.

In Figure 4.7 (a), a signal increase of focused molecules is observed over time. The signal reaches its maximum before the molecules are detected at 1.59 ms. The signal increase is approximately a factor 30. No over-focusing effect is observed in this measurement. Hence the hexapole length and voltages are just sufficient to focus NO molecules in the $X\,^2\Pi_{1/2}, J = 1/2, f$ state. In Figure 4.7 (b), an over-focusing effect is observed. Focusing molecules into the second detection area is already achieved when the hexapole is turned off 0.99 ms after the nozzle is triggered, since the second detection area is much further away along the beam path. This finding represents the relations for L_1, L_2, and L_3 in Equation 4.12.

Monte-Carlo trajectory simulation are performed to simulate the hexapole behavior. The simulation uses a molecular packet with a velocity of $v_0 = 299$ m/s, and a longitudinal (Δv_0) and transversal (Δv_r) Gaussian shaped velocity spread of 15% and 12% (FWHM), respectively. The initial Gaussian shaped spatial

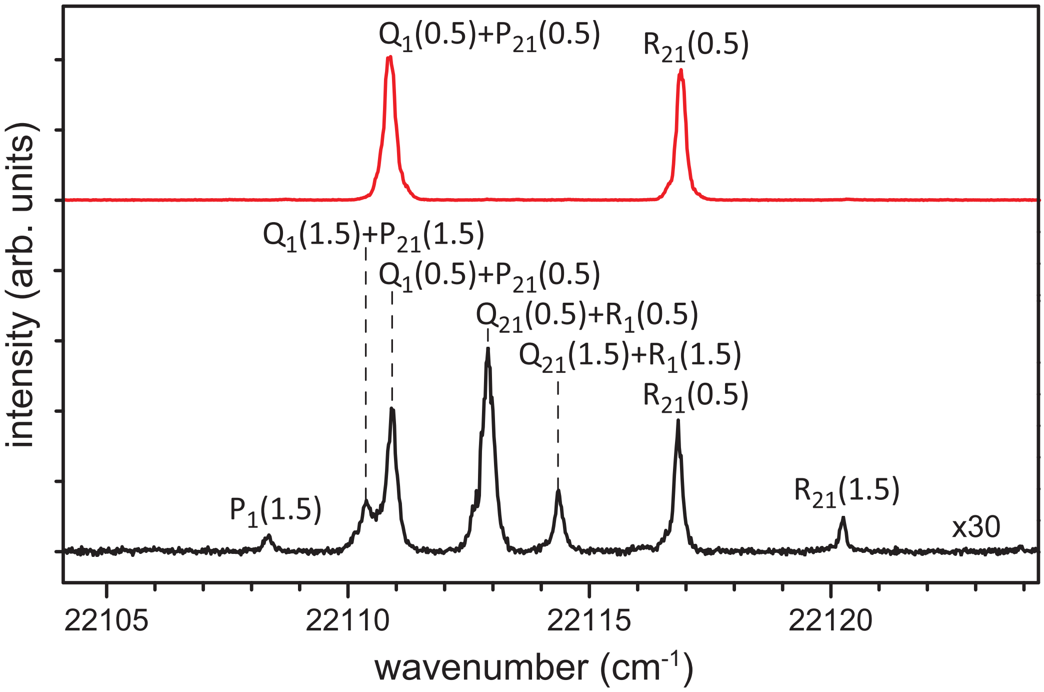

Figure 4.8: Wavelength scans over the $A\,^2\Sigma^+ \leftarrow X\,^2\Pi$ transition around 226 nm. The black spectrum is taken before the hexapole is installed in the chamber, the red spectrum when the hexapole, the beam-stop and the diaphragm are in use. The different rotational levels and their transitions are labeled in both spectra according the Equation 2.38. A clear state-selection of the $X\,^2\Pi_{1/2}, J = 1/2, f$ level is observed with a signal increase of approximately a factor 30.

state	without hexapole (%)	with hexapole (%)
$J = 1/2, f$	(36.2 ± 0.5)	(98.8 ± 0.2)
$J = 1/2, e$	(36.2 ± 0.5)	(0.3 ± 0.2)
$J = 3/2, f$	(12.4 ± 0.5)	(0.8 ± 0.2)
$J = 3/2, e$	(12.4 ± 0.5)	(0.1 ± 0.2)
$J = 5/2, f$	(1.4 ± 0.5)	(0)
$J = 5/2, e$	(1.4 ± 0.5)	(0)

Table 4.1: Rotational populations of the spectra shown in Figure 4.8. The populations are estimated with the LIFBASE program [134]. The second column represents the experiment without the hexapole, the third column the experiment in which the hexapole, the beam-stop and the diaphragm are in use.

spread Δx_i at the nozzle is assumed to be 27 mm (FWHM). With the relation

$$\Delta x_f = \sqrt{\Delta x_i^2 + (\Delta v_0 \cdot t)^2} \tag{4.14}$$

the final spatial spread in the first detection region can be estimated. The result is $\Delta x_f \approx$66 mm (FWHM). For both measurements, (a) and (b) a good overlap between these simulations and the measurement is seen.

In Figure 4.8 two wavelength scans over the $A\,^2\Sigma^+ \leftarrow X\,^2\Pi$ transition around 226 nm are seen. The black spectrum is taken before the hexapole is installed in the chamber, the red spectrum when the hexapole, the beam-stop and the diaphragm are in use, with the hexapole turned on from the triggering of the nozzle until the molecules are detected. The different rotational levels and their transitions are labeled in both spectra according the Equation 2.38. Without the hexapole (black spectrum) the rotational levels $(J = 1/2, e/f)$ and $(J = 3/2, e/f)$ are clearly visible, while in the red spectrum only the $(J = 1/2, f)$ state can be identified. Other molecular states are not seen on this scale in both spectra. The rotational populations for both spectra are fitted using the LIFBASE program [134], assuming equal populations in the two Λ-doublet components when the hexapole is not used. The results are shown in Table 4.1. A clear selection of the $X\,^2\Pi_{1/2}, J = 1/2, f$ state is observed, with a signal increase of approximately a factor 30.

In another experiment the REMPI detector is replaced by the charge-coupled device camera. The fluorescence images recorded by the camera are shown in Figure 4.9. The camera is in line with the beam axis, i.e. the center of the image is in line with the nozzle, the center of the hexapole, the beam-stop, the center of the diaphragm and the center of the detection region. In the images (a) to (d) the hexapole, beam-stop and diaphragm are in use. In the images (e) to (h) the diaphragm is removed, to visualize the importance of the combination of beam-stop and diaphragm. In images (a), (d), (e) and (h) the $(J = 1/2, f)$ level is detected in the images (b) and (f) the $(J = 1/2, e)$ level, and in the images (c) and (g) the $(J = 3/2, f)$ level. Only in the images (d) and (h) the hexapole is turned off, while in all other images it is used with ±15 kV applied to the rods and turned on from the opening off the nozzle until the molecules are detected.

A clear focus is observed in the images (a) and (e). The defocusing of high-field seeking molecules is observed in image (b) and (f). The combination of the beam-stop and the diaphragm eliminates any detection of $(J = 1/2, e)$ molecules, image (b), while in (f) the defocused $(J = 1/2, e)$ molecules appear at the side of the images. These molecules left the hexapole between the rods. In image (c) and (g) the focused $(J = 3/2, f)$ molecules appear. No clear focus is observed since the force on the $(J = 3/2, f)$ is too weak. The comparison between image (c) and (g) illustrates the importance of the diaphragm for the state-selection. Without diaphragm a large amount of $(J = 3/2, f)$ is still entering the detection region. Image (d) and (h) are taken to illustrate the behaviour of the carrier gas. The hexapole is turned off and the $(J = 1/2, f)$ molecules move undisturbed in a straight path from the nozzle to the detection, i.e. they behave just like the

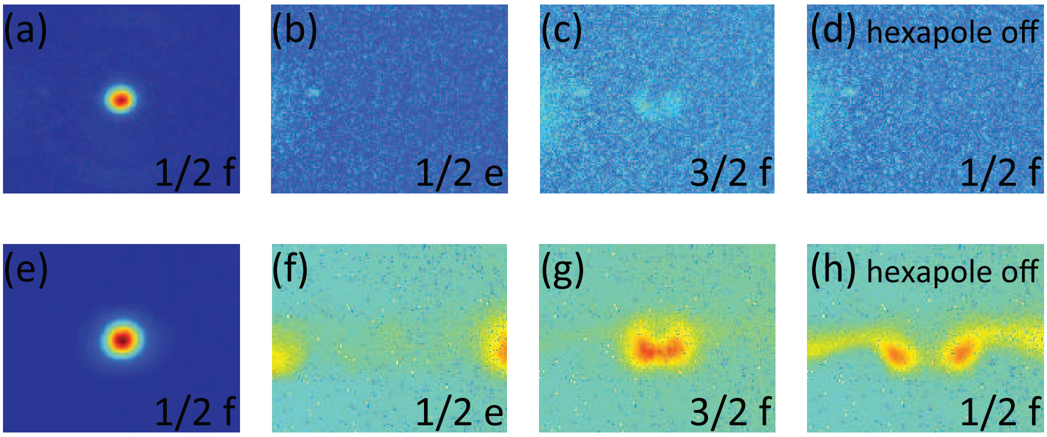

Figure 4.9: Fluorescence images recorded with the charge-coupled device camera. The camera is in line with the beam axis, i.e. the center of the image is in line with the nozzle, the center of the hexapole, the beam-stop, the center of the diaphragm and the center of the detection region. In the images (a) to (d) the hexapole, beam-stop and diaphragm are in use. In the images (e) to (h) the diaphragm is removed to visualize the importance of the combination of beam-stop and diaphragm. The detected molecular state is indicated in each image. The hexapole is turned off in image (d) and (h). The comparison of the images visualizes the state-selectivity and the dilution of the carrier gas, see main text.

carrier gas. Image (h) illustrates how much carrier gas is blocked by the beam-stop, since no molecules appear at the center of the image, which is in line with the beam-stop. The streak of molecules in the center of the image are molecules passing between the rods. When the diaphragm is in use, like in image (d), no molecules are detected, thus illustrating that all carrier gas is blocked.

4.7 Conclusion

In this Chapter a new design for a hexapole to focus NO molecules in the $X\,^2\Pi_{1/2}, J = 1/2, f$ level is introduced. The new hexapole design allows high electric fields under very small rod distances, without the problem of voltage break down due to discharges between the rods. With this new design it is possible to focus NO molecules, despite the small dipole moment, with an only 30 cm long hexapole. With a velocity $v_0 = 299$ m/s and a longitudinal velocity spread of $\Delta v_0 = 15\%$ the molecules have a spatial spread of only 66 mm in the region where the NO beam is planned to intersect with the beam of a collision partner. Thus, the goal of this hexapole design, to keep the number density of molecules in the interaction region per time as large as possible is achieved.

The state-selective abilities of the hexapole are proven in a determination of the residual population behind the hexapole, beamstop and diaphragm combination. The $X\,^2\Pi_{1/2}, J = 1/2, f$ is populated with $\approx$99%. The camera images illustrate the state-selective abilities of the hexapole and the filtering of the carrier gas. The depletion of the Xe carrier gas is not directly measurable in the current experimental setup.

Because of the described abilities, this hexapole is well suited for the planned experiment on the collision of OH-NO, as well as for a variety of other gas-phase and surface scattering experiments, in which a high intensity packer of extremely state-pure NO is desired, separated from the carrier gas that is needed to produce the beam.

Chapter 5

Bi-molecular scattering of OH with NO radicals

In this Chapter the first study of rotational energy transfer between two molecular species with full state-selection prior to the collision and quantum state resolution in the detection process is discussed. A beam of Stark-decelerated OH ($X\,^2\Pi_{3/2}, J = 3/2, f$) radicals is scattered with a beam of hexapole state-selected NO ($X\,^2\Pi_{1/2}, J = 1/2, f$) radicals in a crossed beam configuration. The state-to-state inelastic scattering cross sections are measured for collision energies between 70 and 300 cm^{-1}, revealing the quantum state-resolved threshold behavior of four scattering channels. Absolute cross sections are experimentally determined and show fair agreement with the outcome of theoretical calculations with full Λ-doublet resolution for both radical species.

Based on:
Quantum-state resolved bi-molecular collisions of velocity-controlled OH with NO radicals,
M. Kirste, X. Wang, H. C. Schewe, G. Meijer, K. Liu, A. van der Avoird, L. M. C. Janssen, K. B. Gubbels, G. C. Groenenboom, and S. Y. T. van de Meerakker, Science **338**, 1060, 2012.

5.1 Introduction

A detailed understanding of the flow of energy that occurs during molecular collisions is of fundamental importance to many areas of physics and chemistry [126]. Rotationally inelastic scattering is one of the key processes underlying the exchange of energy between molecules [39]. In bulk systems, rotational energy transfer is responsible for the thermalization of state populations following a chemical reaction. In the dilute interstellar medium, inelastic collisions contribute to the formation of non-thermal population distributions that result in, for instance, interstellar masers [199]. Accurate state-to-state inelastic scattering cross sections are essential ingredients for reliable models of chemical processes in combustion physics, atmospheric science, and astrochemistry.

In molecular beam collision experiments, numerous methods have been developed to vary the collision energy and to prepare molecules in a single rotational (sub)level prior to the collision using electric, magnetic, or optical fields [39]. Thus far these methods have mostly been used to study collisions of state-selected molecules with rare gas atoms. Also in this thesis a collision experiment of state-selected OH $(X\,^2\Pi_{3/2}, J = 3/2, f)$ radicals with He atoms and D_2 molecules is reported in Chapter 3. After the successful accomplishment of that experiment a new experiment on bi-molecular scattering was planned. The ultimate goal of my work was to conduct an experiment on quantum state resolved bi-molecular collisions of two molecules. Molecule-molecule interactions are of particular fascination, since they are a feature element of most chemical processes. Needless to say, that many chemical reactions need two molecules.

The study of molecule-molecule collisions at the ultimate quantum level has been a quest in molecular collision physics since it was established in the 1950s [87]. Opposed to an atomic target, a molecular scattering partner possesses internal degrees of freedom of its own. A full characterization of bi-molecular collisions offers unique prospects to bring a quantitative description of molecular reaction dynamics from the relatively well understood atom-molecule interactions into the realm of more complex and chemically relevant systems.

Major obstacles exist that have prevented studies of state-to-state bi-molecular scattering [86]. The main challenge is the need for reagent beams with sufficient quantum state purity at the densities necessary to observe population transfer in one, or both, reagent beam(s). Thus far, experiments of this kind have only been possible using cryogenically cooled H_2 molecules as a target beam [43, 88].

Also the theoretical study of molecule-molecule collisions has been very challenging. Whereas atom-molecule scattering cross sections can now be calculated routinely in excellent agreement with experiment [84, 89], much less is known about rotational energy transfer in molecule-molecule collisions [90]. As opposed to an atomic target, a molecular scattering partner possesses internal degrees of freedom of its own, adding a level of complexity that can easily render ab initio quantum scattering calculations extremely challenging, if not impossible. Experimental data on bi-molecular state-to-state cross sections is generally lacking, and kinetic models often use collision rate coefficients that are expected to be inaccurate [91].

For the bi-molecular collisions experiment a new hexapole was designed, which was described in Chapter 4. This hexapole is used to state-select a beam of NO radicals ($X\,^2\Pi_{1/2}, v = 0, J = 1/2, f$). The NO is scattered with a beam of Stark-decelerated OH ($X\,^2\Pi_{3/2}, v = 0, J = 3/2, f$) radicals. The OH-NO system is chosen, because both open shell radical species are benchmark systems for the scattering of state-selected molecules with rare gas (Rg) atoms [38]. OH-Rg and NO-Rg collisions involve two Born-Oppenheimer potential energy surfaces (PESs) with non-adiabatic couplings between them. Collisions between OH and NO involve eight interacting PESs, representing the full complexity of bi-molecular inelastic collisions [200]. The OH-NO system serves also as a prototypical example for radical-radical reactions, that are of fundamental importance in gas-phase chemical kinetics [201].

In addition to the scientific relevance of the OH-NO system, both radicals are well suited for the manipulation with electric fields, see Chapter 2.5. OH has been among the first molecules to be decelerated in a Stark decelerator [202] and NO radicals are routinely focused in hexapole devices [39]. In addition, both molecules, especially the NO radical, can be produced with large number densities making a molecule-molecule collision feasible.

5.2 Experimental setup

The experiments are performed in a crossed molecular beam machine, which is schematically shown in Figure 5.1. The beam of OH radicals is produced via photodissociation of HNO_3 seeded in Ar or Kr. The supersonic expansion is done with a backing pressure of 1.6 bar. The OH radicals pass through the 2.6 m long Stark decelerator, which was described briefly in Chapter 3 and in detail in [125]. In addition to the apparatus described in these two sources a cylindrically formed stainless steel separation wall is mounted between the end of the decelerator and the crossing point of the two molecular beams. It is 24 mm from the end of the decelerator and 38 mm from the interaction region. Note that this separator is not shown in the scheme of the experimental setup in Figure 5.1. On the beam axis of the separator is a 4 mm diameter hole. The decelerated OH packages can pass through this hole. The separation wall acts as a differential pumping stage, which separates the vacuum chamber of the decelerator from the vacuum chamber where the collisions take place. It also acts as a electrical shielding, which guarantees field free collisions.

The Stark decelerator selectively manipulates OH molecules in the $X\,^2\Pi_{3/2}$, $J = 3/2, f$ low-field seeking state. All high-field states are effectively defocused and higher rotational states are diluted during the 2.7 meter flight path from the source to the interaction region. The defocused and diluted OH molecules and the carrier gas atoms are shielded from the collision area by the separation wall. The state purity of the OH radicals is $\geq$99.5% in the $X\,^2\Pi_{3/2}$, $J = 3/2, f$

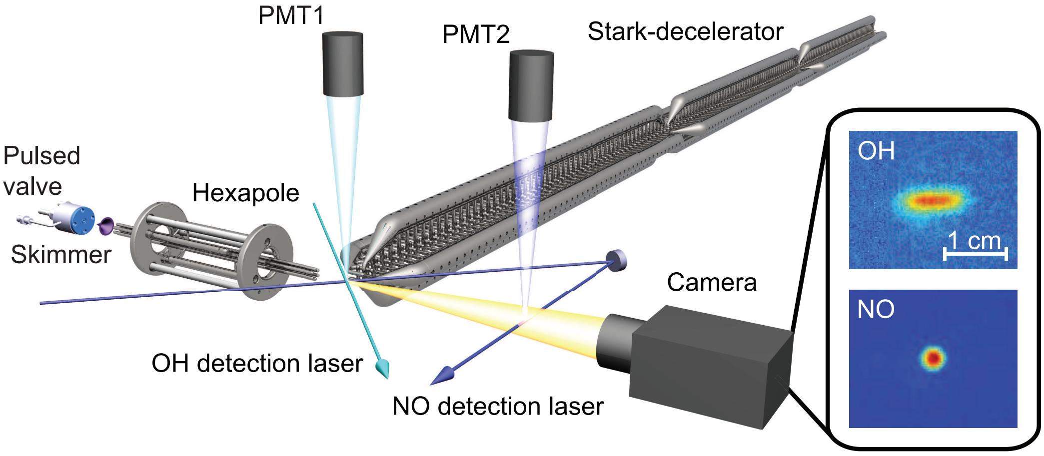

Figure 5.1: Schematic representation of the experimental setup. A state-selected and velocity tunable beam of OH radicals is produced using a 2.6-meter long Stark decelerator, and crossed with a hexapole state-selected beam of NO radicals. Both radical species are detected state-selectively using Laser Induced Fluorescence (LIF). The total fluorescence intensity is measured using a photomultiplier tube (PMT), and the spatial distribution of both reagent molecular packets is recorded by imaging the fluorescence onto a charge-coupled device camera. Typical images of the OH and NO packets are shown in the upper and lower insets, respectively. The mean speed of the OH radical packet is precisely known from the settings of the Stark decelerator. The collision energy is calibrated from the NO beam speed that is measured via a second LIF detection zone located 30 cm downstream from the collision area.

state, with the residual population being in the upper Λ-doublet components of higher rotational states, e.g. $(J = 5/2, f)$, $(J = 7/2, f)$, ... The velocity of the OH radicals is tuned between 240 m/s and 507 m/s for Kr and between 460 m/s and 750 m/s for Ar using the Stark decelerator. The velocity distribution at the exit of the decelerator ranges between 16 and 27 m/s (FWHM). Note that the rotational levels of the two spin orbit manifolds of the OH electronic ground-state will hereafter be designated with the labels $F_1, J, e/f$ and $F_2, J, e/f$, instead of the full labels $X\,^2\Pi_{3/2}, J, e/f$ and $X\,^2\Pi_{1/2}, J, e/f$, respectively. For further reading see Chapter 2.

The molecular beam of NO radicals is produced in a supersonic expansion by seeding 20% NO in Xe using a backing pressure of 0.3 bar. The NO radicals pass through a 30 cm long hexapole, which is described in Chapter 4. NO radicals that reside in the upper Λ-doublet component of the $J = 1/2$ rotational ground state are focused into the collision region, while molecules in the high-field-seeking lower Λ-doublet components are deflected from the beam axis. A 2 mm diameter beamstop is installed in the center of the hexapole. A diaphragm is installed 10 mm downstream from the hexapole and 30 mm away from the crossing point. The skimmer, beamstop, and diaphragm combination allows no direct line of sight from the source to the collision region, effectively filtering out the Xe atoms from the molecular beam pulse. The beamstop-diaphragm combination offers the additional advantage to greatly improve the state purity of the NO radical beam, see Chapter 4. Only NO radicals in the $X\,^2\Pi_{1/2}$, $J = 1/2, f$ state can effectively pass through the hexapole, resulting in a state purity of $\geq$99.0%. The NO package has a velocity of 310 m/s and a velocity distribution of 52 m/s (FWHM). In addition to its state-filtering abilities, the diaphragm also acts as an electrical shielding, which guarantees field free collisions.

The collision energy and energy distributions are calculated from Equation 2.78 and Equation 3.1. With the velocities and velocity distributions described above and the mass of OH of 17 a.u. and the mass of NO of 30 a.u. the collision energy ranges from 70 cm^{-1} to 300 cm^{-1} and the collision energy distribution amounts to 20 cm^{-1} (FWHM).

The collision induced population in four different rotational levels, $(F_1, J = 3/2, e)$, $(F_1, J = 5/2, e)$, $(F_1, J = 7/2, e)$ and $(F_2, J = 1/2, e)$ of the OH radical are measured at the time when both beams maximally overlapped in the beam crossing area. Depending on the inelastic channel, only a fraction of $10^{-4} - 10^{-6}$ of the OH radicals are inelastically scattered. Only final states of e symmetry are probed, as the Stark decelerator efficiently eliminated any initial population in these states. The collision induced populations of the NO radical are not measured, since the scattering signals in the rotational excited levels of the NO radical are below the detection limit of the current experimental setup.

Three pulsed dye lasers are used to detect the parent radical beams and the scattered OH radicals by Laser Induced Fluorescence (LIF). The fluorescence is mapped onto the first PMT mounted above the collision area. The first dye laser (bandwidth 0.06 cm^{-1}) was used to detect NO radicals via saturated laser-induced fluorescence using the $0 - 0$ band of the NO $A\,^2\Sigma^+ \leftarrow X\,^2\Pi$ transition around 226 nm. The reagent beam of OH $(F_1, J = 3/2, f)$ radicals, as well as the OH radicals that inelastically scattered into the $(F_1, J = 5/2, e)$, $(F_1, J = 7/2, e)$ and $(F_2, J = 1/2, e)$ levels, are detected via saturated laser-induced fluorescence using the $1 - 0$ band of the OH $A\,^2\Sigma^+ \leftarrow X\,^2\Pi$ transition around 282 nm, employing a second pulsed dye laser (bandwidth 0.06 cm^{-1}). Although the bandwidth of this laser is larger than the Λ-doublet splittings in the corresponding rotational levels, the selective detection of population in a single Λ-doublet level is facilitated by the parity selection rules of the electric dipole allowed (EDA) transitions, Equation 2.30 to 2.36, and the large energy splitting between levels of opposite parity in the $A\,^2\Sigma^+$ state.

Population transfer into the $F_1, J = 3/2, e$ level can not be probed with a conventional pulsed dye laser, as such laser would simultaneously induce the magnetic dipole allowed (MDA) transition that probes the population in the initial $F_1, J = 3/2, f$ level (see Figure 5.2). This problem only exists for the $F_1, J = 3/2$ level, not for the $(F_1, J = 5/2)$, $(F_1, J = 7/2)$ and $(F_2, J = 1/2, f)$ level, because of the large population difference of 3-4 orders of magnitude of reagent OH radicals and product OH radicals in the two Λ-doublet components

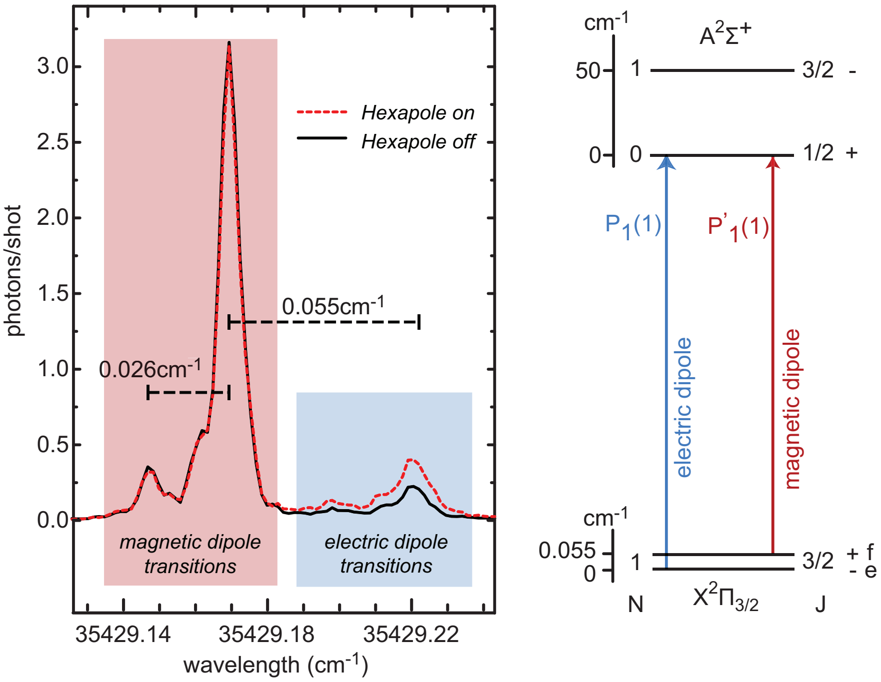

Figure 5.2: Magnetic dipole allowed (MDA) $P_1(1)$' transition that probes the population in the initial $F_1, J = 3/2, f$ level and the electric dipole allowed (EDA) $P_1(1)$ transition that probes the population in the $F_1, J = 3/2, e$ level. Two spectra are shown that are taken with the hexapole switched on (red curve) and off (black curve). The MDA and EDA transitions are separated by the Λ-doublet splitting of the ground state of 0.055 cm^{-1} and each transition splits due to the hyperfine structure of the $J = 1/2$ level in the excited $A\,^2\Sigma^+$ into two lines separated by 0.026 cm^{-1}.

of the same rotational level. The EDA and MDA transitions are spectroscopically separated using a third pulsed dye laser system with a superior bandwidth of approximately 150 MHz. In this laser the output of a frequency stabilized single mode ring dye laser is amplified in a three stage pulsed dye amplifier pumped by a frequency-doubled injection seeded Nd:YAG pump laser. Care is taken to probe the OH populations with this narrowband laser system under unsaturated conditions. In Chapter 6 an experiment is reported, in which the ratio of the EDA and MDA transitions is measured and compared to a theoretical evaluation.

In Figure 5.2, two spectra containing the EDA and MDA transitions are shown that are recorded when the high voltage on the hexapole to manipulate the NO radical beam is switched on and off, respectively. The left two peaks correspond to the MDA transition, that are split by the hyperfine structure in the $A\,^2\Sigma^+$ state, and are seen to be unaffected by the presence of the NO radical beam. The broader feature on the right corresponds to the EDA transition, that is clearly affected by the NO radical beam. The collision induced population in the $F_1, J = 3/2, e$ level is inferred from the integrated intensity difference of all lines in both spectra. The minor initial population in the $F_1, J = 3/2, e$ level that can be seen in Figure 5.2 is due to inelastic scattering of OH $F_1, J = 3/2, f$ radicals with particles in the background gas of the vacuum chamber during the approximately 60 mm flight distance between the exit of the Stark decelerator and the center of the collision area.

The two dye lasers used for the OH detection are parallel to each other and bisect the beam axes of the hexapole and Stark decelerator. The third laser, for the NO detection, shoots under an angle of 90° in respect to the other two lasers through the collision area and is reflected back into the chamber 30 cm downstream the NO beam-path. At this second intersection of this laser with the NO beam a second PMT is mounted above (see Figure 5.1). The collision energy is calibrated from the NO beam speed that is measured between the two LIF zones.

All lasers have a beam diameter of 8 mm, and care is taken to shape the laser beams to produce a homogeneous intensity distribution. This is carefully verified by recording the fluorescence images with a charge-coupled device camera. Typical images of the OH and NO packets are shown in Figure 5.1. The spatial overlap of the two beams is checked each day for each collision energy.

The experiment runs at a repetition rate of 10 Hz, and all trigger signals to synchronize the experiment are computer controlled. The voltages on the hexapole to manipulate the NO radical beam are applied only every other shot, and the collision signals are inferred from the signal intensity difference of alternating shots of the experiment. Hence for very small collision energies unphysical negative cross sections can sometimes result. To reduce the influence of long term drifts in the experiment, the collision energy is varied in a quasi-continuous cycle. The Stark decelerator is programmed to produce a different velocity of the OH radicals every second shot of the experiment. The trigger pulses that control the NO radical beam, the hexapole, and the detection laser(s) are adjusted automatically to match the arrival time of the OH packet in the collision zone. A single cycle consists of 12 measurements using 6 different velocities of the OH packet. In the first 6 measurements, the velocity of the OH packet is varied from high to low values. In the next 6 measurements, the OH velocity is varied from low to high velocities.

The collision induced population in the $(F_1, J = 5/2, e)$, $(F_1, J = 7/2, e)$, and $(F_2, J = 1/2, e)$ levels is probed by repeating these cycles 1500 times with a fixed wavelength for the pulsed dye laser. The resulting 3000 averages are taken over a period of 10-30 days resulting in 96000 to 138000 total averages. When the $(F_1, J = 3/2, e)$ level is probed, the frequency of the narrowband pulsed dye laser is scanned over an energy interval of 0.12 cm^{-1} to cover the magnetic and electric dipole transitions. At each wavelength position, the cycle of 12 measurements is repeated 15 times, before a new wavelength position is chosen. These wavelengths scans are repeated 75 to 78 times over a period of 20 to 30 days.

The fluorescence signals are recorded using dedicated data acquisition software, and are analyzed using photon counting techniques. The signal level of the parent OH packet corresponds to approximately 3000 photons per shot. The signal levels of the scattering products ranges from 0.2 photons per shot (for the $F_1, J = 3/2, e$ channel) to < 0.01 photons per shot for the weakest channels. The observation of these weak signals is facilitated by the excellent state purity of the Stark-decelerated beam of OH, and careful control over the stray light from the lasers.

The measured scattering signals are the arithmetic mean of all repetitions of the experiment. The error is estimated from the standard error of the mean: $u = \frac{s}{\sqrt{n}}$, with s being the standard deviation and n the number of observations. Note that u is also referred to as uncertainty.

The scattering signals of the four rotational levels, $(F_1, J = 3/2, e)$, $(F_1, J = 5/2, e)$, $(F_1, J = 7/2, e)$ and $(F_2, J = 1/2, e)$ are transformed into excitation functions, with the help of the methods described in the forthcoming Chapter 5.3. Chapter 5.3 also describes how these excitation functions are put to an absolute scale. Absolute cross sections are obtained and are compared to the outcome of theoretical calculations described in Chapter 5.5.

5.3 Data analysis

5.3.1 The density-to-flux transformation

In crossed beam scattering experiments using pulsed molecular beams, the measured scattering signals do not directly relate to cross sections. The observed scattering signal is the result of collisions between particles in two beams, each with an inhomogeneous density profile, that experience a time-dependent overlap. Generally, a so-called number density-to-flux transformation needs to be performed that requires information on the spatial and temporal distributions of the overlapping beams, the details of the detection system, and the differential cross section of the scattering process [148, 203]. This procedure is known to be elaborate and prone to error. With the experimental techniques employed here, packets of OH radicals and NO radicals collide that have a well defined and measurable density, velocity, and size. In particular the Stark-decelerated packet of OH radicals is a well defined packet with a narrow spatial distribution, greatly simplifying the analysis. The implications of this for the data analysis in crossed beam experiments is discussed below.

In a crossed beam experiment with laser-induced fluorescence detection, the scattering signal $S_J(T)$ that is recorded at time T relates directly to the number of particles N_J that have been scattered into quantum state J:

$$S_J(T) \propto P_J(T)\, N_J(T), \tag{5.1}$$

where the factor $P_J(T)$ represents the probability for the scattered particles to be detected at time T, i.e., the probability that the scattered particles are within the probe laser volume V_{probe} at time T. The number of scattered particles follows from the beam geometries and the scattering cross section:

$$N_J(T) = \int\int n_{OH}(\vec{r}, t)\, n_{NO}(\vec{r}, t)\, \sigma_J\, g\, dV_{int}\, dt, \tag{5.2}$$

where $n_{OH}(\vec{r},t)$ and $n_{NO}(\vec{r},t)$ are the density distributions of the parent OH and NO radical beams, respectively, σ_J is the scattering cross section to populate state J, and g is the magnitude of the relative velocity vector of the colliding particles, see Chapter 2.6. Both reagent packets of molecules are assumed to have no velocity spread, such that for a given collision energy E_c, there is a single value of g that describes the relative velocity of the colliding beams. The integral must be performed over the beam intersection volume V_{int}, and over all times t until the probe laser fires.

In general, the evaluation of the detection probability $P_J(T)$ requires knowledge over the post-collision velocity vector of the scattered particles, and hence information on the differential cross section. Below, it will be shown that for the present experimental conditions, the detection probability $P_J(T)$ is unity for all collision energies, and for all final states J that are probed, greatly simplifying the analysis.

In its propagation direction, the Stark-decelerated packet of OH radicals is small compared to the NO radical beam, and the temporal overlap between the two beams is exclusively defined by the Stark-decelerated OH radicals. This is illustrated in Figure 5.3, in which the measured normalized arrival time distributions of the NO and OH radical packets are shown. The distribution for the OH radical pertains to the situation where the Stark decelerator is programmed to produce a packet of OH radicals with a mean velocity of 625 m/s ($E = 220$ cm^{-1}). In this case, a packet of OH radicals is created with the largest possible extent in the propagation direction. Even in this case, the arrival time distribution of the OH radicals has a width (FWHM) of only 25 μs. It is seen that the intensity of the NO radical beam is approximately constant during the overlap with the packet of OH radicals.

Therefore no temporal dependence, and no change of the spatial distribution along the propagation direction is assumed to model the density distribution of the NO radical beam. A right-handed coordinate system is defined, with its origin at the crossing point of the centerlines of both molecular beams. The x-axis and the y-axis are defined as the OH and NO propagation directions, respectively. I.e. the decelerator is at a negative x position and the hexapole at a negative y position. The first PMT is at a positive z position, see Figure 5.1.

In the radial direction, the density distribution are best described by Gaussian profiles:

$$n_{NO}(\vec{r},t) = n_{NO}(\vec{r}) = n^{NO}_{max}\, e^{-\alpha(x^2+z^2)}, \tag{5.3}$$

where n^{NO}_{max} represents the maximum density of the NO radical beam. The parameter $\alpha = 4\log 2/(d_{NO})^2$ is estimated from numerical trajectory simulations of the NO radical beam that propagates through the electrostatic hexapole, and from the measured two-dimensional images of the NO beam, see Chapter 4. The NO beam is best characterized using $d_{NO} = 1.177$ mm (FWHM).

The packet of OH radicals travels along the x-axis with a velocity v_{OH}. The spatial distribution of the packet of OH radicals is accurately known from numerical trajectory simulations of the deceleration process [76]. These simulations are

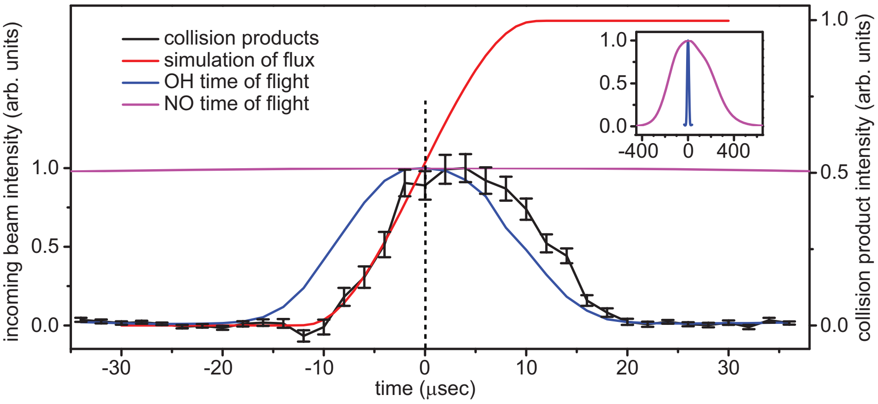

Figure 5.3: Comparison of the temporal dependence of the scattering signal $S_J(T)$ (black), of the integral in equation 5.1 (red), the OH radical beam (blue) and the NO radical beam (violet). The y-axis on the left side relates the two radical beams, and the y-axis on the right side relates to the scattering signal and the simulation. All curves are scaled to one to facilitate a comparison of the temporal profiles. The inset shows an enlarged time range to visualize the broad temporal distribution of the NO radical in relation to the temporal width of the OH radical beam. Note that the temporal distribution of the scattering signal is shifted to later times with respect to the arrival time distribution of the reagent packet of OH radicals. This is the result of the difference between the beam intersection volume V_{int} and the probe laser volume V_{probe}, with $V_{probe} > V_{int}$. The vertical dashed line, at $T = 0$, corresponds to the time at which the laser is fired when cross sections are measured.

Monte Carlo trajectory simulation, that start with a Gaussian 6D phase space distribution. The equations of motions are calculated from the known Stark energy of the OH molecules. The simulation is performed with finite time steps and the equations of motions are approximated with Runge-Kutta methods. In the transverse direction, the spatial distribution can be accurately described by a Gaussian distribution. In the propagation direction, however, the distribution is best described by a parabolic distribution:

$$n_{OH}(\vec{r}, t) = n_{max}^{OH}(1 - b(x - v_{OH}t)^2)\, e^{-\beta(y^2+z^2)}, \tag{5.4}$$

where n_{max}^{OH} represents the maximum density of the OH radical beam. Outside of the intersection points $\pm\sqrt{\frac{1}{b}}$ with the x-axis this function is defined to be 0. The parameters n_{max}^{OH}, b, and $\beta = 4\log 2/(d_{OH})^2$ depend on the settings of the Stark decelerator, and are thus different for every value of v_{OH} that is produced, i.e. different for every phase angle ϕ. The parameters b and d_{OH} (FWHM) are fitted from the spatial distributions that result from the three dimensional Monte-Carlo trajectory simulations of the deceleration process, and are given in Table 5.1.

The integrals in equation 5.1 can now be evaluated. Assuming $P_J(T) = 1$, the temporal dependence of the scattering signal $S_J(T)$ as shown in Figure 5.3

Argon					
E$_c$ (cm^{-1})	v$_{OH}$ (m/s)	b (m^{-2})	d$_{OH}$ (mm)	S$_{OH}$ (a.u.)	n$^{OH}_{max}$ (a.u.)
300	752	70274	0.86	0.34	0.50
280	722	51289	0.85	0.51	0.67
260	691	35234	0.85	0.70	0.75
240	659	27800	0.82	0.88	0.91
220	625	20546	0.79	1.00	1.00
210	606	24421	0.82	0.96	0.94
200	588	27891	0.82	0.88	0.90
190	569	31090	0.86	0.75	0.74
180	549	36815	0.90	0.70	0.69
160	507	47079	0.90	0.52	0.58
140	461	75079	0.90	0.32	0.46

Krypton					
E$_c$ (cm^{-1})	v$_{OH}$ (m/s)	b (m^{-2})	d$_{OH}$ (mm)	S$_{OH}$ (a.u.)	n$^{OH}_{max}$ (a.u.)
160	507	21781	0.91	0.82	0.63
140	461	24952	0.84	0.73	0.69
130	437	28124	0.91	0.65	0.55
120	411	30058	0.99	0.53	0.39
110	383	34665	0.96	0.49	0.41
100	353	40351	1.13	0 39	0.25
90	320	44726	1.18	0.33	0.20
80	283	54451	1.26	0.24	0.15
70	242	55447	1.39	0.18	0.91

Table 5.1: Simulation parameters for all collision energies and the two carrier gases Argon and Krypton that are used to generate the OH molecular beam. Column one shows all collision energies that have been used to measure the collision signals and column two shows the corresponding velocities of the OH beam produced by the Stark decelerator. b and d_{OH} are estimated from numerical trajectory simulation of the decelerator. S_{OH} is the measured peak signal intensity of the reagent packets of OH radicals as shown in Figure 5.4. The maximum density n^{OH}_{max} can be estimated via align 5.4 from b, d and S_{OH}.

is obtained for a collision energy of 220 cm^{-1} (v_{OH} = 625 m/s). This curve is calculated for the $F_1, J = 3/2, e$ scattering channel, i.e., for the situation in which the scattered OH radicals have the largest recoil velocity vector. The temporal dependence of the experimentally observed scattering signal is shown superimposed to the simulated curve. Up to time $T = 0$, the time at which the two beams are at the maximum of their overlap and the probe laser is fired, the measured collision signal $S_J(T)$ closely follows the simulated curve. Note that the time $T = 0$ is indicated with the vertical dashed line in Figure 5.3. At later times, the scattered OH radicals have moved out of the probe laser volume, and the scattering signal is reduced. Thus under the present experimental conditions, at the time when the probe laser fires, all scattered OH radicals are within the detection laser volume, and are detected with equal probability. This verifies the assumption $P_J(T) = 1$.

A similar analysis is done at collision energies of 80 cm^{-1}, 160 cm^{-1} and 240 cm^{-1} (data not shown), leading to identical conclusions. Thus the LIF detector acts as a flux detector, and a density-to-flux transformation is not required to convert measured scattering signals into cross sections. This favorable situation is facilitated by the small dimensions of the Stark-decelerated packets of OH radicals, and the large probe laser volume that is possible using LIF detection.

5.3.2 Evaluation of excitation functions

To evaluate the collision energy dependence of the cross section for a given scattering channel, i.e., the excitation functions of the state-to-state scattering cross sections, the integrals of Equation 5.2 have to be evaluated for every collision energy E_c. Using $P_J = 1$ for all cases, it is written:

$$\sigma_J(E_c) \propto \frac{S_J(E_c, T)}{g(E_c)\ f(E_c, T)}, \tag{5.5}$$

where the variable E_c has been added to indicate the parameters that depend on the collision energy. The beam overlap factor $f(E_c)$ is given by

$$f(E_c, T) = \int \int_{-\infty}^{T} n_{OH}(E_c, \vec{r}, t)\, n_{NO}(\vec{r}, t) dV_{int}\, dt \tag{5.6}$$

and is evaluated using equations 5.3 and 5.4 and from the parameters given in Table 5.1.

To evaluate excitation functions, without an absolute scale, only the relative dependences of these parameters on the collision energy need to be considered. The NO radical beam is kept constant for each collision energy, and the factor n^{NO}_{max} is omitted when the excitation functions are evaluated. The peak density n^{OH}_{max} of the OH packet, however, strongly depends on the settings of the Stark decelerator. This is illustrated in Figure 5.4, in which the measured peak signal intensity $S_{OH}(E_c)$ of the reagent packets of OH radicals is shown. Two different carrier gases Ar and Kr are used in the experiments to generate the molecular

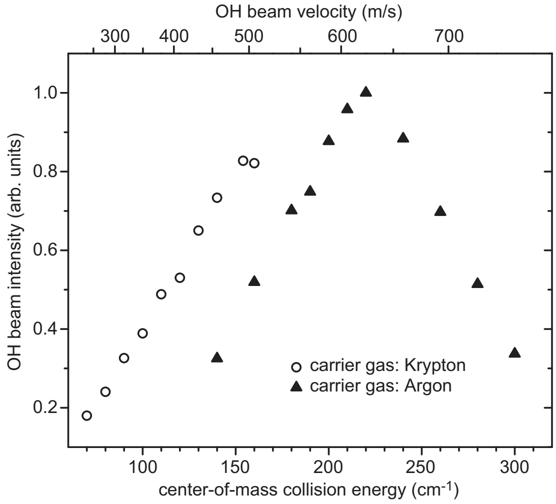

Figure 5.4: Measured peak signal intensities of the reagent packets of OH radicals, as a function of the final velocity of the packet. The final velocities that are produced using the carrier gases Argon and Krypton to generate the molecular beam of OH radicals are indicated by solid triangles and open circles, respectively.

beam of OH radicals. The maximum OH intensity is obtained when Ar is used as a carrier gas, and for $v_{OH} = 625$ m/s. The Stark decelerator is operated at a phase angle $\phi_0 = 0°$ in this case.

The relative peak densities $n_{max}^{OH}(E_c)$ need to be known to evaluate the beam overlap factor $f(E_c, T)$. The relative peak densities are established from the measured relative peak signal intensities $S_{OH}(E_c)$ of the OH packets, that is proportional to the total number $N_{OH}(E_c)$ of reagent OH radicals that is within the probe laser volume: $S_{OH}(E_c) \propto N_{OH}(E_c)$ with:

$$N_{OH}(E_c) = n_{max}^{OH}(E_c) \int (1 - b\, x^2)\, e^{-\beta(y^2+z^2)} dV_{probe} \tag{5.7}$$

Setting $n_{max}^{OH}(E_c = 220 \text{ cm}^{-1}) = 1$, the values for $n_{max}^{OH}(E_c)$ as given in Table 5.1 are obtained.

The excitation functions of the state-to-state scattering cross sections for the collision channels that populate the $(F_1, J = 3/2, e)$, $(F_1, J = 5/2, e)$, $(F_1, J = 7/2), e$ and $(F_2, J = 1/2, e)$ states of OH can now be evaluated for every scattering channel individually, by using Equation 5.5, 5.6, and 5.7 and the parameters from Table 5.1. The result will be given in the forthcoming Section 5.4.

5.3.3 Relating excitation functions at $E_c = 220$ cm^{-1}.

To relate the excitation functions with respect to each other, the relative state-to-state cross sections are evaluated at a single collision energy $E_c = 220$ cm^{-1}. The relative state-to-state inelastic scattering cross sections at this collision energy are determined via additional measurements of the ratios between the collision signals

S_J. The determination of these ratios, however, is complicated by the necessary use of two different laser systems to detect the collision induced population into the four levels.

As described in Chapter 5.2, the collision signals related to the $(F_1, J = 5/2, e)$, $(F_1, J = 7/2, e)$, and the $(F_2, J = 1/2, e)$ scattering channels are detected using a pulsed dye laser, whereas the $(F_1, J = 3/2, e)$ channel can only be probed using a pulsed dye amplified ring dye laser system that offers a superior optical brightness.

The pulsed dye laser has a bandwidth that is sufficiently large to cover the Doppler shifts in the spectral profiles due to the recoil velocities of the scattered particles. Care is taken to excite the optical transitions under saturated conditions. Under these conditions, the fluorescence signal intensities are related to collision induced populations taking the excitation factors ϵ into account that apply to saturated Laser Induced Fluorescence detection, see Chapter 2.7. The excitation factors that apply to the experimental conditions are given in [84] and in Table 3.1. Using Equation 2.90 with these factors, the relative cross sections for the $(F_1, J = 5/2, e)$, $(F_1, J = 7/2, e)$, and the $(F_2, J = 1/2, e)$ channels are determined.

The pulsed dye amplified ring dye laser system has a bandwidth that is much narrower than the Doppler profile of the scattering products. In addition, in order to effectively separate the MDA transitions that probe the initial $F_1, J = 3/2, f$ level from the EDA transitions that probe the $F_1, J = 3/2, e$ level, the transitions must be induced under unsaturated conditions. Hence, the $F_1, J = 3/2, e$ channel is probed by scanning the laser over an energy range that covers the magnetic and electric dipole allowed transitions. The collision induced population in the $F_1, J = 3/2, e$ level is probed by evaluating the integrated intensity difference that results from spectra that are recorded with the voltages on the hexapole to manipulate the NO radical beam switched on and off, respectively.

To relate the $F_1, J = 3/2, e$ channel to the other three channels, the relative state-to-state cross sections for the $F_1, J = 3/2, e$ and the $F_1, J = 5/2, e$ are determined separately. For this, the collision induced population in the $F_1, J = 5/2, e$ channel at a collision energy of 220 cm^{-1} is measured, also using the pulsed dye amplified ring dye laser system. Using Equation 2.88, the ratio in unsaturated fluorescence signal intensities is converted into relative cross sections taking the appropriate Einstein B-coefficients of the transitions into account. The relative cross sections for the $(F_1, J = 3/2, e)$ and $(F_1, J = 5/2, e)$ levels, together with the relative cross sections that are measured for the $(F_1, J = 5/2, e)$, $(F_1, J = 7/2, e)$, and $(F_2, J = 1/2, e)$ levels yield the relative cross sections for all four levels.

5.3.4 Evaluation of absolute cross sections

The relative state-to-state cross sections that are determined at a collision energy of 220 cm^{-1}, together with the excitation functions of the state-dependent cross sections, can be directly compared to the outcome of theoretical calculations.

However, most theoretical calculations also provide absolute values of the cross sections, and it would be very interesting to compare these to experimental values as well. In order to derive absolute cross sections from measured signal intensities, an accurate calibration of the parent beam densities and the absolute number of scattered particles is required. In the discussed experiment the reagent packets of molecules are very well defined, creation a unique position, in which absolute cross sections can be derived from the measured signals that probe the reagent beams and the scattered products. The relative state-to-state cross sections and their excitation functions are accurately determined, with the methods described above. Thus the absolute scattering cross section only needs to be established for a single scattering channel at a single collision energy. It is chosen to evaluate an absolute cross section for the strongest scattering channel at a collision energy where the largest scattering signals are recorded, i.e., for the $F_1, J = 3/2, f \rightarrow F_1, J = 3/2, e$ channel at $E_c = 220$ cm^{-1}.

The cross section σ_J for a given scattering channel J is determined from Equations 5.2 and 5.6:

$$\sigma_J = \frac{N_J}{g f(T)}, \tag{5.8}$$

where the parameter E_c has been dropped since the absolute cross sections is only evaluated at $E_c = 220$ cm^{-1}. The largest difficulty in evaluating the *absolute* numbers for N_J and $f(T)$ is to find the appropriate relation between number of photons detected in the Laser Induced Fluorescence detection scheme, and the corresponding number of molecules that are in the probe laser volume, Equation 2.91. This relationship requires detailed knowledge over the geometry and efficiency of the detection system, which are prone to error. In principle, any errors that are made in this relationship is propagated three times in the final value for the cross section, as this relationship is needed to evaluate the density distributions of both reagent beams and the number of scattered molecules. Here the approach is followed to determine the density distribution of the NO radical beam only, and to measure the *ratio* between the number of reagent and scattered OH radicals, as is explained below.

It is convenient to factor out the peak densities n^{OH}_{max} and n^{NO}_{max} of the reagent beams from the beam overlap function $f(T)$:

$$f'(T) = \frac{1}{n^{OH}_{max} n^{NO}_{max}} f(T). \tag{5.9}$$

The function h is introduced, which describes the volume overlap between the OH reagent beam and the probe laser beam:

$$h = \int (1 - b\,x^2)\, e^{-\beta(y^2+z^2)} dV_{probe} \tag{5.10}$$

such that

$$n^{OH}_{max} = \frac{N_{OH}}{h}. \tag{5.11}$$

Equations 5.8, 5.9 and 5.11 can then be combined to:

$$\sigma_J = \frac{N_J}{N_{OH}} \cdot \frac{h}{g\, f'(T)} \cdot \frac{1}{n_{max}^{NO}}. \tag{5.12}$$

The factor $h/g\, f'(T)$ can be easily evaluated from equations 5.3 and 5.4, and from the parameters of Table 5.1. For the evaluation of the cross section two measurements are needed: a single measurement of the NO beam density and a single measurement of the ratio N_J/N_{OH}, which is directly proportional to the ratio of two detector signals.

The result of the measured NO beam density will be given in Chapter 5.4. The measurement of the ratio N_J/N_{OH} is more complicated. It is inferred from the ratio of the detector signals that are recorded when the reagent and product OH radicals are probed. In principle, for a linear response of the detector, no quantitative knowledge about the detection system is required to accurately measure this ratio. Under the presented experimental conditions, however, the number of product OH radicals $N_J(E_c)$ is orders of magnitude lower than the number of reagent OH radicals $N_{OH}(E_c)$, rendering such measurement difficult. Referring back to Figure 5.2, the magnetic dipole allowed (MDA) $P_1(1)'$ transition to probe N_{OH}, and the electric dipole allowed (EDA) $P_1(1)'$ transition to probe N_J, have been used to circumvent the problem of large signal intensity differences. The advantage of this approach is that information on both N_{OH} and N_J are obtained in a single spectral scan of the narrowband pulsed dye amplified ring dye laser. Both transitions are induced under unsaturated conditions, such that the signal levels that probe N_{OH} and N_J are measured using identical detector settings and characteristics.

The value for N_J/N_{OH} is then established from the measured signal ratio between the EDA transition and the MDA transition in the spectra in Figure 5.2 and the factor k that represents the ratio of transitions strengths of the EDA $P_1(1)$ and the MDA $P_1(1)'$ transitions:

$$\frac{N_J}{N_{OH}} = \frac{1}{k} \times \text{measured signal ratio} \tag{5.13}$$

The value for k is determined from theoretical calculations, see [114] and Chapter 6. In another experiment, discussed in Chapter 6, these calculation have been verified. For these calculations, the population distribution of the OH radicals over the $F = 2$ and $F = 1$ hyperfine levels of the $F_1, J = 3/2, f$ and $F_1, J = 3/2, e$ states must be taken into account. This population distribution of the reagent packet of OH ($F_1, J = 3/2, f$) radicals follows from the hyperfine state dependent transmission efficiency of the Stark decelerator [204]. A population of 77% in the $F = 2$ and 23% in $F = 1$ level is assumed with equal populations in the different M_F states. No polarization effects of the laser and no specific magnetic field direction are taken into account. It is assumed that the $F_1, J = 3/2, f \rightarrow F_1, J = 3/2, e$ inelastic scattering channel is dominated by the $\Delta F = \Delta J = 0$ propensity rule, such that the hyperfine states are conserved during the collision [205]. In

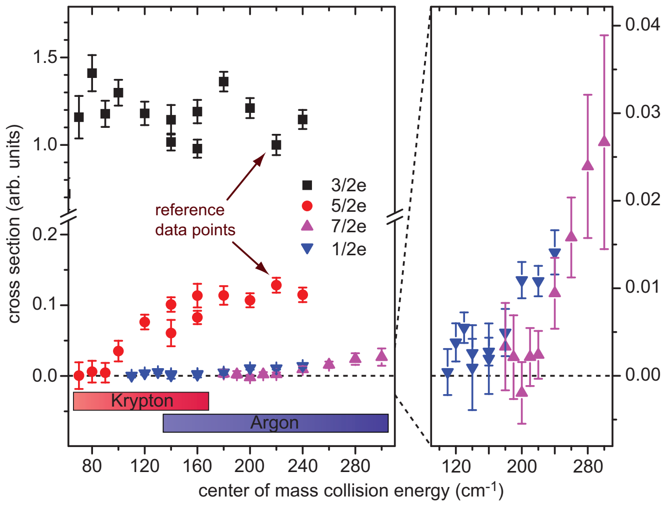

Figure 5.5: Excitation functions for inelastic scattering from the $F_1, J = 3/2, f$ level into the $(F_1, J = 3/2, e)$, $(F_1, J = 5/2, e)$, $(F_1, J = 7/2, e)$ and $(F_2, J = 1/2, e)$ levels. The cross section is given in arbitrary units and is set to unity for excitation into the $F_1, J = 3/2, e$ level at a collision energy at 220 cm^{-1}. The right panel shows the excitation functions of the $F_1, J = 7/2, e$ and $F_2, J = 1/2, e$ levels on an enlarged scale. The two arrows show the datapoints that are used to determine the relative cross section for the $F_1, J = 3/2, e$ and $F_1, J = 5/2, e$ channels at a collision energy of 220 cm^{-1}.

addition, any collision-induced polarization would be largely destroyed by nuclear hyperfine depolarization. Under these conditions, a ratio of $k = 2576$ is found. It is noted that the uncertainty in the value for k is primarily due to uncertainties in the theoretically calculated transition strengths, and the exact experimental conditions such as laser polarization, external magnetic fields, and distribution over the various hyperfine states. The experimental factors can in principle be precisely controlled, see [114] and Chapter 6, although in the present experiment an exquisite level of control was not available. Therefore the accuracy of the value for k is estimated to be about 30%.

5.4 Experimental results

Figure 5.5 shows the result of the excitation function for the $(F_1, J = 3/2, e)$, $(F_1, J = 5/2, e)$, $(F_1, J = 7/2, e)$ and $(F_2, J = 1/2, e)$ levels. The cross section is given in arbitrary units and is set to unity for excitation into the $F_1, J = 3/2, e$ level at a collision energy at 220 cm^{-1}. The right panel in Figure 5.5 shows the excitation functions of the $F_1, J = 7/2, e$ and $F_2, J = 1/2, e$ levels on an enlarged scale. The two arrows show the data-points that are used to determine the relative cross section for the $F_1, J = 3/2, e$ and $F_1, J = 5/2, e$ channels at a collision energy of 220 cm^{-1}, as described in Chapter 5.3.

Two intervals of collision energies are indicated that are covered using Ar and

Kr as a carrier gas to produce the molecular beam of OH. The collision signals at the collision energies of 140 cm^{-1} and 160 cm^{-1} are incorporated in both intervals to ensure overlap between both ranges, i.e., the state-to-state cross sections are measured using OH packets that are produced using different settings of the Stark decelerator resulting in different intensity and spatial distribution of the packets. It is seen that in the region where the two intervals overlap, the data points show satisfactory agreement.

As described in Chapter 5.3 for the determination of the absolute cross sections only the peak density n_{max}^{NO} of the NO reagent beam needs to be determined, i.e. the number N_{NO} of NO radicals in the probe laser volume have to be measured. According to Equation 2.91 the solid angle Ω and the transmission efficiency T of the light collection system, the quantum efficiency Q of the light detector and the excitation factor ϵ, which represents the fraction of the molecules that contributes to the fluorescence signal upon laser excitation need to be known. Using a calibrated spectrometer, a value for T of 0.87 ± 0.05 is measured. The quantum efficiency of the photomultiplier tube (PMT) is specified by the supplier as 0.3 ± 0.03. Optical excitation of the NO radicals is performed under completely saturated conditions, such that $\epsilon = 0.5$.

The solid angle Ω is the most difficult parameter to accurately determine. In contrast to the measurements of the collision signals, no light collection lens is used in these measurements such that Ω is exclusively determined by the distance r of the PMT with respect to the probe volume, and the active area of the PMT which is reduced by a pinhole with 1.0 mm diameter. The number of photons $N_{photons}$ are counted for four different values of r, ranging from 1.5 m to 2.1 m. The results are shown in Figure 5.6(b), and the expected linear dependency of $N_{photons}$ on Ω is observed. It is noted that extrapolation of the fitted line passes through the origin. The experimental error on the value for Ω is estimated from a linear fit of these data points. For the largest solid angle used, on average 3.9 photons per shot are observed, resulting in $N_{NO} = (1.0 \pm 0.3) \times 10^9$ molecules. Using the spatial distribution of the NO packet as defined in equation 5.3 and the probe laser volume V_{probe}, the peak density $n_{max}^{NO} = (9 \pm 3) \times 10^{10}$ molecules cm^{-3} is determined.

Although not required for the evaluation of absolute scattering cross sections, the same procedure is followed to determine the peak density of the packet of OH radicals. This packet has a much lower density than the NO packet, and smaller values of r in combination with a larger pinhole in front of the PMT (diameter is increased to 7 mm) are used to count the number of photons, see Figure 5.6(a). The maximum intensity of the OH packet is obtained for an Ar seeded beam and a velocity of 625 m/s, see Figure 5.4, for which a peak density of $n_{max}^{OH} = (2 \pm 0.8) \times 10^8$ molecules cm^{-3} is determined.

The measurements of n_{max}^{NO} in combination with the ratio between reagent and product number of molecules N_J/N_{OH} can be combined to yield a total inelastic scattering cross section. Note that the ratio N_J/N_{OH} is established from the measured signal ratio between the EDA transition and the MDA transition in

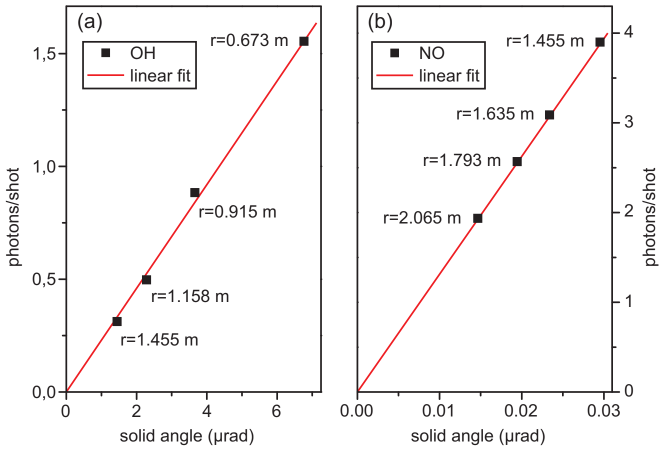

Figure 5.6: Number of photons detected when the reagent packets of OH (panel a) and NO (panel b) are probed via calibrated Laser Induced Fluorescence. The photomultiplier tube that records the emitted photons is mounted at several distances r with respect to the probe volume.

the spectra in Figure 5.2 and the factor k that represents the ratio of transitions strengths of the EDA $P_1(1)$ and the MDA $P_1(1)'$ transitions, as described in Chapter 5.3 and Equation 5.13. For the $F_1, J = 3/2, f \rightarrow F_1, J = 3/2, e$ channel at a collision energy of 220 cm^{-1}, an absolute cross section of 90 ± 38 Å^2 is obtained. Since the excitation functions are already evaluated, the absolute cross sections for all scattering channels and all collision energies are directly derived from this value, shown in Figure 5.7.

The collisions that populate the $F_1, J = 3/2, e$ level are most likely, and the cross section for this transition accounts for about 90% of the total inelastic scattering cross section. The cross sections to populate the $(F_1, J = 5/2, e)$, the $(F_1, J = 7/2, e)$, and the $(F_2, J = 1/2, e)$ levels show a clear threshold behavior; the collision energies at which these channels become energetically possible are indicated by vertical arrows in Figure 5.7. These cross sections show large qualitative differences compared to the scattering of OH with atomic targets [146]. The most striking difference is found in the relative contributions of the $(F_1, J = 3/2, e)$ and $(F_1, J = 5/2, e)$ channels to the total inelastic scattering cross section. The role of the $(F_1, J = 3/2, e)$ channel, which dominates rotational energy transfer for OH-He and OH-Ne, gradually reduces in favor of the $(F_1, J = 3/2, e)$ channel in the series of targets He, Ne, Ar, Kr, and Xe [146]. This behavior could be rationalized from the increasing well depth, anisotropy, and head-tail asymmetry of the two BO PESs [146, 206]. The overwhelming dominance of the $F_1, J = 3/2, f \rightarrow F_1, J = 3/2, e$ quenching channel observed for OH-NO reflects how a dipolar open-shell molecular scattering partner rather than a spherical atomic partner governs the collision dynamics.

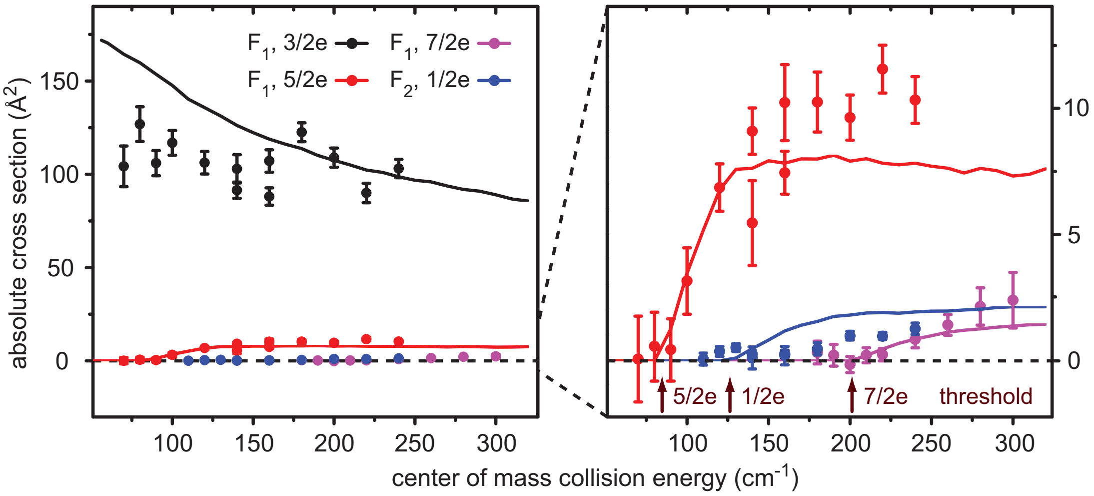

Figure 5.7: Comparison of the collision energy dependence of the measured (data points with error bars) and calculated (solid curves) state-to-state inelastic scattering cross sections of OH ($F_1, J = 3/2, f$) radicals in collision with NO ($F_1, J = 1/2, f$) radicals. The cross sections are first measured relatively with respect to each other, and the vertical error bars represent the statistical spread of the data as obtained from repeated runs of the experiment. The vertical axis was then put to an absolute scale by a single measurement of the absolute cross section for the $F_1, J = 3/2, e$ channel at a collision energy of 220 cm^{-1}. The cross sections were computed on an energy grid of 10, 20, 30, 40,..., 320 cm^{-1}. The cross section for the dominant $F_1, J = 3/2, e$ is converged to within a few percent; the cross sections for the weaker channels vary by $20-50\%$ with respect to changes in the theoretical model [207].

5.5 Theoretical calculations

The theoretical model was developed by the Theoretical Chemistry Nijmegen group of Groenenboom. A detailed description is found in the supplementary information of [207], here only a short overview is given. In order to interpret the experimental results, a model for the scattering of two molecules in an open shell $^2\Pi$ state is constructed. In contrast to scattering of OH or NO with rare gas atoms, Chapter 3.3 and [82, 84, 146, 154], ab initio calculations of multiple anisotropic PESs with their non-adiabatic couplings for OH-NO are beyond the capabilities of current theoretical methods. Coupling of the $S = 1/2$ electron spins gives rise to singlet ($S = 0$) and triplet ($S = 1$) potentials, which describe different short-range exchange interactions. There are four spatially distinct electronic states for each spin state, which are degenerate at long range and for linear geometries and which are coupled by non-adiabatic interactions. Nuclear derivative couplings with respect to all nuclear degrees of freedom exist between these states. Ab initio studies of the OH-NO complex [208] focused on the region where the chemical reaction $OH + NO \rightarrow H + NO_2$ takes place, but considered only the lowest adiabatic potential for the singlet state. Even if it would be possible to compute all the relevant adiabatic PESs, there would be no simple recipe to take the non-adiabatic couplings between the PESs into account.

The theoretical model exploits the following hypothesis: The processes with the largest cross sections are governed by couplings that occur at relatively large OH-NO separations, beyond the HONO well region. As opposed to the short range interactions, the long-range parts of the PESs can be calculated accurately by ab initio methods. The complicated short-range behavior of the PESs is neglected and replaced with an isotropic repulsion term. However, the model accurately calculates the long-range PESs that are governed by first-order electrostatic interactions between the dipole, quadrupole, and octupolemoments of the collision partners [207]. Moreover, it includes isotropic dispersion and induction terms. The intermolecular Hamiltonian contains the usual radial and centrifugal kinetic energy operators, and the full 4×4 matrix of diabatic interaction potentials [207]. Due to the non-cylindrical symmetry of the $^2\Pi$ ground states of both the OH and NO radical, the off-diagonal elements of this matrix provided by the quadrupole and octupole moments of both radicals contain important couplings between the $^2\Pi_{3/2}$ and $^2\Pi_{1/2}$ states of both species.

The cross sections that are obtained from the model PESs by full coupled-channels calculations are shown as solid lines in Figure 5.7. Fair agreement between experiment and theory is obtained, in particular considering the simplistic approximations for the short-range PESs that are made. The absolute value for the cross section of the dominating $F_1, J = 3/2, e$ channel, as well as the relative strengths of the inelastic channels, is reproduced well by the model calculations. The cross section for the spin-orbit changing $F_2, J = 1/2, e$ channel, as well as the cross section for the $F_1, J = 3/2, e$ channel at low collision energies, is overestimated by the model.

The sensitivity of the model calculations are tested with respect to changes in the short-range repulsion term [207]. This test shows that the cross section for the parity-changing $F_1, J = 3/2, e$ channel is governed exclusively by the long-range electrostatic interaction; its value is converged within a few percent. About half of this large quenching cross section originates from collisions with impact parameters exceeding 12 a_0. The $F_1, J = 5/2, e$ channel is also mainly determined by the long-range forces, although its cross section varies by $10-25\%$ upon changes in the short-range model parameters [207]. The weak $F_1, J = 7/2, e$ and $F_2, J = 1/2, e$ channels show larger variations, and more realistic short-range PESs are required to accurately predict their cross sections.

5.6 Conclusion

The measurements of absolute inelastic scattering cross sections for collisions between state-selected OH and state-selected NO radicals epitomize the level of sensitivity and precision that can be reached nowadays in collision experiments using state-of-the-art beam manipulation techniques.

The comparison between the theoretical model and the experiment shows that the main mechanisms of rotational energy transfer in systems as studied here, that are chemically reactive in nature and have a seemingly unsurmountable complexity, are captured using a model for the long-range interactions alone, provided that the full monomer Hamiltonians and all relevant long-range non-adiabatic couplings are taken into account. Even at relatively high collision energies, the inelastic scattering events with the largest cross sections predominantly occur at large intermolecular distances where the interaction potentials can be calculated accurately. The success attained here implies that reliable predictions for state-to-state scattering cross sections can now be made for complex molecular systems involving radicals, helping to solve urgent scientific questions in, for instance, astrochemistry. Ultimately, new electronic structure methods that include the chemically reactive short-range potentials are required to elucidate the exact mechanisms of radical-radical collisions. The detailed experimental data on bi-molecular scattering that can now be obtained will also stimulate the development of advanced theory in this field.

This experiment is the first crossed beam inelastic scattering experiment of two state-selected open-shell radical species with quantum-state-selectivity in the detection process, and it opens new research avenues to unravel energy transfer between two molecules. The theoretical model also predicts the final states of the NO radical that are populated in coincidence with rotational energy transfer in the OH radical, but that cannot be probed with the present experimental arrangement. Nevertheless, the experiment is well suited to be combined with the velocity map imaging technique to record differential cross sections, for instance. This would also allow for the measurement of collision induced energy transfer that occur in both molecules from individual encounters, i.e, product pair correlations that reveal a kinematically complete picture of the scattering process. The NO radical would be particularly amenable to these kind of studies. By orienting or aligning both reagent molecules, the influence of the mutual orientation on the collision outcome can be studied, revealing the full complexity of the stereodynamics when individual molecules interact.

Extending the level of control over the hexapole state-selected beam is another exciting avenue. Numerical trajectory simulations indicate that replacement of the hexapole for a second Stark decelerator will reduce the reagent product density by less than a factor five, suggesting that the scattering of two Stark-decelerated beams is experimentally feasible [209]. This would enable the study of bi-molecular collisions at collision energies in the $1-500$ cm^{-1} range and with an energy resolution of a fraction of a wavenumber. This offers unique prospects for the study of threshold phenomena with improved energy resolution, for the observation of shape and Feshbach resonances that are predicted to occur at low collision energies and around energetic thresholds, and for controlling dipole-dipole interactions in cold molecular collisions with external electric or magnetic fields. In Chapter 7 of this thesis an experiment on the first deceleration of NO radicals is discussed, which could form the basis for future collision experiments using two crossed Stark-decelerated beams.

Chapter 6

Magnetic dipole allowed transitions in the OH $A\,^2\Sigma^+ \leftarrow X\,^2\Pi$ system

In this Chapter the observation of magnetic dipole allowed transitions in the well-characterized $A\,^2\Sigma^+ - X\,^2\Pi$ band system of the OH radical is reported. A Stark decelerator in combination with microwave Rabi spectroscopy is used to control the populations in selected hyperfine levels of both Λ-doublet components of the $X\,^2\Pi_{3/2}, v = 0, J = 3/2$ ground state. The theoretical calculations presented in this Chapter predict that the magnetic dipole transitions in the $\nu' = 1 \leftarrow \nu = 0$ band are weaker than the electric dipole transitions by a factor of 2.58×10^3 only, i.e., much less than commonly believed. The experimental data confirm this prediction.

Based on:
Magnetic dipole transitions in the OH $A\,^2\Sigma^+ \leftarrow X\,^2\Pi$ system,
M. Kirste, X. Wang, G. Meijer, K. B. Gubbels, A. van der Avoird, G. C. Groenenboom, and S. Y. T. van de Meerakker, J. Chem. Phys. **137**, 101102, 2012.

6.1 Introduction

The hydroxyl radical (OH) plays a central role in many areas of chemistry and physics, and is one of the most extensively studied molecular species to date. In 1950, Meinel discovered that emission from vibrationally excited OH radicals in the Earth's atmosphere is responsible for the infrared night-time air glow [210]. Detection of the 18 cm absorption lines in the radio spectrum of Cassiopeia A by Weinreb et al. in 1963 revealed the presence of OH in interstellar space [199]. Shortly after, the OH radical was identified as the first molecule to form astrophysical (mega)masers [211, 212]. Since then, a wealth of spectroscopic investigations has been carried out in the microwave, infrared, and ultraviolet part of the spectrum, unravelling the electronic, vibrational, rotational, and hyperfine structure of the OH radical.

The OH ($^2\Pi$) radical (together with the similar NO ($^2\Pi$) radical) has also been established as the paradigm for molecular collisions studies. Interest in these open-shell radical species stems from their importance in combustion and atmospheric environments, as well as from their complex rotational structure that exhibits spin-orbit and Λ-doublet splittings. Ingenious methods have been developed to select OH ($^2\Pi$) radicals in a single rotational (sub)level, to orient them in space [15, 213], and to tune their velocity [82, 84]. These methods have allowed collision experiments of transient species at the fully state-resolved level, and have contributed enormously to our present understanding of how intermolecular potentials govern molecular collision dynamics. Also in Chapter 3 and 5 of this thesis experiments on the collision of OH radicals with He, D_2, and NO are reported.

Recently, the OH radical has emerged as a benchmark molecule in the rapidly developing field of cold molecules [77]. The OH radical was one of the first molecular species to be slowed down [202] and to be confined in traps [75]. In the near future, comparison of high-resolution spectroscopic data on cold OH radicals in the laboratory with interstellar megamaser observations may reveal a possible time variation of fundamental constants [81].

In the vast majority of experiments, ground state OH radicals are detected via Laser Induced Fluorescence (LIF) after optical excitation on electric dipole allowed (EDA) transitions of the $A\,^2\Sigma^+ \leftarrow X\,^2\Pi$ band using a pulsed dye laser, see Chapter 2.7. An important property of the $A-X$ band is that it allows one to selectively probe the population of individual Λ-doublet components of opposite parity within a rotational state, see Chapter 2.2.4 and Figure 2.2. Although the Λ-doublet splittings are typically much smaller than the bandwidth of pulsed dye lasers, the measurement of populations in selected Λ-doublet components is facilitated by the parity selection rules of EDA transitions and the large energy splitting between levels of opposite parity in the $A\,^2\Sigma^+$ state. The selection rules of EDA transitions are discussed in Chapter 2.2.4 and the common EDA transition, which are used for the detection of the OH ($X\,^2\Pi_{3/2}, J = 3/2$) ground state are seen in the inset to Figure 6.1. Similar schemes are used to probe Λ-

doublet component resolved populations in other $^2\Pi$ molecules such as NO, CH, and SH.

Extreme care, however, must be taken when using this approach. In the experiment reported in Chapter 5, molecular beams of OH with an almost perfect quantum state purity were produced via the Stark deceleration technique. In these experiments, $\geq$ 99.999% of OH radicals in the $^2\Pi_{3/2}, J = 3/2$ rotational ground state reside in the upper Λ-doublet component of f symmetry; the lower Λ-doublet component of e symmetry is effectively depopulated in the Stark-deceleration process. When the populations in the e and f components were probed using LIF via the $A \leftarrow X$ transition, however, the apparent population in the e state appeared at least one order of magnitude too large. A spectroscopic re-investigation using a laser with a much narrower bandwidth revealed that magnetic dipole allowed (MDA) transitions were responsible for this effect [207].

Magnetic dipole allowed transitions have rarely been observed in laser excitation spectra of heteronuclear molecules [113]. Their existence is generally neglected in quantitative measurements of state populations, potentially leading to a significant misinterpretation of detector signals. In homonuclear molecules, MDA transitions between electronic states are well known to result in “forbidden” band systems that violate the rigorous selection rules for electric dipole transitions. The most famous example is the atmospheric oxygen band, which appears in the red part of the solar spectrum. In contrast, MDA transitions in heteronuclear molecules mostly exist as weak satellite lines parallel to strong EDA transitions. The general rule of thumb is that MDA transitions are about a factor 10^5 weaker than the corresponding EDA transitions [107]. Already in the 1920’s, weak satellite lines in the $A - X$ emission band of OH were observed that appeared to correspond to transitions to the “wrong” Λ-doublet component [108,109,110,111]. These lines were tentatively attributed to the MDA transitions by Van Vleck in 1934 [112], but received little attention ever since.

In this Chapter a detailed analysis of MDA transitions in the $A\,^2\Sigma^+ \leftarrow X\,^2\Pi$ band of OH is presented. The experiment shows that the satellite MDA transitions are surprisingly strong, and only three orders of magnitude weaker than the main EDA transitions. In the experiment a Stark-decelerator is used to produce packets of OH radicals that reside exclusively in the upper Λ-doublet component of f symmetry. A controlled fraction of the population is transferred to the lower component of e symmetry by using a microwave field. The MDA and EDA $A\,^2\Sigma^+, v = 1 \leftarrow X\,^2\Pi, v = 0$ transitions originating from the f and e level, respectively, are spectroscopically resolved using a narrowband pulsed dye laser. The observed ratio of the signal intensities agrees well with theoretical calculations for the EDA and MDA transition strengths.

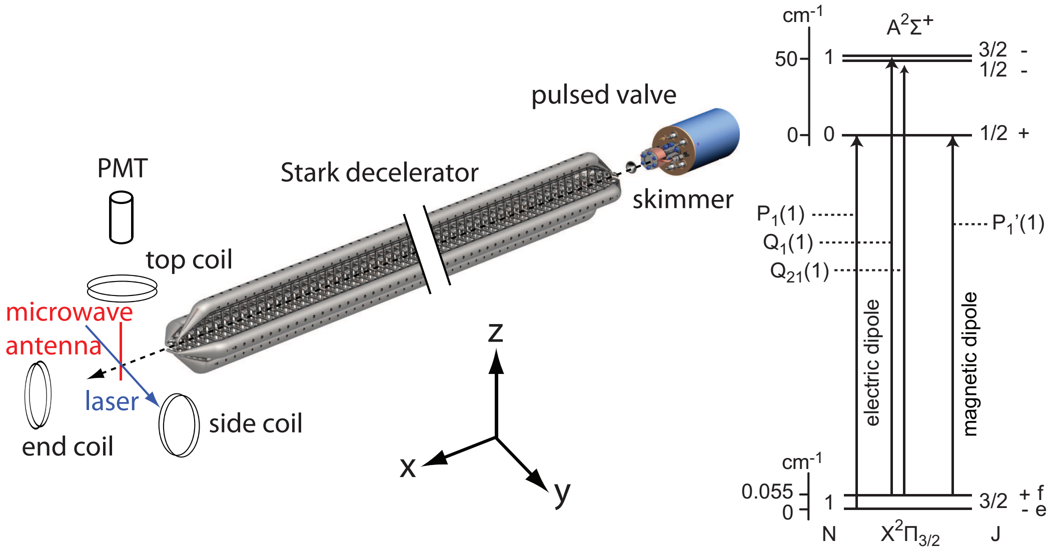

Figure 6.1: Scheme of the experimental setup. The inset shows the electric dipole allowed and magnetic dipole allowed transition used for the detection of the two Λ-doublet components in the OH ground state.

transition	frequency (kHz)
$\|X, f, +, F = 1\rangle \rightarrow \|X, e, -, F = 2\rangle$	1612231.01 [106]
$\|X, f, +, F = 1\rangle \rightarrow \|X, e, -, F = 1\rangle$	1665401.803 [81]
$\|X, f, +, F = 2\rangle \rightarrow \|X, e, -, F = 2\rangle$	1667358.996 [81]
$\|X, f, +, F = 2\rangle \rightarrow \|X, e, -, F = 1\rangle$	1720529.98 [106]

Table 6.1: Transition frequencies of the four Hyperfine transitions in the OH $X\,^2\Pi_{3/2}, v = 0, J = 3/2$, ground state.

6.2 Experiment

The relevant energy levels and electronic transitions are shown in the inset to Figure 6.1. As it was described in Chapter 2.2, the electronic ground state of OH has a $X\,^2\Pi$ configuration. Each rotational level, labeled by J, splits into two Λ-doublet components which are separated by 0.055 cm^{-1} for the $J = 3/2$ rotational ground state [99]. The upper and lower components have $+$ and $-$ parity, and are indicated by the spectroscopic labels f and e, respectively [97]. Each of the Λ-doublet components of the $J = 3/2$ state is split into $F = 1$ and $F = 2$ hyperfine levels, see Chapter 2.2.3. The four resulting levels are referred to hereafter as $|X, f, +, F = 2\rangle$, $|X, f, +, F = 1\rangle$, $|X, e, -, F = 2\rangle$ and $|X, e, -, F = 1\rangle$. The four transition frequencies between these levels have been measured by ter Meulen et al. [106] and their results have been recently improved by Hudson et al. [81]. Their results are given in Table 6.1.

The first electronically excited state of OH has a $A\,^2\Sigma^+$ configuration. In this experiment, only the $N = 0, J = 1/2$ rotational ground state of $+$ parity is of relevance. This state is split into two hyperfine states $F = 0$ and $F = 1$ that are separated by 0.026 cm^{-1}, and are referred to hereafter as $|A,+,F=0\rangle$ and $|A,+,F=1\rangle$. The EDA ($P_1(1)$) and MDA ($P_1'(1)$) $A-X$ transitions couple the $|X,e,-\rangle$ and $|X,f,+\rangle$ states to the $|A,+\rangle$ states following the parity changing and parity conserving selection rules for EDA and MDA transitions, Equation 2.30 to 2.36 and Equation 2.39 to 2.45, respectively.

The experimental setup is schematically shown in Figure 6.1. The Stark decelerator is the same as described in Chapter 2.5, Chapter 3, and Chapter 5. A packet of OH ($X\,^2\Pi_{3/2}, v=0, J=3/2, f$) radicals with a velocity of 448 m/s is produced by passing a molecular beam of OH through the 2.6 meter long Stark decelerator [83]. The Stark decelerator efficiently deflects molecules in the $|X,e,-\rangle$ states. A phase angle $\phi_0=50°$ is used to ensure that the OH radicals that exit the decelerator reside exclusively in the $|X,f,+,F=2\rangle$ state. The end of the Stark decelerator is electrically shielded to prevent any electric stray fields to penetrate into the interaction area.

A controlled fraction of the OH radicals is transferred into the $|X,e,-,F=1\rangle$ state by inducing the $|X,f,+,F=2\rangle \rightarrow |X,e,-,F=1\rangle$ transition at 1.72 GHz with a microwave pulse. For this purpose a 90 mm long microwave antenna is installed 38 mm downstream from the decelerator and perpendicular to the molecular beam axis. No frequency-matched microwave resonator is used. The microwaves are reflected by the vacuum chamber walls filling the whole vacuum chamber, and the microwaves are assumed to be unpolarized. The microwave duration and power can be controlled via a microwave switch and attenuator, respectively. The magnetic field in the interaction region is controlled by three copper coils with a diameter of 31 cm each, that are mounted 30 cm from the interaction area. One coil is positioned above the interaction area, one at the side and one at the end.

Two lasers are used to detect the OH radicals via LIF using the 1-0 band of the OH $A\,^2\Sigma^+ \leftarrow X\,^2\Pi_{3/2}$ transition around 282 nm. The first laser, a pulsed dye laser (PDL) with a bandwidth of 1.8 GHz, is used to probe the population in the $|X,e,-\rangle$ state via the EDA $P_1(1)$ transition. The second laser, a pulsed dye amplifier (PDA) seeded by a single mode ring dye laser, has a bandwidth of 120 MHz and is used to separate the $P_1(1)$ and $P_1'(1)$ transitions. The power of the PDL and PDA lasers are adjusted to ensure that the transitions are induced under saturated and unsaturated conditions, respectively, and both lasers are linearly polarized in the z direction (see Figure 6.1 for the definition of the coordinate system). The off-resonant fluorescence is imaged into a photomultiplier tube (PMT), and the influence of the coils on the PMT is incorporated in the analysis of the data.

6.3 Results

In the presence of a magnetic field, the $F=1$ and $F=2$ hyperfine states split into 3 and 5 M_F Zeeman sublevels, respectively, that are readily resolved in the microwave spectrum. This is illustrated in Figure 6.2(a) that shows the

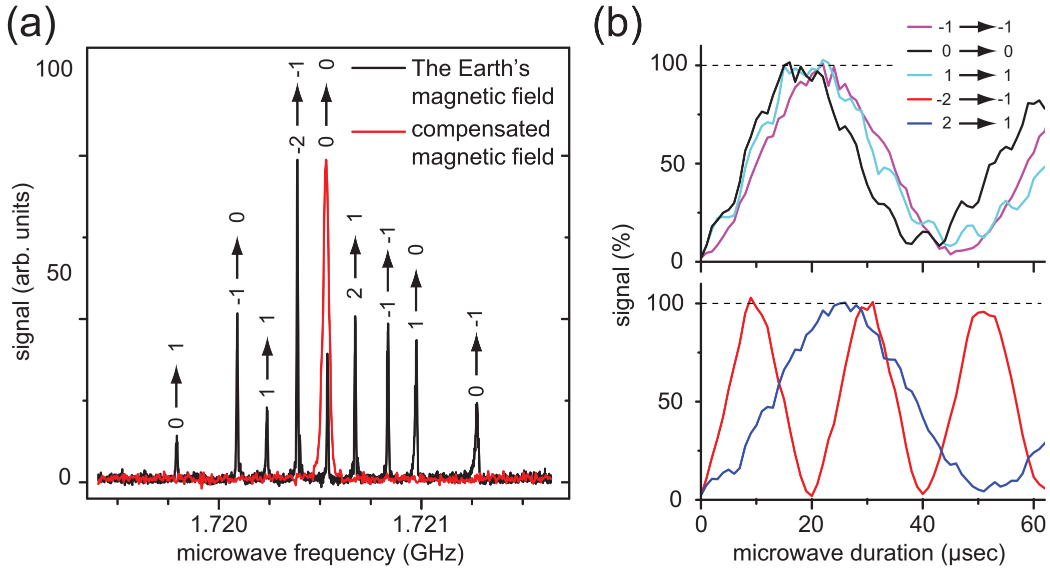

Figure 6.2: (a): Frequency scan over the $|X, f, +, F = 2\rangle \rightarrow |X, e, -, F = 1\rangle$ transition in the presence of the Earth's magnetic field (black) and the compensated magnetic field (red). Spectra are scaled to each other to fasciliate a better comparison. The nine $|X, f, +, F = 2, M_F\rangle \rightarrow |X, e, -, F = 1, M_F\rangle$ transitions are indicated. (b): Rabi oscillations of selected $|X, f, +, F = 2, M_F\rangle \rightarrow |X, e, -, F = 1, M_F\rangle$ transitions.

$|X, f, +, F = 2\rangle \rightarrow |X, e, -, F = 1\rangle$ spectrum around 1.72 GHz, recorded with the broadband PDL system. In the black spectrum no currents are applied to the coils, and nine transitions can be identified corresponding to the nine allowed $|X, f, +, F = 2, M_F\rangle \rightarrow |X, e, -, F = 1, M_F\rangle$ transitions that are split by the Earth's magnetic field.

For an unambiguous interpretation of the EDA and MDA $A{-}X$ transitions, and to measure their relative strengths, it is convenient to choose the laser polarization direction parallel to the space quantization axis. The Earth's magnetic field, however, is not suitable for this, as the direction of the magnetic field vector is in general not parallel to the laser polarization axis. Instead, by applying currents to the three coils the Earth's magnetic field is compensated, and then a controlled magnetic field is applied that is parallel to the z axis, i.e., the laser polarization axis. For a definition of the coordinate system, see Figure 6.1. In general the three coils can be used to create any desired direction for the magnetic field vector.

The red curve in Fig. 6.2(a), shows the microwave spectrum that is recorded when currents of 2.10 A, 1.60 A and 0.35 A are passed through the top, side and end coils, respectively. It is seen that in this configuration the Earth's magnetic field is compensated and the nine lines merge into one. An additional magnetic field in the z direction can be added by changing the current in the top coil, while keeping the current in the other coils constant. For the measurement of the EDA and MDA transition it is chosen to reverse the current in the top coil to generate a magnetic field with a magnitude that is twice as large as the z-component of the Earth's magnetic field.

A controlled fraction of the population in each of the $|X, f, +, F = 2, M_F\rangle$ levels can be transferred to an individual M_F component of the $|X, e, -, F = 1\rangle$ level by applying a microwave pulse with a controlled pulse duration and power. In Figure 6.2(b), the fluorescence intensity is shown, that is measured for five different microwave transitions as a function of the microwave pulse duration. Clear Rabi oscillations are observed, with different Rabi frequencies for each transition due to the differences in transition strength and the unpolarized microwave radiation. Each Rabi oscillation maxima corresponds to 100% pumping of that specific ΔM_F transition. The Rabi oscillations are measured for all nine transitions shown in Figure 6.2(a), and for each transition it is observed that the maxima of the oscillations yield equal signal intensity. Thus, the OH radicals that exit the Stark decelerator are equally distributed over the five M_F levels of the $|X, f, +, F = 2\rangle$ state before the microwave field is applied. This result is of particular importance for collision experiments using Stark-decelerated beams, where Hyperfine propensities are observed, because no M_F selection prior to the collision takes place. In most experimental setups a small residual magnetic field is present, which splits the hyperfine states in the M_F Zeeman sublevels, and it is extremely difficult to experimentally shield small residual magnetic fields e.g. the Earth magnetic field.

For the measurement of the ratio of EDA and MDA transition, three different microwave transitions are induced that transfer population from the $|X, f, +, F = 2, M_F = 0\rangle$ into the $M_F = 1$, $M_F = 0$ and $M_F = -1$ levels of the $|X, e, -, F = 1\rangle$ state, respectively. These transitions are indicated by the red, black and blue arrows in the inset in Figure 6.3. For each transition, the microwave pulse duration and power is carefully chosen to transfer (2.5±1)% of all molecules from the $|X, f, +, F = 2, M_F = 0\rangle$ level. Since this $M_F = 0$ level contains one fifth of all $F = 2$ molecules, 99.5±0.2% of the OH radicals remain in the $|X, f, +, F = 2\rangle$ state, in all three cases. The error (2σ) is given by the statistical spread of the Rabi oscillations. The benefit of using three different microwave transitions is that the ratio of to EDA and MDA transition can be compared for three cases with different selection rules.

The EDA $P_1(1)$ and MDA $P_1'(1)$ $A - X$ transitions are then investigated in these three cases by probing the populations in the $|X, e, -\rangle$ and $|X, f, +\rangle$ states with the narrowband PDA system. This laser can spectroscopically resolve the Λ-doublet splitting in the $|X\rangle$ state and the hyperfine splitting in the $|A\rangle$ state, but not the hyperfine splittings in both $|X\rangle$ states or any Zeeman splittings. The EDA and MDA transition obey the selection rules which are discussed in Chapter 2.2.4. The laser polarization and magnetic field direction create additional selection rules. For parallel laser polarization and magnetic field direction, both the EDA and the MDA transitions obey the hyperfine selection rule ΔF=0,±1, Equation 2.36 and 2.45. The EDA transition has the additional selection rule ΔM_F=0 (with $\Delta F \neq 0$ for $M_F = 0$), while MDA transitions can only couple states with

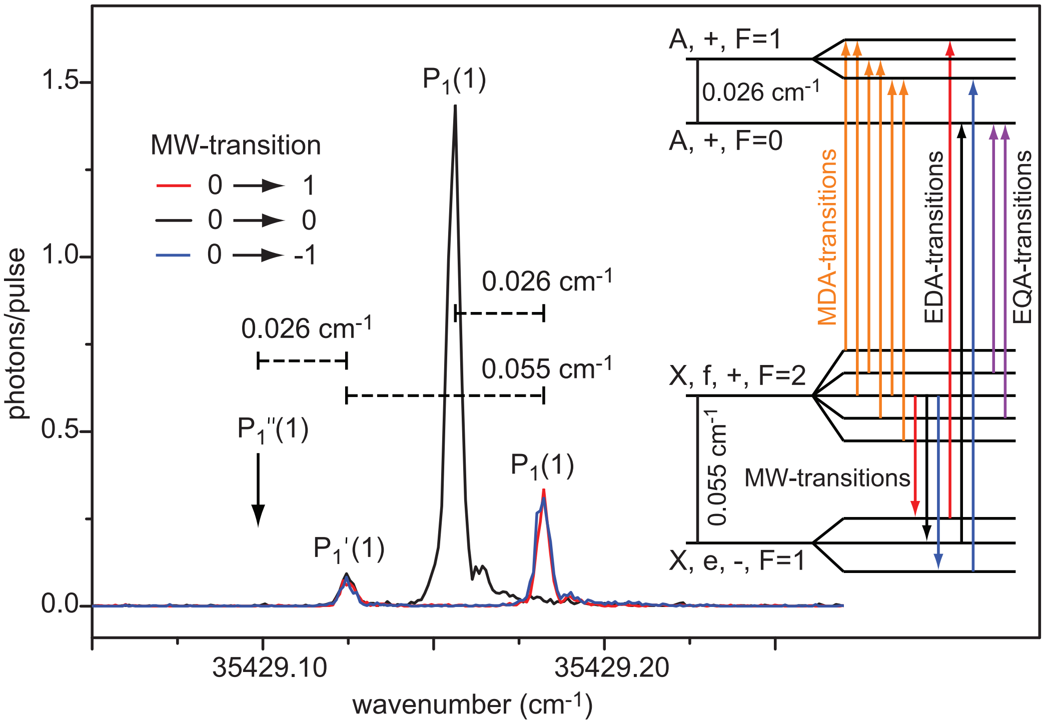

Figure 6.3: The EDA and MDA OH(A-X) transitions for three different microwave transitions (marked red,black and blue). The corresponding microwave transitions to prepare a population in selected M_F components of the $|X, e, -, F = 1\rangle$ state are shown in the inset and the EDA $P_1(1)$, MDA $P_1'(1)$ and EQA $P_1''(1)$ transitions are indicated. The $|X, f, +, F = 1\rangle$ and $|X, e, -, F = 2\rangle$ levels are not shown in the inset, because the experiment does not populate these levels. The arrow indicates the position of possible EQA transitions $P_1''(1)$.

$\Delta M_F{=}\pm1$. As indicated in Figure 6.3, there are thus six MDA transitions and only one EDA transition for each case.

In Figure 6.3 the MDA $P_1'(1)$ and the EDA $P_1(1)$ transitions are shown that are recorded in the three cases. The MDA $P_1'(1)$ transitions appear at the same position and with equal intensity in all spectra. Depending on the M_F level that is populated in the $|X, e, -, F = 1\rangle$ state, the EDA $P_1(1)$ transition either couples to the $|A, +, F = 0\rangle$ (for $M_F = 0$) or the $|A, +, F = 1\rangle$ state (for $M_F = \pm1$). These transitions are clearly resolved in the spectra. The former transition appears four times more intense than the latter two transitions that are of equal intensity. This is theoretically expected, as it is discussed in the forthcoming Chapter 6.5. The Λ-doublet splitting is also recognized.

The ratio of the fluorescence intensities of the EDA $|A, +, F = 0\rangle \leftarrow |X, e, -, F = 1, M_F = 0\rangle$ transition and the combined six MDA $|A, +, F = 1\rangle \leftarrow |X, f, +, F = 2\rangle$ transitions is estimated to be (18±8). This value is obtained by comparing the strong central with the left peak in Figure 6.3. The experimental error is mainly given by the statistical error of the population transfer in the microwave field from the $|X, f, +, F = 2, M_F = 0\rangle$ to the $|X, e, -, F = 1, M_F\rangle$ levels.

Having observed the MDA transition one might wonder about the presence of electric quadrupole allowed (EQA) transitions. Also the EQA transitions obey the selection rules which are discussed in Chapter 2.2.4, and the laser polarization and magnetic field direction create additional selection rules. An EQA transition can couple states with $\Delta F{=}\pm 2$, Equation 2.52. Since the laser propagates in the y-direction and is polarized in the z-direction, only the (space-fixed) Q_{zy} component of the transition quadrupole moment is non-zero, see Eq. (4.13.9) in [214]. This leads to the EQA selection rule $\Delta M_F = \pm 1$. In the experiment no EQA $|A, +, F = 0\rangle \leftarrow |X, f, +, F = 2\rangle$ transition was observed, see Figure 6.3. Electric quadrupole transitions with $\Delta F = 0, \pm 1$ should be in the same order of magnitude as transitions with $\Delta F = \pm 2$ and can therefore be neglected. Hence, EQA transitions in the OH (A-X) band are at least two orders of magnitude weaker than MDA transitions. This finding is supported by the theoretical estimate of the EQA transition strength, see forthcoming Chapter 6.5.

6.4 Theoretical treatment of EDA and MDA transitions in OH

The strengths of the EDA and MDA transitions are calculated from the magnitude of the two transition dipole moments, given by:

$$|\langle \mu^{\mathrm{bf}}_{\mathrm{el/mag}} \rangle| = \left| \left\langle A\,^2\Sigma^+, v = 1 \right| \hat{\boldsymbol{\mu}}_{\mathrm{el/mag}} \left| X\,^2\Pi, v = 0 \right\rangle \right|, \tag{6.1}$$

with the electric/magnetic dipole moment operator $\hat{\boldsymbol{\mu}}_{\mathrm{el/mag}}$. The transition dipole moments are calculated with the MOLPRO program package [215]. The calculations were performed by the Theoretical Chemistry Nijmegen group of Groenenboom and the details are given in the supplementary material to [114]. Here only the result is given.

Both transition dipole moments are determined in the body-fixed frame, that is the frame with its z axis along the OH bond vector. For the electronic potential the theoretical calculations used a potential calculated by Loo and Groenenboom [216]. The result of the MOLPRO calculations is: $|\langle \mu^{\mathrm{bf}}_{\mathrm{el}} \rangle| = 0.05249$ and $|\langle \mu^{\mathrm{bf}}_{\mathrm{mag}} \rangle| = 0.1417$ in atomic units.

Both transition dipole moments only have components perpendicular to the body fixed z axis, i.e. the OH bond vector. The projection of the electric and the magnetic dipole moment on the body fixed z axis is introduced:

$$\mu^{\mathrm{bf}}_{\mathrm{el},\pm 1} = i\frac{\langle \mu_{\mathrm{el}} \rangle}{\sqrt{2}} \qquad \text{and} \qquad \mu^{\mathrm{bf}}_{\mathrm{mag},\pm 1} = \mp\frac{\langle \mu_{\mathrm{mag}} \rangle}{\sqrt{2}}, \tag{6.2}$$

and in both cases $\mu^{\mathrm{bf}}_{\mathrm{el/mag},0} = 0$. Similar to the description of the Stark effect in Chapter 2.3, these transition dipole moments are spherical tensor operators of rank 1, see [95]. To compare the experimental results to the theoretical results a transformation from the body-fixed (molecular) frame to the space-fixed (laboratory) frame is needed. After this transformation the laser polarization and the different state population are considered. The corresponding space-fixed transition dipole moments are given by

$$\mu^{\mathrm{sf}}_{\mathrm{el/mag},m} = \sum_k \mu^{\mathrm{bf}}_{\mathrm{el/mag},k} D^{(1)*}_{mk}(\phi,\theta,0), \tag{6.3}$$

with ϕ and θ the Euler angles, and $D^{(1)}_{mk}(\phi,\theta,0)$ the Wigner rotation matrices, see [95] and Equation 2.55.

In the experiment different hyperfine transitions are used for the comparison of the EDA and the MDA transition. Therefore the dipole moments have to be calculated in a basis set that involves the Hyperfine structure, see Chapter 2.2.3. It is convenient to first calculate the dipole moments in a pure Hund's case (a) basis set, Equation 2.2, which is not yet parity adapted and does not consider the mixing of wavefunctions with different Ω in the ground state $X\,^2\Pi$. Parity adaptation and the Ω mixing are afterwards easily incorporated in the analysis. They are considered by a sum of the parity adapted wavefunctions with the mixing coefficients C_1 and C_2, see Equation 2.18.

The Hund's case (a) wavefunctions from Equation 2.2 are extended by the Quantum numbers I for the total nuclear spin, F for the total angular momentum that involves the nuclear spin and M_F which is the projection of F on an external quantization axis, see Chapter 2.2.3. In the experiment this external quantization axis is given by the magnetic field. The basic wavefunctions are

$$|n\,\Lambda; S\,\Sigma; \nu; J\,\Omega\,M_J\,I\,F\,M_F\rangle \tag{6.4}$$

Note that these basis states are not yet parity adapted.

All MDA and EDA transition in this analysis are in the same band $A\,^2\Sigma^+, v = 1 \leftarrow X\,^2\Pi, v = 0$. The exited state $A\,^2\Sigma^+$, can also be described as Hund's case (a), see [93] and Chapter 2.1. Hence the basic wavefunctions of the ground state and the excited state are expressed as

$$|^2\Pi_\Omega; J\,\Omega\,M_J\,I\,F\,M_F\rangle = |^2\Pi_\Omega\rangle\,|J\,\Omega\,M_J\,I\,F\,M_F\rangle \tag{6.5}$$

$$|^2\Sigma^+; J\,\Omega\,M_J\,I\,F\,M_F\rangle = |^2\Sigma^+\rangle\,|J\,\Omega\,M_J\,I\,F\,M_F\rangle\,, \tag{6.6}$$

respectively. Note that the vibrational quantum number v is dropped. The electric and magnetic dipole moments are calculated in this new basis set:

$$\langle^2\Sigma^+; J'\,\Omega'\,M'_J\,I'\,F'\,M'_F|\,\mu^{\mathrm{sf}}_{\mathrm{el/mag},m}\,|^2\Pi_\Omega; J\,\Omega\,M_J\,I\,F\,M_F\rangle\,. \tag{6.7}$$

To perform this calculation some relations are needed to simplify the analysis.

Using the relation found in [95] for the coupling of two component states one can write

$$|J\,\Omega\,M_J\,I\,F\,M_F\rangle = \sum_{M_I,M_J} |J\,\Omega\,M_J\rangle\,|I\,M_I\rangle\,\langle J\,M_J\,I\,M_I|F\,M_F\rangle\,. \tag{6.8}$$

M_I is the projection of I on the external quantization axis. $\langle J\, M_J\, I\, M_I | F\, M_F\rangle$ is a Clebsch-Gordan coefficient. Any Clebsch-Gordan coefficient can be expressed with a Wigner 3-J symbol [95]:

$$\begin{aligned} C^{J_3,M_3}_{J_1,M_1,J_2,M_2} &= \langle J_1\, M_1\, J_2\, M_2 | J_3\, M_3\rangle \\ &= (-1)^{J_1-J_2+M_3}\sqrt{2J_3+1}\begin{pmatrix} J_1 & J_2 & J_3 \\ M_1 & M_2 & M_3\end{pmatrix}. \end{aligned} \tag{6.9}$$

For the rotational part in Equation 6.8, one can write [95]:

$$\langle J'\,\Omega'\,M'_J|\, D^{(1)*}_{mk}(\phi,\theta,0)\,|J\,\Omega\,M_J\rangle = \sqrt{\frac{2J+1}{2J'+1}}C^{J',\Omega'}_{J,\Omega,1,k}C^{J',M'_J}_{J,M_J,1,m}. \tag{6.10}$$

And the last useful relation evaluates the sum of three Clebsch-Gordan coefficients:

$$\begin{aligned} &\sum_{M_J,M'_J,M_I} C^{J',M'_J}_{J,M_J,1,m}C^{F,M_F}_{J,M_J,I,M_I}C^{F',M'_F}_{J',M'_J,I,M_I} \\ &\qquad = \sqrt{(2J'+1)(2F+1)}(-1)^{I+F+J'+1}C^{F',M'_F}_{F,M_F,1,m}\begin{Bmatrix} J & I & F \\ F' & 1 & J'\end{Bmatrix}, \end{aligned} \tag{6.11}$$

with the curly brackets denoting the 6-j symbol. Using Equation 6.8, 6.9, 6.10, and 6.11 one can write:

$$\begin{aligned} &\langle {}^2\Sigma^+; J'\,\Omega'\,M'_J\,I'\,F'\,M'_F|\mu^{\mathrm{sf}}_{\mathrm{el/mag},m}\,|{}^2\Pi_\Omega; J\,\Omega\,M_J\,I\,F\,M_F\rangle \\ &\qquad =\delta_{I',I}(-1)^{I-J+J'+1-\Omega'-M'_F} \\ &\qquad\quad \times \sqrt{(2J+1)(2J'+1)(2F+1)(2F'+1)}\begin{Bmatrix} J & I & F \\ F' & 1 & J'\end{Bmatrix} \\ &\qquad\quad \times \sum_k \mu^{\mathrm{bf}}_{\mathrm{el/mag},k}\begin{pmatrix} J & 1 & J' \\ \Omega & k & -\Omega'\end{pmatrix}\begin{pmatrix} F & 1 & F' \\ M_F & m & -M'_F\end{pmatrix}. \end{aligned} \tag{6.12}$$

Equation 6.12 is valid for both the electric and the magnetic transition dipole moment.

Now similar to the description in Chapter 2.1 the basic wavefunctions of the ground state, Equation 6.5, and the excited state, Equation 6.6, have to be parity adapted and for the ground state the mixing of wavefunctions with different Ω has to be considered. For the parity adaptation of the ground state one can write:

$$\begin{aligned} |{}^2\Pi_{|\Omega|}; F\,M_F; \epsilon = \pm\rangle =& \frac{1}{\sqrt{2}}(|{}^2\Pi_\Omega; J\,\Omega\,M_J\,I\,F\,M_F\rangle \\ & \pm |{}^2\Pi_{-\Omega}; J\,-\Omega\,M_J\,I\,F\,M_F\rangle). \end{aligned} \tag{6.13}$$

Note that in contrast to Chapter 2.1, since only the rotational ground state with $J = 3/2$ is considered, the $\epsilon = +$ corresponds to spectroscopic e parity, while the

− corresponds to spectroscopic f parity and not only to the sign in the linear combination, see Equation 2.14.

Ω is almost a good quantum number, and the state with approximately $\Omega = 3/2$ is the ground state. The latter is denoted by $F_1; {}^2\Pi_{3/2}$, and its wavefunction is given by

$$|X, e/f, \epsilon, F, M_F\rangle = C_1\,|^2\Pi_{1/2}; F\,M_F; \epsilon\rangle + C_2\,|^2\Pi_{3/2}; F\,M_F; \epsilon\rangle\,, \tag{6.14}$$

where C_1 and C_2 are the mixing coefficients of the OH rotational ground state. They are calculated in Equation 2.19 and 2.20 and their values can be found in Table 2.1. Note that Equation 6.14 uses the same nomenclature for the ground state, which was introduced in the description of the experimental setup in Chapter 6.2.

The excited sate in the experiment is of + parity. Moreover, this state has $J = 1/2$ and $I = 1/2$, so that $F = 0, 1$. The corresponding parity adapted wave function is given by

$$\begin{aligned} |A, +, F, M_F\rangle =& \frac{1}{\sqrt{2}}(|^2\Sigma^+; J\,\Omega{=}1/2\,M_J\,I\,F\,M_F\rangle \\ &+ |^2\Sigma^+; J\,\Omega{=}{-1}/2\,M_J\,I\,F\,M_F\rangle). \end{aligned} \tag{6.15}$$

Equation 6.15 also uses the same nomenclature, which was introduced in the description of the experimental setup in Chapter 6.2.

Combining Equation 6.12, 6.13, and 6.13, yields for the transition dipole moment

$$\begin{aligned} &\langle A, +, F', M'_F|\mu^{\mathrm{sf}}_{\mathrm{el/mag},m}\,|X, e/f, \epsilon, F, M_F\rangle = \\ &\qquad \sqrt{(2J+1)(2J'+1)(2F+1)(2F'+1)} \\ &\qquad \times (-1)^{I-J+1-M'_F} \begin{Bmatrix} J & I & F \\ F' & 1 & J' \end{Bmatrix} \begin{pmatrix} F & 1 & F' \\ M_F & m & -M'_F \end{pmatrix} \\ &\qquad \times \sum_{\Omega',\Omega,k} \frac{c_\Omega \epsilon^{\vartheta(\Omega)}}{2} (-1)^{J'-\Omega'} \mu^{\mathrm{bf}}_{\mathrm{el/mag},k} \begin{pmatrix} J & 1 & J' \\ \Omega & k & -\Omega' \end{pmatrix}, \end{aligned} \tag{6.16}$$

where $J = 3/2$, $I = 1/2$, $J' = 1/2$, and $I' = 1/2$. Moreover, $\epsilon = \pm 1$, $\vartheta(x)$ is the step function, and the sum is over $\Omega' \in \{\pm 1/2\}$ and $\Omega \in \{\pm 1/2, \pm 3/2\}$. The factor $\epsilon^{\vartheta(\Omega)}$ contains $\vartheta(-\Omega) = 0$ for $\Omega > 0$ and $\vartheta(-\Omega) = 1$ for $\Omega < 0$. It is present because for $\epsilon = +1$ (e symmetry) Equation 6.13 has a positive combination, while for $\epsilon = -1$ (f symmetry) it has a sign change for negative Ω. The expression in Equation 6.16 is valid for both the magnetic and the electric transition. As follows from Equation 6.2, the two transition dipole moments have a different k dependence, since the magnetic transition dipole moment changes sign when k changes sign, while the electric transition dipole moment does not. As a result, the sum on the right-hand side of Equation 6.16 leads to the correct parity selection rules for the magnetic ($p = + \to +$) and electric dipole transitions ($p = - \to +$).

The theoretical model described so far does not include the magnetic field in the analysis. The Zeeman effect of OH in low magnetic fields is discussed in detail in [217] and [218], the results are summarized here. Similar to the Stark interaction the Zeeman interaction adds an additional Zeeman term to the Hamiltonian.

$$\boldsymbol{H}_\mathrm{Z} = \mu_0(\boldsymbol{L} + g_S\boldsymbol{S} + g_I\boldsymbol{I} + g_N\boldsymbol{N}) \cdot \boldsymbol{B} \tag{6.17}$$

The numerical values are $g_S = 2.0023192$, $g_I = -3.042 \cdot 10^{-3}$ $g_N = -5.42 \cdot 10^{-4}$ [217]. For the OH radical, the rotational spacing is relatively large compared to the Zeeman energy, and therefore the coupling between states with $J = J' + 1$ is relatively weak. At small magnetic field strengths, like the ones used in this experiment, the mixing between different rotational states is therefore neglected. Thus, for the excited state $A\,^2\Sigma^+$ the influence of the magnetic field is neglected. In the electronic ground state $X\,^2\Pi$, the Zeeman interaction mixes levels with different parity, hence there are also non zero matrix elements between two different Λ doublets. But they will only give a small contribution in second order perturbation calculation, because of the small magnetic fields. Therefore in the present experiment the analysis is limited to wave functions of the ground state $X\,^2\Pi_{3/2}, v = 0, J = 3/2$ belonging to the same Λ doublet.

The matrix elements for the basic wave functions $|X, e/f, \epsilon, F, M_F\rangle$ are then given by:

$$\begin{aligned}
&\langle X, e/f, \epsilon, F', M_F'|\boldsymbol{H}_\mathrm{Z}\,|X, e/f, \epsilon, F, M_F\rangle \\
&\qquad= \mu_0 B g_J^\epsilon (-1)^{J+I-M_F+1}\sqrt{(2F+1)(2F'+1)(2J+1)(J+1)J} \\
&\qquad\quad \cdot \begin{pmatrix} F & 1 & F' \\ -M_F & 0 & M_F' \end{pmatrix} \begin{Bmatrix} F & 1 & F' \\ J & I & J \end{Bmatrix} \\
&\qquad\quad + \mu_0 B g_I (-1)^{J+I-M_F+1}\sqrt{(2F+1)(2F'+1)I(I+1)(2I+1)} \\
&\qquad\quad \cdot \begin{pmatrix} F & 1 & F' \\ -M_F & 0 & M_F' \end{pmatrix} \begin{Bmatrix} F & 1 & F' \\ I & J & I \end{Bmatrix},
\end{aligned} \tag{6.18}$$

with I being the quantum number for the total nuclear spin. The g factors are $g_{3/2}^+ = 0.93507$, $g_{3/2}^- = 0.93644$ and $g_I = -3.042 \cdot 10^{-3}$ [217]. Matrix elements $\langle X, e, -, F, M_F|\,\boldsymbol{H}_\mathrm{Z}\,|X, f, +, F, M_F\rangle$ and $\langle X, f, +, F, M_F|\,\boldsymbol{H}_\mathrm{Z}\,|X, e, -, F, M_F\rangle$ are zero. By evaluating the 3-J symbol in Equation 6.18, it can be seen that only levels with $M_F = M_F'$ are mixing.

Equation 6.18 leads to a new set of eigenstates:

$$|\Psi, e/f, \epsilon, F = 2, M_F = 2\rangle = |X, e/f, \epsilon, F = 2, M_F = 2\rangle \tag{6.19}$$

$$\begin{aligned}|\Psi, e/f, \epsilon, F = 2, M_F \neq 2\rangle &= -c_{1,M_F}^\epsilon\,|X, e/f, \epsilon, F = 2, M_F\rangle \\ &\quad + c_{2,M_F}^\epsilon\,|X, e/f, \epsilon, F = 1, M_F\rangle\end{aligned} \tag{6.20}$$

$$\begin{aligned}|\Psi, e/f, \epsilon, F = 1, M_F \neq 2\rangle &= c_{2,M_F}^\epsilon\,|X, e/f, \epsilon, F = 2, M_F\rangle \\ &\quad + c_{1,M_F}^\epsilon\,|X, e/f, \epsilon, F = 1, M_F\rangle\end{aligned} \tag{6.21}$$

$$|\Psi, e/f, \epsilon, F = 2, M_F = -2\rangle = |X, e/f, \epsilon, F = 2, M_F = -2\rangle \tag{6.22}$$

f symmetry		e symmetry	
$c^+_{1,1}$	0.9999566	$c^-_{1,1}$	0.9999565
$c^+_{2,1}$	0.0093204	$c^-_{2,1}$	0.0093269
$c^+_{1,0}$	0.9999433	$c^-_{1,0}$	0.9999432
$c^+_{2,0}$	0.0106465	$c^-_{2,0}$	0.0106538
$c^+_{1,-1}$	0.9999584	$c^-_{1,-1}$	0.9999583
$c^+_{2,-1}$	0.0091228	$c^-_{2,-1}$	0.0091290

Table 6.2: Coefficients of the new eigenstates $|\Psi, e/f, \epsilon, F, M_F\rangle$ of the OH ground state $X\,^2\Pi_{3/2}, v = 0, J = 3/2$, which include the mixing of levels with different F, caused by the Zeeman interaction with an external magnetic field.

Note that the labelling of the new eigenstates is the same as for the unperturbed sates since F and M_F are nearly good quantum numbers. The mixing coefficients c^ϵ_{1,M_F} and c^ϵ_{2,M_F} depend on the magnetic field strength. In the experiment fields of ≈ 0.9 Gs are used, which is approximately twice as large as the component perpendicular to the Earth's surface of the Earth's magnetic field in Berlin, where the experiment takes place. In the experiment this is the z-component, see Figure 6.1. The mixing coefficients for 0.9 Gs are given in Table 6.2. It can be seen, that the mixing between levels with different F is extremely small for all states and can therefore be neglected.

6.5 Comparison between theory and experiment

In the experiment three different cases for the electric dipole transition are prepared. They are characterized by the three different M_F states of the $X\,^2\Pi_{3/2}, J = 3/2, v = 0, e, F = 1$ state after the microwave transition. The electric dipole transition strength to the $A\,^2\Sigma^+, J = 1/2, v = 1$ state is determined experimentally for these three cases separately. By the symmetry of the experiment, case 2 with $M_F = 1$ and case 3 with $M_F = -1$ are equivalent. Moreover, since the experimental results are in arbitrary units, only a single ratio of the two inequivalent electric dipole intensities can be compared with theory. Since the electric field of the laser is in the space-fixed z direction, it couples to the z component of the space-fixed transition dipole moment, so that $m = 0$. From Equation 6.16, the two inequivalent cases only differ in the value of the conserved M_F and the final angular momentum F', where only $F' = 0$ gives a nonzero contribution for case 1 and only $F' = 1$ for case 2 (and 3). The part of Equation 6.16, that depends on F', M_F, and M'_F is given by

$$\xi(\text{case}) = \sqrt{2F'+1}(-1)^{-M'_F} \begin{Bmatrix} J & I & F \\ F' & 1 & J' \end{Bmatrix} \begin{pmatrix} F & 1 & F' \\ M_F & m & -M'_F \end{pmatrix}, \qquad (6.23)$$

where $J = 3/2$, $J' = 1/2$, $I = 1/2$, $F = 1$ and $m = 0$ for the electric dipole transition. Case 1 has $F' = 0$ and $M_F = M'_F = 0$, while case 2 (3) has $F' = 1$ and $M_F = M'_F = 1(-1)$. As a result, the ratio between the two electric dipole transition strengths is the ratio of the squares of the two transition dipole moments, resulting in

$$\text{signal ratio} = \frac{\xi(\text{case 1})^2}{\xi(\text{case 2})^2} = \frac{\xi(\text{case 1})^2}{\xi(\text{case 3})^2} = 4. \tag{6.24}$$

This is because all other terms of Equation 6.16 drop out of the ratio. Also other quantities as the laser intensity and the molecular density drop out of the ratio because they are assumed to be kept constant for the two experimental cases. The analytic result of Equation 6.24 is confirmed experimentally, see Figure 6.3.

Next, the ratio between the electric and the magnetic dipole transition intensity is calculated. The initial state for the magnetic dipole transitions is the same for the three experimental cases. Namely, it is given by a statistical mixture of $X\,^2\Pi_{3/2}, J = 3/2, v = 0, f, F = 2, M_F$ states, of which four levels ($M_F = \pm 1, \pm 2$) are occupied by 20% of the molecules and one level ($M_F = 0$) is occupied by 19.5%. For the EDA transition the line strength S^{el} is defined for case 1 via:

$$S^{\text{el}} = \quad 0.005 |\langle ^2\Sigma^+; F'\!=\!0\, M'_F\!=\!0; +|\mu^{\text{sf}}_{\text{el},0}|F_1; {}^2\Pi_{3/2}; F\!=\!1\, M_F\!=\!0; +\rangle|^2, \tag{6.25}$$

where the factor of 0.005 represents the 0.5 % population of the initial level and we have $\epsilon = +$ (e symmetry or $-$ parity) for the initial state. Since the magnetic field of the laser points in the x direction of the laboratory frame, the line strength for the MDA transition is defined via

$$\begin{aligned} S^{\text{mag}} &= \frac{\alpha^2}{2} \sum_{M_F} P(M_F) \\ &\times \sum_{M'_F} |\,\langle ^2\Sigma^+; F'\!=\!1\, M'_F; +|\,(\mu^{\text{sf}}_{\text{mag},1} - \mu^{\text{sf}}_{\text{mag},-1})\,|F_1; {}^2\Pi_{3/2}; F\!=\!2\, M_F; -\rangle\,|^2, \end{aligned} \tag{6.26}$$

where $P(M_F)$ accounts for the fraction of molecules in each initial state, so that $P(M_F) = 0.2$ for $M_F = \pm 1, \pm 2$ and $P(0) = 0.195$, and $\epsilon = -$ (f symmetry or $+$ parity) for the initial state. Here, $\alpha = 1/137.036$ is the fine-structure constant, which is included to account for the relative strength of the magnetic field of the laser compared to the electric field.

Using Eqaution 6.25 and 6.26, the ratio between the electric and the magnetic dipole moment for case 1 is calculated:

$$\text{signal ratio} = \frac{S^{\text{el}}}{S^{\text{mag}}} = 25.8. \tag{6.27}$$

In the present theoretical treatment several approximations are made for the calculation of the transition dipole moments with the MOLPRO program package [215]. The details of these approximations are given in the supplementary material to [114]. The errors caused by these approximations is estimated to be an uncertainty of about 10% for the ratio of the squared transition dipole moments. This is to be compared with the experimental measured ratio of 18 ± 8.

The above measured result depends on the fraction of molecules in each of the prepared quantum states. If the two ground states (e and f) have an equal number of molecules before the dipole transitions and if spatial orientation plays no role (for example in the case of an unpolarized laser, or with all M_F states equally populated), then the signal ratio would have been simply given by

$$k = \frac{1}{\alpha^2} \frac{|\langle \mu_{\mathrm{el}} \rangle|^2}{|\langle \mu_{\mathrm{mag}} |\rangle^2} = 2576, \tag{6.28}$$

which therefore represents most directly the relative importance of EDA and MDA transitions from the $X\,^2\Pi_{3/2}, v = 0$ state to the $A\,^2\Sigma^+, v = 1$ state. This value of k has been used in Chapter 5 for the determination of absolute cross section in the collision experiment of OH-NO.

In the experiment no electric quadrupole allowed (EQA) transitions are observed. Calculations of the transition quadrupole moment with MOLPRO [215], give the result, that the EQA transitions are about 100 times weaker than the MDA transitions, which is consistent with the experimental findings.

6.6 Conclusion

In this Chapter the direct measurement of magnetic dipole transitions in laser excitation spectra of the OH $A\,^2\Sigma^+, v = 1 \leftarrow X\,^2\Pi_{3/2}, v = 0$ band is reported. These satellite transitions appear only three orders of magnitude weaker than the corresponding main electric dipole transitions, and can potentially lead to a misinterpretation of detector signals when the Λ-doublet-resolved state populations in OH ($X\,^2\Pi$) are measured. This finding may seem of limited significance in some experiments; in experiments in which large differences in Λ-doublet populations are expected it may be essential. In particular in state-of-the-art molecular beam experiments with unprecedented state purity and precision, magnetic dipole transitions should be carefully considered. One example of such experiment is reported in Chapter 5. The importance of spectroscopically resolving the EDA and MDA transitions with a narrow bandwidth laser is discussed in detail in Chapter 5.3 and [207]. In addition the value k, which is the ratio of the EDA and MDA transitions is used to evaluate absolute cross sections.

Chapter 7

Stark deceleration of NO radicals

In this Chapter the Stark deceleration of NO radicals is reported, despite the small NO dipole moment of only 0.159 Debye. The NO radicals are pumped from the lower Λ-doublet of the electronic ground state $(X\,^2\Pi_{1/2}, v = 0, J = 1/2, e)$ to the lowest rotational state $(X\,^2\Pi_{3/2}, J = 3/2)$ of the other spin-orbit manifold, increasing the Stark shift by a factor 1.8. With the increased resulting force, up to 50% of the kinetic energy is removed.

Based on:
Stark deceleration of NO molecular beam,
X. Wang, M. Kirste, G. Meijer, and S. Y. T. van de Meerakker, Z. Phys. Chem., unpublished manuscript.

7.1 Introduction

The combination of the techniques of Stark-deceleration and cross beam scattering is still at its beginning. To date, only the OH and the ND_3 molecules have been studied in such experiments using a Stark-decelerator. Hence, the realization of a collision experiment with another polar molecule is desirable. To date, Stark deceleration of CO, H_2CO, LiH, NH, ND_3, NH_3, OH, OD, SO_2, YbF, CaF and benzonitrile has been experimentally demonstrated. In principle any of these molecules is suited for collision experiments. One particularly interesting molecule for collision studies has not been decelerated yet. It is the NO radical, which has been discussed extensively in this work.

As it is mentioned in the introduction and in Chapter 4 the NO radical is one of the key molecules in cross beam collision studies [39]. The study of NO radical interaction with rare-gas atoms [47, 48] and surfaces [169, 219] has significantly improved our understanding of interaction dynamics and reaction dynamics. In addition NO, as an open-shell radical, plays an important role in chemical engineering.

In ordinary molecular beam experiments, NO beams are routinely produced in a supersonic expansion, where the NO is seeded in an inert carrier gas. In cooled beam sources and using Xe as the carrier gas, a NO beam velocity of approximately 280 m/s is reached, see Chapter 4. It is experimentally very challenging to reach lower velocities without the formation of NO clusters.

Due to the small NO dipole moment of only 0.159 Debye, Stark deceleration of the NO ground state $(X\,^2\Pi_{1/2}, v = 0, J = 1/2)$ has not been accomplished to date. The force on the molecules per stage is too weak to efficiently decelerate NO. In this work, a different approach is used, in which molecules are pumped from the lower Λ-doublet of the electronic ground state $(X\,^2\Pi_{1/2}, v = 0, J = 1/2, e)$ to the lowest rotational state of the other spin-orbit manifold $(X\,^2\Pi_{3/2}, J = 3/2)$. This state has a factor 1.8 larger Stark shift, see Figure 7.1. With the increased resulting force it is possible to also decelerate the important NO radical.

7.2 Experiment

The molecular beam of NO radicals is produced in a supersonic expansion, by seeding 20% NO in Xe using a backing pressure of 3 bar. The nozzle is cooled to -70°C, resulting in an average velocity of approximately 315 m/s. The NO molecules reside in the rotational levels $(X\,^2\Pi, v = 0, J, e/f)$ of the electronic ground state, hereafter called $(F_1, J, e/f)$ and $(F_2, J, e/f)$, depending on the spin-orbit manifold. The molecules in the $(F_1, J = 1/2, e)$ state are excited, just after the supersonic expansion, via the $A\,^2\Sigma^+ \leftarrow X\,^2\Pi$, R_{11} and Q_{21} transition, to the first electronically excited state $(A\,^2\Sigma^+, v = 0, N = 1)$, using a pulsed dye laser (PDL) at 226.2 nm. The laser is aligned perpendicular to the molecular beam. For the labeling of the NO transition see Equation 2.38 and Figure 2.3. Spontaneous decay from the $(A\,^2\Sigma^+, v = 0, N = 1)$ state, via the R_{22}, Q_{12}, and

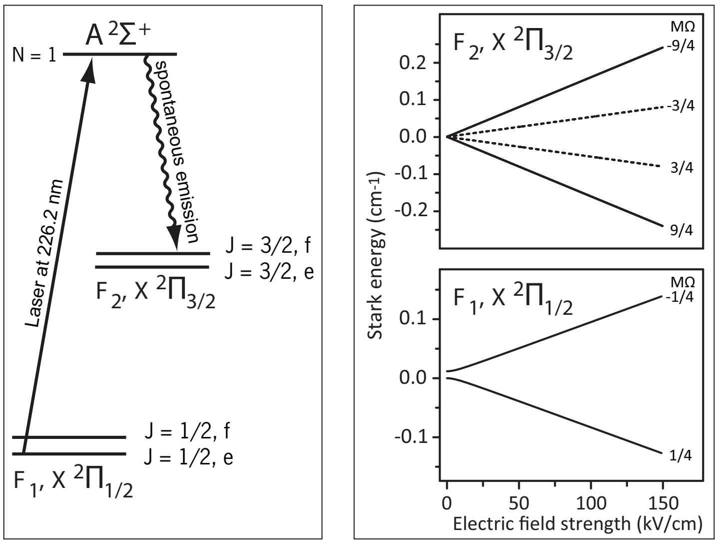

Figure 7.1: Left: Franck-Condon pumping of NO $(F_1, J = 1/2, e)$ molecules to the other spin-orbit manifold $(F_2, J = 3/2, f)$. Right: Comparison of the Stark shift of the ground state $(F_1, J = 1/2, f)$ and the state $(F_2, J = 3/2, f)$, which is produced by the Franck-Condon pumping.

P_{22} transition, populates the $(F_2, J = 3/2, f)$ state, which is not populated after the supersonic expansion. The fluorescence from the $(A\,^2\Sigma^+, v = 0, N = 1)$ state to all final states, is measured with a photomultiplier tube (PMT), mounted above the source chamber.

After passing a 2-mm diameter skimmer the NO radicals enter the 2.6 m long Stark decelerator, which is described in Chapter 2.5, Chapter 3, Chapter 5, and Chapter 6. The $(F_2, J = 3/2, f)$ NO molecules are guided, which corresponds to phase angle $\phi_0 = 0$, and decelerated, using $\phi_0 = 30°$, $\phi_0 = 55°$, and $\phi_0 = 80°$, see Chapter 2.5. For guiding both the $s = 1$ and the $s = 3$ deceleration schemes are used.

The NO $(F_2, J = 3/2, f)$ state consist of two equally populated levels with $(M\Omega = \pm 9/4)$ and $(M\Omega = \pm 3/4)$. Since the Stark shift of $(M\Omega = \pm 9/4)$ is larger, see Figure 7.1, the deceleration of the $(M\Omega = -9/4)$ level is more efficient, than of the $(M\Omega = -3/4)$ level. A larger Stark shift keeps the NO molecules longitudinal and transversal closer together, see Chapter 2.5. Hence, in order to decelerate large number of molecules, the deceleration sequence is calculated for the $(M\Omega = -9/4)$ level.

Behind the Stark decelerator the NO molecules in the $(F_2, J = 3/2, f)$ state are detected via the $A\,^2\Sigma^+ \leftarrow X\,^2\Pi$, Q_{11} and P_{22} transition, using a second PDL at 226.9 nm. The fluorescence is imaged into a second PMT, mounted above the end of the Stark decelerator. Note, that without an external electric field the $(M\Omega = -9/4)$ and the $(M\Omega = -3/4)$ levels are degenerate and therefore these two levels experience a different force in the decelerator, but are not detected differently.

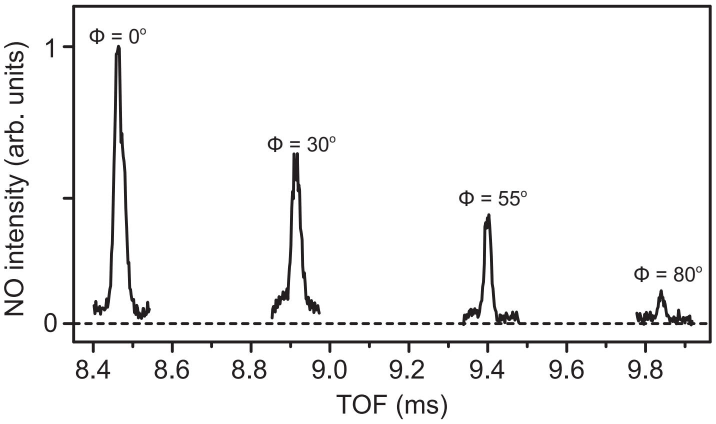

Figure 7.2: Time-of-flight (TOF) profiles of $(F_2, J = 3/2, f)$ NO molecules detected behind the Stark decelerator. The measurements are performed in a $s = 1$ operation mode with a phase angle of $\phi_0 = 0$, $\phi_0 = 30°$, $\phi_0 = 55°$, and $\phi_0 = 80°$, which corresponds to the velocities 315 m/s, 284 m/s, 254 m/s and 229 m/s, respectively. The initial mean velocity of the molecular beam is 315 m/s.

7.3 Results

The time-of-flight (TOF) profiles of $(F_2, J = 3/2, f)$ NO molecules are shown in Figure 7.2. The measurements are performed in a $s = 1$ operation mode with a phase angle of $\phi_0 = 0°$, $\phi_0 = 30°$, $\phi_0 = 55°$, and $\phi_0 = 80°$, which corresponds to the final velocities 315 m/s, 284 m/s, 254 m/s and 229 m/s, respectively. 47% of the kinetic energy is removed at the largest phase angle $\phi_0 = 80°$. The signal is reduced from guiding at $\phi_0 = 0°$, to the maximum deceleration at $\phi_0 = 80°$ by approximately a factor 8.5. This is expected in the Stark deceleration process, since lager phase angles cause smaller phase space acceptances, see Chapter 2.5. The velocity spread of the decelerated packages is 5.5 m/s, 4.5 m/s, 3.5 m/s and 2.0 m/s (FWHM) for the phase angles 0°, 30°, 55°, and 80°, respectively.

The TOF measurements are repeated on a longer time scale for $\phi_0 = 0°$ in $s = 3$ operation mode and for $\phi_0 = 0°$ and $\phi_0 = 55°$ in $s = 1$ operation mode, see Figure 7.3 (a), (b), and (c), respectively. The measurements are reproduced by Monte-Carlo trajectory simulations of the Stark deceleration process. The simulations are done for the $(M\Omega = -9/4)$ and the $(M\Omega = -3/4)$ levels and the outcome is summed. These simulations are in good agreement with the measured TOF. From Figure 7.3 (a) and (b), it is seen that the guided peak at approximately 8.5 ms lies within the much broader undecelerated pulse of NO $(F_2, J = 3/2, f)$ molecules. The undecelerated part exhibits a unique structure which is caused by the switching of the decelerator [72, 73, 74, 75, 76, 77]. For the $s = 3$ deceleration mode in (a) the signal is approximately a factor two larger than for the $s = 1$ deceleration mode in (b). This is also expected, see [83] and Chapter 2.5. In (c) the decelerated part is clearly observed at approximately 9.4 ms, but also for this

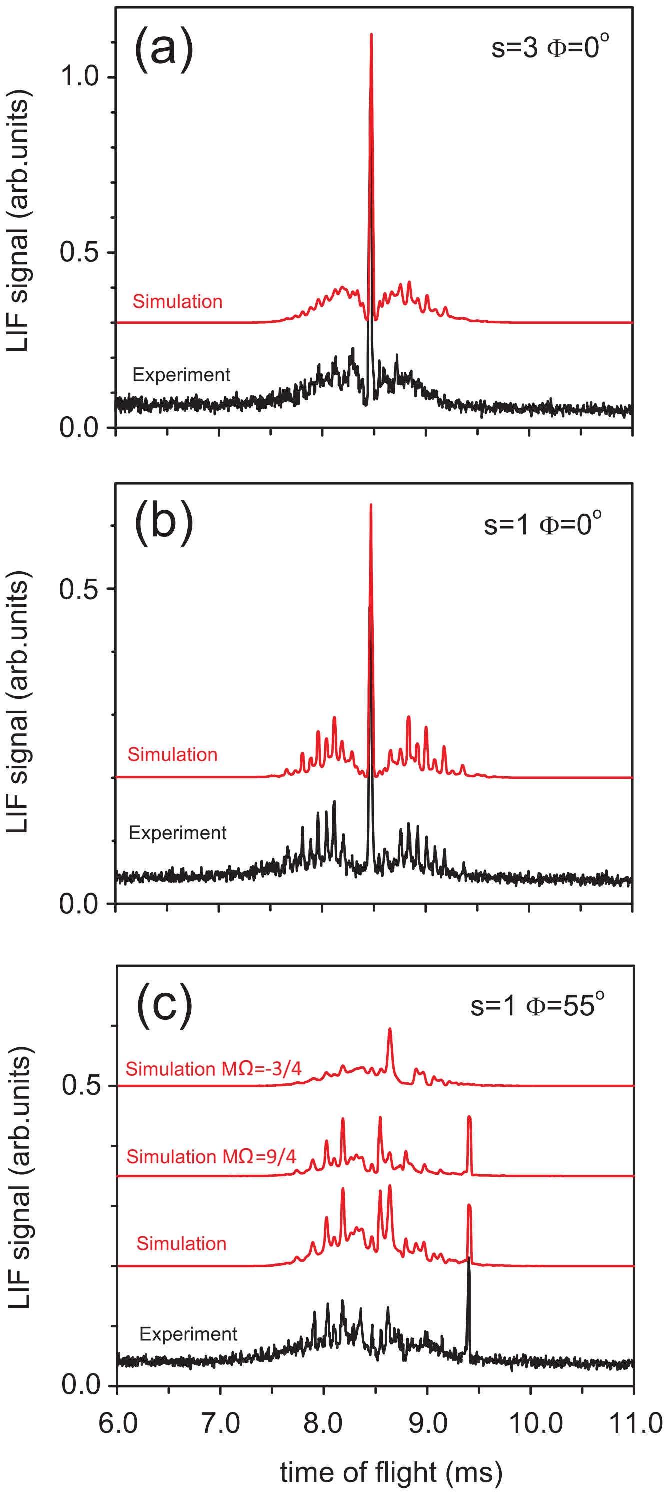

Figure 7.3: Time-of-flight (TOF) profiles of $(F_2, J = 3/2, f)$ NO molecules detected behind the Stark decelerator. The measurements are performed in (a) for $\phi_0 = 0^\circ$ in $s = 3$ operation mode, for (b) in $\phi_0 = 0^\circ$ in $s = 1$ operation mode and for (c) in $\phi_0 = 55^\circ$ in $s = 1$ operation mode. The measurements are reproduced by Monte-Carlo trajectory simulations of the Stark deceleration process.

measurement with $\phi_0 = 55°$, the decelerated part is not yet fully separated from the undecelerated part. Only for phase angles above 80° the decelerated part is fully isolated from the undecelerated beam.

If the decelerated NO molecules are to be used in a collision experiment, the state purity of the decelerated beam is an important issue. The high-field seeking molecules are defocused by the electric fields in the decelerator, i.e. high-field seeking states are not populated behind the decelerator. All low-field seeking states, which are populated after the supersonic expansion, are diluted in the deceleration process. Nevertheless they are still populated. Especially the NO ground state $(F_1, J = 1/2, f)$ is strongly populated after the supersonic expansion. The small dipole moment of the NO molecules is sufficient to keep the molecules within the decelerator, but it is insufficient to lead to unstable trajectories, due to unmatched phase angles [72, 73, 74, 75, 76, 77]. Hence the $(F_1, J = 1/2, f)$ state is guided by the decelerator. Figure 7.4 shows a comparison of the $(F_1, J = 1/2, f)$ state to the $(F_2, J = 3/2, f)$ state. Both measurements are performed with the same decelerator setting, $s = 1$, $\phi_0 = 0°$. The signal intensities are not comparable, because the measurements are done with different settings of the PMT, but it is obvious that the $(F_1, J = 1/2, f)$ state is much more intense. All other rotational states are populated less, due to their smaller Stark shift and due to their smaller initial population. The TOF profile of the $(F_1, J = 1/2, f)$ state is much broader than the profile of the $(F_2, J = 3/2, f)$ state. Thus, the decelerated $(F_2, J = 3/2, f)$ molecules are never detected without a residual population in at least one other rotational level.

If the decelerated NO molecules are to be used in a collision experiment, the state purity of the decelerated beam is not sufficient in the current setup. Also is the intensity of $(F_2, J = 3/2, f)$ molecules presumably too small for most collision experiments. The state purity could be improved to perfect state-selection, for instance by using a hexapole, like it was described in Chapter 4, in front of the decelerator. The intensity could be much improved by replacing the current Franck-Condon pumping scheme with a more efficient scheme like stimulated emission pumping or stimulated Raman adiabatic passage (STIRAP). The population in the $(F_2, J = 3/2, f)$ state could also be increased, when the molecules are directly pumped from the $(F_1, J = 1/2, f)$ state, using a light source like for instance a free electron laser.

Instead of a Stark decelerator a Zeeman decelerator can also be used to decelerate NO, using the Zeeman interaction of the molecules in an inhomogeneous magnetic field [220]. Since the $(F_1, J = 1/2)$ state has in first order no magnetic moment, also in a Zeeman deceleration experiment the NO molecules need to be pumped to the $(F_2, J = 3/2)$ state, which yields a magnetic moment of 1.2 Bohr magneton. In contrast to the Stark decelerator the Zeeman decelerator decelerates NO radicals in the e state. Thus, also in a Zeeman decelerator, all discussed issues about the population intensity remain. The specialty of Zeeman deceleration of NO, which is the lacking magnetic moment of both Λ-doublet components of the ground state $(F_1, J = 1/2, e/f)$, can be an advantage or dis-

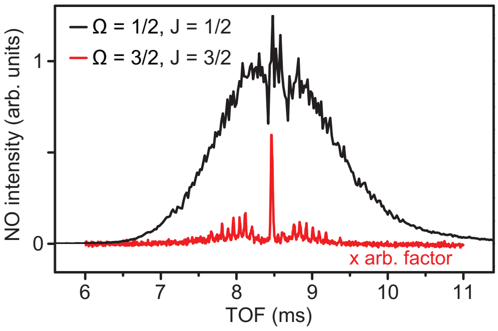

Figure 7.4: Comparison of the $(F_1, J = 1/2, f)$ state (red) to the $(F_2, J = 3/2, f)$ state (black). Both measurements are performed with the same decelerator setting, $s = 1$, $\phi_0 = 0°$.

advantage. It is only an advantage if the Zeeman decelerator is long enough to strongly dilute the $(F_1, J = 1/2, e/f)$ population in the molecular beam compared to the $(F_2, J = 3/2, e)$ population. If the Zeeman decelerator is too short, then the residual $(F_1, J = 1/2, e/f)$ population might be a serious impediment for a useful application of Zeeman decelerated NO molecules, since the magnetic field can never influence the $(F_1, J = 1/2, e/f)$ state.

7.4 Conclusion

In this last experiment of my thesis the NO molecule is decelerated for the first time. Up to 50% of the kinetic energy is removed in the deceleration process. In order to do so, the molecules are pumped to the $(F_2, J = 3/2, f)$ state, by Franck-Condon pumping. The measured TOF profiles show good agreement with the outcome of Monte-Carlo trajectory simulations. The experimental findings, reported here, establish the NO molecule within the family of decelerated molecules and more interesting experiments with decelerated NO molecules are to be expected after this first proof of principle experiment.

Summary and outlook

In this thesis the technique of Stark deceleration is combined with the mature technique of crossed molecular beam scattering. Collision of Stark-decelerated OH ($X\,^2\Pi_{3/2}, v = 0, J = 3/2, f$) radicals with He atoms and D_2 molecules are studied. The measured state-to-state cross sections are in good agreement with the inelastic scattering cross sections determined from quantum close-coupled scattering calculations based on high-quality ab initio OH-He PES's.

A hexapole was designed with an innovative geometry. The hexapole geometry is obtained without the need for ceramic suspensions that connect two neighboring hexapole rods, which are on different polarities. Hence, the pathway for a discharge over the insulating suspension is largely increased, while in the meantime the six hexapole rods are brought close to each other. The hexapole focuses and state-selects NO radicals with a state purity of 99% in the upper Λ-doublet of the electronic ground state ($X\,^2\Pi_{1/2}, v = 0, J = 1/2, f$) after only 30 cm. Thus far hexapoles of several meters in length have been used to focus NO molecules.

Extending the level of control in crossed molecular beam scattering experiments was the main goal of this thesis. This goal has been fulfilled to a large extent in the OH-NO collision experiment. In this experiment the inelastic scattering between Stark-decelerated OH ($X\,^2\Pi_{3/2}, v = 0, J = 3/2, f$) and hexapole-selected NO ($X\,^2\Pi_{1/2}, v = 0, J = 1/2, f$) radicals was reported. The Stark-decelerator allowed for an energy resolved study of this bi-molecular scattering. The energy was varied between 70 und 300 cm^{-1}, by scanning the OH velocity. An energy resolution of 20 cm^{-1} (FWHM) was achieved. In addition, the state-selective abilities of the Stark-decelerator and the hexapole and the state-specific LIF detection method, allowed the scattering study to be quantum-state resolved. It was possible to measure the threshold behavior of four rotationally excited OH scattering channels. The determination of absolute cross sections is in general difficult in conventional crossed molecular beam scattering experiments, since in most cases the density and the spatial spread of one collision partner is unknown. But absolute cross sections are an essential part of the theoretical models in combustion physics, atmospheric science, and astrochemistry. In the OH-NO collision experiment the Stark-decelerated OH beam and the hexapole-selected beam were well characterized by the comparison of time-of-flight measurements with the outcome of Monte-Carlo trajectory simulations. A simulation of the spatial overlap of the two beams and the measurement of the absolute number of molecules allowed for the determination of absolute cross sections.

The background-free detection was of vital importance for the success of the ON-NO collision experiment. The analysis of the background signal in the OH ($X\,^2\Pi_{3/2}, v = 0, J = 3/2, e$) state brought a surprising result. The magnetic dipole allowed transitions in the well characterized $A\,^2\Sigma^+ \leftarrow X\,^2\Pi$ system are two orders of magnitude larger than generally believed. In a follow-up experiment the ratio between electric dipole allowed and magnetic dipole allowed transitions was compared for the important OH radical. In prospective experiments on OH, in which large differences in Λ-doublet populations are expected, the magnetic dipole transition may be essential.

The last experiment, reported in this thesis, was the first deceleration of the important NO radical, removing up to 50% of the kinetic energy. For this purpose the NO radicals were pumped from the lower Λ-doublet of the electronic ground state ($X\,^2\Pi_{1/2}, v = 0, J = 1/2, e$) to the lowest rotational state ($X\,^2\Pi_{3/2}, J = 3/2$) of the other spin-orbit manifold.

The combination of the techniques of Stark-deceleration and cross beam scattering is still at its infancy. To date, only the OH molecule has been studied in such experiments using a Stark-decelerator. Hence, the realization of a collision experiment with another polar molecule is desirable. To date, Stark deceleration of CO, H_2CO, LiH, NH, ND_3, NH_3, OH, OD, SO_2, YbF, CaF and benzonitrile has been experimentally demonstrated. In principle any of these molecules is suited for collision experiments and surely a vast number of interesting collision experiments using Stark decelerated beams is yet to come. OH-He is a well-suited system to improve the energy resolution in the scattering process, since scattering resonances are believed to be pronounced in this system. By reducing the angle between the two beams the energy resolution can significantly be improved. Currently, an experiment on the scattering of OH-He with improved energy resolution is performed at the Fritz-Haber-Institute in Berlin.

A new approach, to measure scattering resonances in crossed-beam collision studies, using Stark-decelerators, is the measurement of the differential cross section, using a velocity-map-ion-imaging detector. The narrow velocity spread of Stark-decelerated beams is expected to result in sharper scattering images, revealing the detailed structure in the differential cross section.

Another application of the combination of Stark deceleration and velocity-map-ion-imaging is the measurement of product pair correlations in bi-molecular scattering. The ion image contains information of the product state distributions of both collision partners. With the excellent velocity resolution of a Stark decelerator this information is expected to be revealed in the images. The combination of Stark deceleration and velocity-map-ion-imaging is currently, followed by the group of Van de Meerakker at the Radboud University in Nijmegen.

The combination of two Stark-decelerators is another promising approach. This would enable the study of bi-molecular collisions at collision energies in the $1 - 500$ cm^{-1} range and with an energy resolution of a fraction of a wavenumber. This offers unique prospects for the study of threshold phenomena with improved energy resolution, for the observation of shape and Feshbach resonances that are predicted to occur at low collision energies and around energetic thresholds, and for controlling dipole-dipole interactions in cold molecular collisions with external electric or magnetic fields. The NO radical is a particularly interesting candidate for these experiments, using either Stark or Zeeman deceleration for the manipulation of its internal energy.

Closing remark

Referring to the anecdote from the introduction, the Stark decelerator is one of the tools we can use to study collision processes. It is a very powerful tool and it will hopefully stimulate the well established field of cross molecular beam scattering. This work accomplished for the first time the state-to-state scattering of two radicals. This most important result of my thesis constitutes an important step forward in the quest to study molecular collisions under completely controlled conditions, thereby offering new insights into molecular dynamics.

Bibliography

[1] I. Estermann and S. N. Foner, *History of molecular beam research: Personal reminiscences of the important evolutionary period 1919–1933*, Am. J. Phys. **43**, 661, 1975.

[2] L. Dunoyer, *Sur la théorie cinétique des gaz et la réalisation d'un rayonnement matériel d'origine thermique*, Comptes rendus hebdomadaires des séances de Académie des sciences (France) **152**, 592, 1911.

[3] O. Stern, *Zur Methode der Molekularstrahlen I*, Z. Phys. **39**, 751, 1926.

[4] H. Kallmann and F. Reiche, *Über den Durchgang bewegter Moleküle durch inhomogene Kraftfelder*, Z. Phys. **6**, 352, 1921.

[5] I. Estermann and O. Stern, *Beugung von Molekularstrahlen*, Z. Phys. A **61**, 95, 1930.

[6] F. Knauer, *Über die Streuung von Molekularstrahlen in Gasen. I*, Z. Phys. A **80**, 80, 1933.

[7] L. F. Broadway, *Experiments on molecular scattering in gases. II. The collision of sodium and potassium atoms with mercury*, Proc. R. Soc. London **141**, 634, 1933.

[8] W. H. Mais, *The scattering of a beam of potassium atoms in various gases*, Phys. Rev. **45**, 773, 1934.

[9] S. Rosin and I. I. Rabi, *Effective collision cross sections of the alkali atoms in various gases*, Phys. Rev. **48**, 373, 1935.

[10] P. Rosenberg, *Collision cross sections of K atoms and* K_2 *molecules in gases*, Phys. Rev. **55**, 1267, 1939.

[11] J. P. Gordon, H. J. Zeiger, and C. H. Townes, *Molecular microwave oscillator and new hyperfine structure in the microwave spectrum of* NH_3, Phys. Rev. **95**, 282, 1954.

[12] J. P. Gordon, H. J. Zeiger, and C. H. Townes, *The Maser - New type of microwave amplifier, frequency standard, and spectrometer*, Phys. Rev. **99**, 1264, 1955.

[13] H. G. Bennewitz, W. Paul, and C. Schlier, *Fokussierung polarer Moleküle*, Z. Phys. **141**, 6, 1955.

[14] K. H. Kramer and R. B. Bernstein, *Focusing and orientation of symmetric-top molecules with the electric six-pole field*, J. Chem. Phys. **42**, 767, 1965.

[15] J. J. T. ter Meulen, W. L. Meerts, G. W. M. van Mierlo, and A. Dymanus, *Observations of population inversion between the Λ-doublet states of OH*, Phys. Rev. Lett. **36**, 1031, 1976.

[16] J. P. Toennies, *General discussion*, Discuss. Faraday Soc. **33**, 96, 1962.

[17] J. P. Toennies, *Molekularstrahlmessungen von Stoßquerschnitten für Übergänge zwischen definierten Rotationszuständen zwei-atomiger Moleküle*, Z. Phys. A **182**, 257, 1965.

[18] H. G. Bennewitz, K. H. Kramer, J. P. Toennies, and W. Paul, *Messung der Anisotropie des van der Waals-Potentials durch Streuung von Molekülen in definiertem Quantenzustand*, Z. Phys. **177**, 84, 1964.

[19] P. R. Brooks and E. M. Jones, *Reactive scattering of K atoms from oriented CH_3I molecules*, J. Chem. Phys. **45**, 3449, 1966.

[20] R. J. Beuhler, R. B. Bernstein, and K. H. Kramer, *Observation of the reactive asymmetry of methyl iodide. Crossed beam study of the reaction of rubidium with oriented methyl iodide molecules*, J. Am. Chem. Soc. **88**, 5331, 1966.

[21] P. R. Brooks, *Reactions of oriented molecules*, Science **193**, 11, 1976.

[22] S. Stolte, J. Reuss, and H. Schwartz, *Orientational anisotropy in the total collision cross section of state-selected NO on CCl_4 using crossed molecular beams*, Physica **57**, 254 , 1972.

[23] S. Stolte, J. Reuss, and H. Schwartz, *Orientational anisotropy in the total collision cross section of state-selected NO molecules*, Physica **66**, 211 , 1973.

[24] H. Moerkerken, M. Prior, and J. Reuss, *Preliminary observations of the orientation dependence of H_2-Ar scattering by a new technique*, Physica **50**, 499 , 1970.

[25] J. J. Everdij, A. Huijser, and N. F. Verster, *Improved space focusing of polar diatomic molecules in a system of quadrupole and hexapole fields*, Rev. Sci. Instrum. **44**, 721, 1973.

[26] D. Auerbach, E. E. A. Bromberg, and L. Wharton, *Alternate-gradient focusing of molecular beams*, J. Chem. Phys. **45**, 2160, 1966.

[27] D. Kakati and D. C. Lainé, *Alternate-gradient focusing of a molecular beam*,

J. Phys. E **4**, 269, 1971.

[28] D. C. Lainé and R. Sweeting, *Crossed-wire focuser for molecular beams*, Phys. Lett. A **34**, 144, 1971.

[29] D. H. H. Al-Amiedy and D. C. Lainé, *Ring-type state-selector and space focuser for molecules with a positive induced dipole moment*, Phys. Lett. A **66**, 94 , 1978.

[30] S. M. Bobbio, C. T. Chiou, E. F. Greene, and H. D. Lambropoulos, *Reduction of the angular divergence of a molecular beam by a coaxial beam of electrons*, J. Chem. Phys. **62**, 190, 1975.

[31] G. Hall, K. Liu, M. J. McAuliffe, C. F. Giese, and W. R. Gentry, *Pulsed molecular beam study of state-to-state vibrational excitation in He+I_2 collisions: Energy dependence of the $v=0 \rightarrow 1$ cross section*, J. Chem. Phys. **78**, 5260, 1983.

[32] L. K. Macdonald, R. G., *State-to-state integral cross sections for the inelastic scattering of CH($X^2\Pi$)+He: Rotational rainbow and orbital alignment*, J. Chem. Phys. **91**, 821, 1989.

[33] H. U. Hostettler and R. B. Bernstein, *Improved slotted disk type velocity selector for molecular beams*, Rev. Sci. Instrum. **31**, 872, 1960.

[34] H. Thuis, S. Stolte, and J. Reuss, *Investigation of the angle dependent part of the intermolecular potential of NO-inert gas systems using crossed molecular beams*, Chem. Phys. **43**, 351 , 1979.

[35] D. H. Parker, H. Jalink, and S. Stolte, *Dynamics of molecular stereochemistry via oriented molecule scattering*, J. Phys. Chem. **91**, 5427, 1987.

[36] D. H. Parker and R. B. Bernstein, *Oriented molecule beams via the electrostatic hexapole - preparation, characterization, and reactive scattering*, Annu. Rev. Phys. Chem. **40**, 561, 1989.

[37] S. Stolte, *Aiming the molecular arrow*, Nature **353**, 391, 1991.

[38] H. Kohguchi and T. Suzuki, *State-to-state rotational inelastic scattering of free radicals*, Annu. Rep. Prog. Chem. **98**, 421, 2002.

[39] M. Brouard and C. Vallance (Editors), *Tutorials in molecular reaction dynamics*, Royal Society of Chemistry, 2010.

[40] A. Gijsbertsen, H. Linnartz, G. Rus, A. E. Wiskerke, S. Stolte, D. W. Chandler, and J. Kłos, *Differential cross sections for collisions of hexapole state-selected NO with He*, J. Chem. Phys. **123**, 224305, 2005.

[41] A. Gijsbertsen, H. Linnartz, and S. Stolte, *Parity-dependent rotational rainbows in D_2-NO and He-NO differential collision cross sections*, J. Chem.

Phys. **125**, 133112, 2006.

[42] J. J. van Leuken, F. H. W. Van Amerom, J. Bulthuis, J. G. Snijders, and S. Stolte, *Parity-resolved rotationally inelastic collisions of hexapole state-selected NO (*$^2\Pi, J = 1/2^-$*) with Ar*, J. Phys. Chem. **99**, 15573, 1995.

[43] K. Schreel and J. J. T. ter Meulen, *Determination of* Λ*-doublet resolved cross-sections for inelastic scattering of OH by para- and normal-*H_2, J. Chem. Phys. **105**, 4552, 1996.

[44] K. Schreel, J. Schleipen, A. Eppink, and J. J. T. ter Meulen, *State-to-state cross sections for rotational excitation of OH by collisions with He and Ar*, J. Chem. Phys. **99**, 8713, 1993.

[45] M. C. van Beek, G. Berden, H. L. Bethlem, and J. J. T. ter Meulen, *Molecular reorientation in collisions of OH+Ar*, Phys. Rev. Lett. **86**, 4001, 2001.

[46] M. C. van Beek, J. J. T. ter Meulen, and M. H. Alexander, *Rotationally inelastic collisions of OH(X* $^2\Pi$*)+Ar. I. State-to-state cross sections*, J. Chem. Phys. **113**, 628, 2000.

[47] C. J. Eyles, M. Brouard, C. H. Yang, J. Klos, F. J. Aoiz, A. Gijsbertsen, A. E. Wiskerke, and S. Stolte, *Interference structures in the differential cross-sections for inelastic scattering of NO by Ar*, Nature Chem. **3**, 597, 2010.

[48] H. Kohguchi, T. Suzuki, and M. H. Alexander, *Fully state-resolved differential cross sections for the inelastic scattering of the open-shell NO molecule by Ar*, Science **294**, 832, 2001.

[49] K. Bergmann, R. Engelhardt, U. Hefter, P. Hering, and J. Witt, *State-resolved differential cross sections for rotational transitions in* Na_2*+Ne (He) collisions*, Phys. Rev. Lett. **40**, 1446, 1978.

[50] T. Schäfer, N. Bartels, N. Hocke, X. Yang, and A. M. Wodtke, *Orienting polar molecules without hexapoles: Optical state-selection with adiabatic orientation*, Chem. Phys. Lett. **535**, 1 , 2012.

[51] D. Matsiev, J. Chen, M. Murphy, and A. M. Wodtke, *Transport and focusing of highly vibrationally excited NO molecules*, J. Chem. Phys. **118**, 9477, 2003.

[52] J. Chen, D. Matsiev, J. D. White, M. Murphy, and A. M. Wodtke, *Hexapole transport and focusing of vibrationally excited NO molecules prepared by optical pumping*, Chem. Phys. **301**, 161 , 2004.

[53] F. Y. Wang, J. S. Lin, and K. Liu, *Steric control of the reaction of CH stretchŰexcited CHD*$_3$ *with chlorine atom*, Science **331**, 900, 2011.

[54] F. Wang, K. Liu, and T. P. Rakitzis, *Revealing the stereospecific chemistry*

of the reaction of Cl with aligned $CHD_3(v_1 = 1)$, Nature Chem. **4**, 636, 2012.

[55] A. Schultz, H. W. Cruse, and R. N. Zare, *Laser Induced Fluorescence: A method to measure the internal state distribution of reaction products*, J. Chem. Phys. **57**, 1354, 1972.

[56] J. L. Kinsey, *Laser Induced Fluorescence*, Ann. Rev. Phys. Chem. **28**, 349, 1977.

[57] D. W. Chandler and P. L. Houston, *Two-dimensional imaging of state-selected photodissociation products detected by multiphoton ionization*, J. Chem. Phys. **87**, 1445, 1987.

[58] D. H. Parker and A. T. J. B. Eppink, *Photoelectron and photofragment velocity map imaging of state-selected molecular oxygen dissociation/ionization dynamics*, J. Chem. Phys. **107**, 2357, 1997.

[59] T. P. Gebhardt, C. R.and Rakitzis, P. C. Samartzis, V. Ladopoulos, and T. N. Kitsopoulos, *Slice imaging: A new approach to ion imaging and velocity mapping*, Rev. Sci. Instrum. **72**, 3848, 2001.

[60] D. Townsend, M. P. Minitti, and A. G. Suits, *Direct current slice imaging*, Rev. Sci. Instrum. **74**, 2530, 2003.

[61] L. Schnieder, K. Seekamp-Rahn, J. Brokowski, E. Wrede, K. H. Welge, F. J. Aoiz, L. Bañares, M. J. D'Mello, V. J. Herrero, V. Sáez Rábanos, and R. E. Wyatt, *Experimental studies and theoretical predictions for the $H + D_2 \rightarrow HD + D$ reaction*, Science **269**, 207, 1995.

[62] L. Schnieder, K. Seekamp-Rahn, E. Wrede, and K. H. Welge, *Experimental determination of quantum state resolved differential cross sections for the hydrogen exchange reaction $H{+}D_2 \rightarrow HD{+}D$*, J. Chem. Phys. **107**, 6175, 1997.

[63] X. Yang, *State-to-state dynamics of elementary chemical reactions using Rydberg H-atom translational spectroscopy*, Int. Rev. Phys. Chem. **24**, 37, 2005.

[64] B. R. Strazisar, C. Lin, and H. F. Davis, *Mode-specific energy disposal in the four-atom reaction $OH + D_2 \rightarrow HOD + D$*, Science **290**, 958, 2000.

[65] L. H. Lai, J. H. Wang, D. C. Che, and K. Liu, *Direct mapping of vibrational-specific angular distributions of the polyatomic reaction product: $CN{+}D_2 \rightarrow DCN{+}D$*, J. Chem. Phys. **105**, 3332, 1996.

[66] D. F. Varley and P. J. Dagdigian, *Product state distributions and angular differential cross sections from photoinitiated reactions of chlorine atoms with small hydrocarbons*, J. Phys. Chem. **99**, 9843, 1995.

[67] S. A. Kandel, P. Rakitzis, T. Lev-on, and R. N. Zare, *Dynamics for the* $Cl+C_2H_6 \rightarrow HCl+C_2H_5$ *reaction examined through state-specific angular distributions*, J. Chem. Phys. **105**, 7550, 1996.

[68] J. J. Lin, J. Zhou, W. Shiu, and K. Liu, *Application of time-sliced ion velocity imaging to crossed molecular beam experiments*, Rev. Sci. Instrum. **74**, 2495, 2003.

[69] R. N. Zare, *Resonances in reaction dynamics*, Science **311**, 1383, 2006.

[70] M. H. Qiu, Z. F. Ren, L. Che, D. X. Dai, S. A. Harich, X. Y. Wang, X. M. Yang, C. X. Xu, D. Q. Xie, M. Gustafsson, R. T. Skodje, Z. G. Sun, and D. H. Zhang, *Observation of Feshbach resonances in the* $F+H_2 \rightarrow HF+H$ *reaction*, Science **311**, 1440, 2006.

[71] X. A. Wang, W. R. Dong, M. H. Qiu, Z. F. Ren, L. Che, D. X. Dai, X. Y. Wang, X. M. Yang, Z. G. Sun, B. N. Fu, S. Y. Lee, X. Xu, and D. H. Zhang, *HF(v' = 3) forward scattering in the* $F + H_2$ *reaction: Shape resonance and slow-down mechanism*, Proc. Natl. Acad. Sci. USA **105**, 6227, 2008.

[72] H. L. Bethlem, G. Berden, and G. Meijer, *Decelerating neutral dipolar molecules*, Phys. Rev. Lett. **83**, 1558, 1999.

[73] H. L. Bethlem, *Deceleration and trapping of polar molecules using time-varying electric fields*, Ph. D. thesis, Radboud Universiteit, Nijmegen, The Netherlands, 2002.

[74] S. Y. T. van de Meerakker, H. L. Bethlem, and G. Meijer, *Taming molecular beams*, Nature Phys. **4**, 595, 2008.

[75] S. Y. T. van de Meerakker, P. H. M. Smeets, N. Vanhaecke, R. T. Jongma, and G. Meijer, *Deceleration and electrostatic trapping of OH radicals*, Phys. Rev. Lett. **94**, 023004, 2005.

[76] S. Y. T. van de Meerakker, *Deceleration and electrostatic trapping of OH radicals*, Ph. D. thesis, Radboud Universiteit, Nijmegen, The Netherlands, 2005.

[77] S. Y. T. van de Meerakker, H. L. Bethlem, N. Vanhaecke, and G. Meijer, *Manipulation and Control of Molecular Beams*, Chem. Rev. **112**, 4828, 2012.

[78] H. L. Bethlem, G. Berden, F. M. H. Crompvoets, R. T. Jongma, A. J. A. van Roij, and G. Meijer, *Electrostatic trapping of ammonia molecules*, Nature **406**, 491, 2000.

[79] S. Y. T. van de Meerakker, N. Vanhaecke, M. P. J. van der Loo, G. C. Groenenboom, and G. Meijer, *Direct measurement of the radiative lifetime of vibrationally excited OH radicals*, Phys. Rev. Lett. **95**, 013003, 2005.

[80] J. J. Gilijamse, S. Hoekstra, S. A. Meek, M. Metsälä, S. Y. T. v. de Meerakker, G. Meijer, and G. C. Groenenboom, *The radiative lifetime of metastable CO ($a^3\Pi$, v=0)*, J. Chem. Phys. **127**, 221102, 2007.

[81] E. R. Hudson, H. J. Lewandowski, B. C. Sawyer, and J. Ye, *Cold molecule spectroscopy for constraining the evolution of the fine structure constant*, Phys. Rev. Lett. **96**, 143004, 2006.

[82] J. J. Gilijamse, S. Hoekstra, S. Y. T. van de Meerakker, G. C. Groenenboom, and G. Meijer, *Near-threshold inelastic collisions using molecular beams with a tunable velocity*, Science **313**, 1617, 2006.

[83] L. Scharfenberg, H. Haak, G. Meijer, and S. Y. T. van de Meerakker, *Operation of a Stark decelerator with optimum acceptance*, Phys. Rev. A **79**, 023410, 2009.

[84] L. Scharfenberg, J. Kłos, P. J. Dagdigian, M. H. Alexander, G. Meijer, and S. Y. T. van de Meerakker, *State-to-state inelastic scattering of Stark-decelerated OH radicals with Ar atoms*, Phys. Chem. Chem. Phys. **12**, 10660, 2010.

[85] B. C. Sawyer, B. K. Stuhl, D. Wang, and J. Yeo, M. Ye, *Molecular Beam Collisions with a Magnetically Trapped Target*, Phys. Rev. Lett. **101**, 203203, 2008.

[86] B. C. Sawyer, B. K. Stuhl, M. Yeo, T. V. Tscherbul, M. T. Hummon, Y. Xia, J. Kłos, D. Patterson, J. M. Doyle, and J. Ye, *Cold heteromolecular dipolar collisions*, Phys. Chem. Chem. Phys. **13**, 19059, 2011.

[87] R. B. Bernstein, *Molecular beam scattering at thermal energies*, Science **144**, 141, 1964.

[88] C. Berteloite, M. Lara, A. Bergeat, S. D. L. Picard, F. Dayou, K. M. Hickson, A. Canosa, C. Naulin, J. M. Launay, I. R. Sims, and P. R. L. M. Costes, *Kinetics and dynamics of the $S(^1D_2)+H_2 \rightarrow SH+H$ reaction at very low temperatures and collision energies*, Phys. Rev. Lett. **105**, 203201, 2010.

[89] G. Paterson, M. K. Costen, and K. G. McKendrick, *Collisional depolarisation of rotational angular momentum: influence of the potential energy surface on the collision dynamics?*, Int. Rev. Phys. Chem. **31**, 69, 2012.

[90] D. C. Clary, *Fast chemical reactions: Theory challenges experiment*, Ann. Rev. Phys. Chem. **41**, 61, 1990.

[91] I. W. M. Smith, *Laboratory astrochemistry: Gas-phase processes*, Annu. Rev. Astron. Astrophys. **49**, 29, 2011.

[92] G. Herzberg, *The spectra and structures of simple free radicals*, Dover Publications, New York, NY, USA, 1971.

[93] J. M. Brown and A. Carrington, *Rotational spectroscopy of diatomic molecules*, Cambridge University Press, 2003.

[94] F. Hund, *Allgemeine Quantenmechanik des Atom- und Molekülbaues. Handbuch der Physik*, volume 24, Berlin, 1933.

[95] R. N. Zare, *Angular momentum*, John Wiley & Sons, New York, NY, USA, 1988.

[96] P. F. Bernath, *Spectra of atoms and molecules*, Oxford university press, New York, NY, USA, 1995.

[97] J. Brown, J. Hougen, K.-P. Huber, J. Johns, I. Kopp, H. Lefebvre-Brion, A. Merer, D. Ramsay, J. Rostas, and R. Zare, *The labeling of parity doublet levels in linear molecules*, J. Mol. Spec. **55**, 500, 1975.

[98] K. F. Freed, *Theory of hyperfine structure of molecules*, J. Chem. Phys. **45**, 4214, 1966.

[99] W. L. Meerts, *On the microwave spectrum of the* $X^2\Pi$ *state of the hydroxyl radical*, Chem. Phys. Lett. **46**, 24, 1977.

[100] C. A. Burrus and W. Gordy, *One-to-two millimeter wave spectroscopy. III. NO and DI*, Phys. Rev. **92**, 1437, 1953.

[101] W. L. Meerts and A. Dymanus, *The hyperfine* Λ*-doubling spectrum of* $^{14}N^{16}O$ *and* $^{15}N^{16}O$, J. Mol. Spec. **44**, 320 , 1972.

[102] G. H. Dieke and J. Crosswhite, *The ultraviolet bands of OH*, J. Quant. Spectrosc. Radiat. Transf. **2**, 97, 1962.

[103] J. J. T. ter Meulen, W. A. Majewski, W. L. Meerts, and A. Dymanus, *Determination of the spin-rotation and hyperfine structure in the* $A^2\Sigma^+_{1/2}$ $v = 0$ *and* $v = 1$ *states of OH*, Chem. Phys. Lett. **94**, 25, 1983.

[104] J. J. T. ter Meulen, W. Ubachs, and A. Dumanus, *Observation of* ρ*-doublet transitions in OH(*$A^2\Sigma^+_{1/2}$*) by UV-microwave double resonance in a molecular beam*, Chem. Phys. Lett. **129**, 533 , 1986.

[105] C. Amiot and J. Verges, *Spin-rotation doubling in the NO* $A^2\Sigma^+$, $D^2\Sigma^+$, $E^2\Sigma^+$ *(v = 0) electronic states by emission fourier transform spectroscopy*, Chem. Phys. Lett. **66**, 570 , 1979.

[106] J. J. T. ter Meulen and A. Dymanus, *Beam-maser measurements of the ground-state transition frequencies of OH*, Astrophys. J. **172**, L21, 1972.

[107] G. Herzberg, *Molecular spectra and molecular structure: Spectra of diatomic molecules*, volume 1, Krieger Publishing Company, Malabar, Fl, USA, 1989.

[108] G. Dieke, *The structure of the so-called ultraviolet bands of water vapour*, Nature **115**, 194, 1925.

[109] W. Watson, *The origin of the satellites in the ultraviolet OH bands*, Nature **117**, 157, 1926.

[110] R. S. Mulliken, *Electronic states and band spectrum structure in diatomic molecules. VII.* ^{2}P→^{2}S *and* ^{2}S→^{2}P *transitions*, Phys. Rev. **32**, 388, 1928.

[111] D. Jack, *The band spectrum of water vapour. III*, Proc. Royal Soc. A **120**, 222, 1928.

[112] J. van Vleck, *Magnetic dipole radiation and the atmospheric absorption bands of oxygen*, Astrophys. J. **80**, 161, 1934.

[113] X. Yang and P. J. Dagdigian, *Observation of magnetic dipole transitions in the CN* $B\,^2\Sigma^+$-$A\,^2\Pi$ *band system*, J. Mol. Spec. **198**, 189 , 1999.

[114] M. Kirste, X. Wang, G. Meijer, K. B. Gubbels, A. van der Avoird, G. C. Groenenboom, and S. Y. T. van de Meerakker, *Communication: Magnetic dipole transitions in the OH* $A\,^2\Sigma^+ \leftarrow X\,^2\Pi$ *system*, J. Chem. Phys. **137**, 101102, 2012.

[115] P. Bunker, *Molecular symmetry and spectroscopy*, Academic Press, New York, NY, USA, 1979.

[116] W. L. Meerts and A. Dymanus, *Electric dipole moment of OH and OD by molecular beam electric resonance*, Chem. Phys. Lett. **23**, 45, 1973.

[117] B. J. Bichsel, M. A. Morrison, N. Shafer-Ray, and E. R. I. Abraham, *Experimental and theoretical investigation of the Stark effect for manipulating cold molecules: Application to nitric oxide*, Phys. Rev. A **75**, 023410, 2007.

[118] K.-E. Hallin, J. Johns, D. Lepard, A. Mantz, D. Wall, and K. N. Rao, *The infrared emission spectrum of* $^{14}N^{16}O$ *in the overtone region and determination of Dunham coefficients for the ground state*, J. Mol. Spec. **74**, 26 , 1979.

[119] G. Scoles (Editor), *Atomic and molecular beam methods*, volume 1 & 2, Oxford University Press, New York, NY, USA, 1988 & 1992.

[120] S. Y. T. van de Meerakker, N. Vanhaecke, H. L. Bethlem, and G. Meijer, *Transverse stability in a Stark decelerator*, Phys. Rev. A **73**, 023401, 2006.

[121] B. C. Sawyer, B. K. Stuhl, B. L. Lev, J. Ye, and E. R. Hudson, *Mitigation of loss within a molecular Stark decelerator*, Eur. Phys. J. D **48**, 197, 2008.

[122] J. J. Gilijamse, J. Küpper, S. Hoekstra, N. Vanhaecke, S. Y. T. van de Meerakker, and G. Meijer, *Optimizing the Stark-decelerator beamline for the trapping of cold molecules using evolutionary strategies*, Phys. Rev. A **73**, 063410, 2006.

[123] J. J. Gilijamse, S. Hoekstra, N. Vanhaecke, S. van de Meerakker, and

G. Meijer, *Loading Stark-decelerated molecules into electrostatic quadrupole traps*, Eur. Phys. J. D **57**, 33, 2010.

[124] A. Jacobs, K. Kleinermanns, H. Kluge, and J. Wolfrum, *OH($X\,^2\Pi$) state distribution from HNO_3 and H_2O_2 photodissociation at 193 nm*, J. Chem. Phys. **79**, 3162, 1983.

[125] L. Scharfenberg, *Crossed beam scattering with a Stark-decelerated molecular beam*, Ph. D. thesis, Technische Universität, Berlin, Deutschland, 2012.

[126] R. D. Livine and R. B. Bernstein, *Molecular reaction dynamics and chemical reactivity*, Oxford University Press, 1987.

[127] R. N. Zare and P. J. Dagdigian, *Tunable laser fluorescence method for product state analysis*, Science **185**, 739, 1974.

[128] M. P. Sinha, A. Schultz, and R. N. Zare, *Internal state distribution of alkali dimers in supersonic nozzle beams*, J. Chem. Phys. **58**, 549, 1973.

[129] G. Breit, *Quantum theory of dispersion (Continued). Parts VI and VII*, Rev. Mod. Phys. **5**, 91, 1933.

[130] R. N. Zare, *Molecular level-crossing spectroscopy*, J. Chem. Phys. **45**, 4510, 1966.

[131] C. H. Greene and R. N. Zare, *Determination of product population and alignment using Laser Induced Fluorescence*, J. Chem. Phys. **78**, 6741, 1983.

[132] P. J. Dagdigian, H. W. Cruse, A. Schultz, and R. N. Zare, *Product state analysis of BaO from the reactions Ba + $C0_2$ and Ba + O_2*, J. Chem. Phys. **61**, 4450, 1974.

[133] H. Lefebvre-Brion and R. W. Field, *The spectra and dynamics of diatomic molecules*, Academic Press, London, GB, 2004.

[134] J. Luque and D. R. Crosley, *LIFBASE: Database and spectral simulation program (Version 1.5)*, (1999).

[135] N. Vitanov, B. Shore, L. Yatsenko, K. BÃűhmer, T. Halfmann, T. Rickes, and K. Bergmann, *Power broadening revisited: Theory and experiment*, Opt. Commun. **199**, 117 , 2001.

[136] D. R. Guyer, L. Hüwel, and S. R. Leone, *Single collision ionŰmolecule reactions at thermal energy: Rotational and vibrational distributions from N^++CO→N+CO^+*, J. Chem. Phys. **79**, 1259, 1983.

[137] J. M. Hossenlopp, D. T. Anderson, M. W. Todd, and M. I. Lester, *State-to-state inelastic scattering from vibrationally activated OH-H_2 complexes*, J. Chem. Phys. **109**, 10707, 1998.

[138] D. R. Yarkoni, *A theoretical treatment of the predissociation of the individ-*

ual rovibronic levels of OH/OD($A\,^2\Sigma^+$), J. Chem. Phys. **97**, 1838, 1992.

[139] M. Collard, P. Kerwin, and A. Hodgson, *Two-photon resonance ionisation spectroscopy of OH/OD $D\,^2\Sigma^-$*, Chem. Phys. Lett. **179**, 422 , 1991.

[140] E. de Beer, M. P. Koopmans, C. A. de Lange, Y. Wang, and W. A. Chupka, *(2+1) resonance-enhanced multiphoton ionization–photoelectron spectroscopy of the OH radical*, J. Chem. Phys. **94**, 7634, 1991.

[141] J. M. Beames, F. Liu, M. I. Lester, and C. Murray, *Communication: A new spectroscopic window on hydroxyl radicals using UV + VUV resonant ionization*, J. Chem. Phys. **134**, 241102, 2011.

[142] A. Schiffman and D. W. Chandler, *Experimental measurements of state resolved, rotationally inelastic energy transfer*, Int. Rev. Phys. Chem. **14**, 371, 1995.

[143] D. Watanabe, H. Ohoyama, T. Matsumura, and T. Kasai, *Effect of mutual configuration between molecular orientation and atomic orientation in the oriented Ar* ($^3P_2$) + *oriented* $\mathrm{CF_3H}$ *reaction*, Phys. Rev. Lett. **99**, 043201, 2007.

[144] W. R. Dong, C. L. Xiao, T. Wang, D. X. Dai, X. M. Yang, and D. H. Zhang, *Transition-state spectroscopy of partial wave resonances in the F + HD reaction*, Science **327**, 1501, 2010.

[145] R. T. Skodje, D. Skouteris, D. E. Manolopoulos, S. H. Lee, F. Dong, and K. Liu, *Resonance-mediated chemical reaction: F+HD → HF+D*, Phys. Rev. Lett. **85**, 1206, 2000.

[146] L. Scharfenberg, K. B. Gubbels, M. Kirste, G. C. Groenenboom, A. van der Avoird, G. Meijer, and S. Y. T. van de Meerakker, *Scattering of Stark-decelerated OH radicals with rare-gas atoms*, Eur. Phys. J. D **65**, 189, 2011.

[147] S. Y. T. van de Meerakker, N. Vanhaecke, H. L. Bethlem, and G. Meijer, *Higher-order resonances in a Stark decelerator*, Phys. Rev. A **71**, 053409, 2005.

[148] D. M. Sonnenfroh and K. Liu, *Number density-to-flux transformation revisited: kinematic effects in the use of Laser Induced Fluorescence for scattering experiments*, Chem. Phys. Lett. **183**, 1991, 176.

[149] M. H. Alexander, *Quantum treatment of rotationally inelastic collisions involving molecules in* Π *electronic states: New derivation of the coupling potential*, Chem. Phys. **92**, 337, 1985.

[150] M. H. Alexander, *Rotationally inelastic collisions between a diatomic molecule in a* $^2\Pi$ *electronic state and a structureless target*, J. Chem. Phys. **76**, 5974, 1982.

[151] J. Kłos, F. Lique, and M. H. Alexander, *Temperature dependence of rotational excitation rate coefficients of OH($X\,^2\Pi$) in collision with He*, Chem. Phys. Lett. **445**, 12, 2007.

[152] H. S. Lee, A. B. McCoy, R. R. Toczyłowski, and S. M. Cybulski, *Theoretical studies of the math $\tilde{X}\,^2\Pi$ and $\tilde{A}\,^2\Sigma^+$ states of the He-OH and Ne-OH complexes*, J. Chem. Phys. **113**, 5736, 2000.

[153] HIBRIDON, *is a package of programs for the time-independent quantum treatment of inelastic collisions and photodissociation written by M. H. Alexander, D. E. Manolopoulos, H.-J. Werner, B. Follmeg, and others. More information and/or a copy of the code can be obtained from the website, http://www2.chem.umd.edu/groups/alexander/hibridon/hib43.*

[154] M. Kirste, L. Scharfenberg, J. Kłos, F. Lique, M. H. Alexander, G. Meijer, and S. Y. T. van de Meerakker, *Low-energy inelastic collisions of OH radicals with He atoms and D_2 molecules*, Phys. Rev. A **82**, 042717, 2010.

[155] P. J. Dagdigian, M. H. Alexander, and K. Liu, *The inelastic scattering of $^2\Pi$[case (b)] molecules and an understanding of the differing Λ doublet propensities for molecules of π vs π^3 orbital occupancy*, J. Chem. Phys. **91**, 839, 1989.

[156] A. D. Esposti, A. Berning, and H.-J. Werner, *Quantum scattering studies of the Λ doublet resolved rotational energy transfer of OH($X^2\Pi$) in collisions with He and Ar*, J. Chem. Phys. **103**, 2067, 1995.

[157] R. Cireasa, M. C. van Beek, A. Moise, and J. J. T. ter Meulen, *Inelastic state-to-state scattering of OH($^2\Pi_{3/2}, J = 3/2, f$) by HCl*, J. Chem. Phys. **122**, 074319, 2005.

[158] A. Moise, R. Cireasa, D. H. Parker, and J. J. T. ter Meulen, *Rotationally inelastic scattering of OH ($^2\Pi_{3/2}$, v = 0, J = 3/2, f) by HBr ($^1\Sigma$, v = 0, J<4)*, J. Chem. Phys. **125**, 204315, 2006.

[159] A. Moise, D. H. Parker, and J. J. T. ter Meulen, *State-to-state inelastic scattering of OH by HI: A comparison with OH-HCl and OH-HBr*, J. Chem. Phys. **126**, 124302, 2007.

[160] M. C. van Beek, K. Schreel, and J. J. T. ter Meulen, *Rotational excitation of OH in collisions with CO, N_2, and CO_2*, J. Chem. Phys. **109**, 1302, 1998.

[161] K. B. Gubbels, Q. Ma, M. H. Alexander, P. J. Dagdigian, D. Tanis, G. C. Groenenboom, A. van der Avoird, and S. Y. T. van de Meerakker, *Resonances in rotationally inelastic scattering of OH($X\,^2\Pi$) with helium and neon*, J. Chem. Phys. **136**, 144308, 2012.

[162] L. Scharfenberg, S. Y. T. van de Meerakker, and G. Meijer, *Crossed beam scattering experiments with optimized energy resolution*, Phys. Chem.

Chem. Phys. **13**, 8448, 2011.

[163] S. Stolte, *Reactive scattering studies on oriented molecules*, Ber. Bunsenges. Phys. Chem. **86**, 413, 1982.

[164] H. Jalink, D. H. Parker, and S. Stolte, *Polarized emission from the products of oriented reactants: The* $Ba+N_2O \rightarrow BaO^*+N_2$ *reaction*, J. Chem. Phys. **85**, 5372, 1986.

[165] M. A. Weibel, T. D. Hain, and T. J. Curtiss, *Hexapole-selected supersonic beams of reactive radicals:* CF_3, SiF_3, *SH, CH, and* C_2H, J. Chem. Phys. **108**, 3134, 1998.

[166] T. D. Hain, R. M. Moision, and T. J. Curtiss, *Hexapole state-selection and orientation of asymmetric top molecules:* CH_2F_2, J. Chem. Phys. **111**, 6797, 1999.

[167] T. D. Hain, M. A. Weibel, K. M. Backstrand, and T. J. Curtiss, *Rotational state-selection and orientation of OH and OD radicals by electric hexapole beam-focusing*, J. Phys. Chem. A **101**, 7674, 1997.

[168] L. V. Novakoski and G. M. McClelland, *Orientation of* $\mathrm{CHF_3}$ *desorbed and scattered from Ag(111): Measurements using electrostatic focusing*, Phys. Rev. Lett. **59**, 1259, 1987.

[169] E. W. Kuipers, M. G. Tenner, A. Kleyn, and S. Stolte, *Observation of steric effects in gas-surface scattering*, Nature **334**, 420, 1988.

[170] M. G. Tenner, E. W. Kuipers, A. W. Kleyn, and S. Stolte, *Steric effects in molecular adsorption*, J. Chem. Phys. **89**, 6552, 1988.

[171] E. W. Kuipers, M. G. Tenner, A. W. Kleyn, and S. Stolte, *Steric effects for NO/Pt(111) adsorption and scattering*, Phys. Rev. Lett. **62**, 2152, 1989.

[172] B. Berenbak, B. Riedmüller, S. Stolte, and A. Kleyn, *Impact site-dependent molecular anisotropy: NO scattering from Ru(0 0 0 1)-(1 × 1)H*, Chem. Phys. **301**, 309 , 2004.

[173] T. J. Curtiss and R. B. Bernstein, *Steric effect in the scattering of oriented* CH_3F *molecules by graphite (0001)*, J. Chem. Phys. **161**, 212 , 1989.

[174] T. J. Curtiss, R. S. Mackay, and R. B. Bernstein, *Steric effect in the scattering of hexapole-oriented beams of symmetric-top molecules by graphite(0001)*, J. Chem. Phys. **93**, 7387, 1990.

[175] F. M. H. Crompvoets, H. L. Bethlem, R. T. Jongma, and G. Meijer, *A prototype storage ring for neutral molecules*, Nature **411**, 174, 2001.

[176] F. M. H. Crompvoets, H. L. Bethlem, J. Küpper, A. J. A. van Roij, and G. Meijer, *Dynamics of neutral molecules stored in a ring*, Phys. Rev. A

69, 063406, 2004.

[177] C. E. Heiner, D. Carty, G. Meijer, and H. L. Bethlem, *A molecular synchrotron*, Nature Phys. **3**, 115, 2007.

[178] P. C. Zieger, S. Y. T. van de Meerakker, C. E. Heiner, H. L. Bethlem, A. J. A. van Roij, and G. Meijer, *Multiple packets of neutral molecules revolving for over a mile*, Phys. Rev. Lett. **105**, 173001, 2010.

[179] M. Kurahashi and Y. Yamauchi, *Production of a single spin-rotational state [(J,M) = (2,2)] selected molecular oxygen ($^3\Sigma_g^-$) beam by a hexapole magnet*, Review of Scientific Instruments **80**, 083103, 2009.

[180] M. Kurahashi and Y. Yamauchi, *State-selection of molecular oxygen ($^3\Sigma_g^-$) by a hexapole magnet and the inversion of population for the spin-rotational states*, Phys. Rev. A **78**, 022708, 2008.

[181] E. D. Courant and H. S. Snyder, *Theory of the alternating-gradient synchrotron*, Ann. Phys. **3**, 1, 1958.

[182] D. Kakati and D. C. Lainé, *Alternate-gradient focusing of a molecular beam of ammonia*, Phys. Lett. A **24**, 676, 1967.

[183] H. L. Bethlem, M. R. Tarbutt, J. Küpper, D. Carty, K. Wohlfart, E. A. Hinds, and G. Meijer, *Alternating gradient focusing and deceleration of polar molecules*, J. Phys. B **39**, R263, 2006.

[184] T. Junglen, T. Rieger, S. A. Rangwala, P. W. H. Pinkse, and G. Rempe, *Two-dimensional trapping of dipolar molecules in time-varying electric fields*, Phys. Rev. Lett. **92**, 223001, 2004.

[185] F. Filsinger, U. Erlekam, G. von Helden, J. Küpper, and G. Meijer, *Selector for structural isomers of neutral molecules*, Phys. Rev. Lett. **100**, 133003, 2008.

[186] S. Putzke, F. Filsinger, H. Haak, J. Küpper, and G. Meijer, *Rotational-state-specific guiding of large molecules*, Phys. Chem. Chem. Phys. **13**, 18962, 2011.

[187] F. Filsinger, *Manipulation of large neutral molecules with electric fields*, Ph. D. thesis, Radboud Universiteit, Nijmegen, The Netherlands, 2010.

[188] S. Putzke, *Alternating-gradient deceleration of large neutral molecules*, Ph. D. thesis, Freie Universität, Berlin, Deutschland, 2012.

[189] F. M. Crompvoets, H. L. Bethlem, and G. Meijer, *A storage ring for neutral molecules*, Adv. At., Mol., Opt. Phys. **52**, 209, 2006.

[190] J. Reuss, *State selection by nonoptical methods*, in G. Scoles (Editor), *Atomic and molecular beam methods*, volume 1, chapter 11, 276–292, Ox-

ford University Press, New York, NY, USA, 1988.

[191] R. T. Jongma, T. Rasing, and G. Meijer, *Two-dimensional imaging of metastable CO molecules*, J. Chem. Phys. **102**, 1925, 1995.

[192] R. W. Anderson, *Tracks of symmetric top molecules in hexapole electric fields*, J. Phys. Chem. A **101**, 7664, 1997.

[193] A. Gijsbertsen, *Towards a better understanding of inelastic atom-molecule collisions*, Ph. D. thesis, Vrije Universiteit, Amsterdam, The Netherlands, 2006.

[194] S. Y. Lee, *Accelerator physics*, World Scientific, Singapore, 2 edition, 2004.

[195] A. P. Banford, *The transport of charged particle beams*, London: E. & F. N. Spon Limited, 1966.

[196] F. M. H. Crompvoets, *A storage ring for neutral molecules*, Ph. D. thesis, Radboud Universiteit, Nijmegen, The Netherlands, 2005.

[197] C. E. Heiner, *A molecular synchrotron*, Ph. D. thesis, Radboud Universiteit, Nijmegen, The Netherlands, 2009.

[198] Comsol, *Multiphysics 3.2*, 2006, `http://www.comsol.com/products`.

[199] S. Weinreb, A. H. Barrett, M. L. Meeks, and J. C. Henry, *Radio observations of OH in the interstellar medium*, Nature **200**, 829, 1963.

[200] M. T. Vonk, J. A. Bacon, C. F. Giese, and W. R. Gentry, *Differential cross sections for rotationally inelastic collisions of NO($^2\Pi_{1/2}, j' \leq 2.5$) with NO($^2\Pi_{1/2}, j' \leq 2.5$) at a kinetic energy of 442 cm^{-1}*, J. Chem. Phys. **106**, 1353, 1996.

[201] P. Sharkey, I. R. Sims, I. W. M. Smith, P. Bocherel, and B. R. Rowe, *Pressure and temperature dependence of the rate constants for the association reaction of OH radicals with NO between 301 and 23 K*, J. Chem. Soc., Faraday Trans. **90**, 3609, 1994.

[202] J. R. Bochinski, E. R. Hudson, H. J. Lewandowski, G. Meijer, and J. Ye, *Phase space manipulation of cold free radical OH molecules*, Phys. Rev. Lett. **91**, 243001, 2003.

[203] C. Naulin, M. Costes, A. Benseddik, and G. Dorthe, *Kinematic effects on Laser Induced Fluorescence measurements performed in reactive crossed beam experiments*, Laser Chem. **8**, 283, 1988.

[204] S. Y. T. van de Meerakker, N. Vanhaecke, and G. Meijer, *Stark deceleration and trapping of OH radicals*, Annu. Rev. Phys. Chem. **57**, 159, 2006.

[205] C. D. Ball and F. C. D. Lucia, *Direct observation of Λ-doublet and hyperfine branching ratios for rotationally inelastic collisions of NO-He at 4.2 K*,

Chem. Phys. Lett. **300**, 227 , 1999.

[206] P. J. Dagdigian and M. H. Alexander, *Tensor cross sections and the collisional evolution of state multipoles: OH($X\,^2\Pi$)-Ar*, J. Chem. Phys. **130**, 094303, 2009.

[207] M. Kirste, X. Wang, H. C. Schewe, G. Meijer, K. Liu, A. van der Avoird, L. M. C. Janssen, K. B. Gubbels, G. C. Groenenboom, and S. Y. T. van de Meerakker, *Quantum-state resolved bimolecular collisions of velocity-controlled OH with NO radicals*, Science **338**, 1060, 2012.

[208] M. Nguyen, R. Sumathi, D. Sengupta, and J. Peeters, *Theoretical analysis of reactions related to the HNO_2 energy surface: OH + NO and H + NO_2*, Chem. Phys. **230**, 1, 1998.

[209] S. Y. T. van de Meerakker and G. Meijer, *Collision experiments with Stark-decelerated beams*, Faraday Discuss. **142**, 113, 2009.

[210] A. B. Meinel, *OH emission bands in the spectrum of the night sky 1.* **111**, 555, 1950.

[211] H. Weaver, D. R. W. Williams, N. H. Dieter, and W. T. Lum, *Observations of a strong unidentified microwave line and of emission from the OH molecule*, Nature **208**, 29, 1965.

[212] W. A. Baan and P. A. D. Wood, *Broad hydroxyl emission in IC 4553*, Astrophys. J. **260**, 49, 1982.

[213] T. D. Hain, M. A. Weibel, K. M. Backstrand, P. E. Pope, and T. J. Curtiss, *State-selected beams of hydroxyl radicals via electric hexapole focusing*, Chem. Phys. Lett. **262**, 723, 1996.

[214] D. P. Craig and T. Thirunamachandran, *Molecular quantum electrodynamics*, Academic, London, 1984.

[215] H.-J. Werner, P. J. Knowles, and et al., *MOLPRO: a package of ab initio programs, version 2010.1, URL http://www.molpro.net*, 2006.

[216] M. P. J. van der Loo and G. C. Groenenboom, *Theoretical transition probabilities for the OH Meinel system*, J. Chem. Phys. **126**, 114314, 2007.

[217] J. J. T. ter Meulen, *The low-field Zeeman splittings of the $^2\Pi_{3/2}$ (J=3/2) Λ-doublet states of OH*, Quaterly Report 27, Katholieke Universiteit Nijmegen 47, 1970.

[218] J. J. T. ter Meulen, *Beam maser investigation of population inversion mechanisms for interstellar hydroxyl radicals*, Ph. D. thesis, Radboud Universiteit, Nijmegen, The Netherlands, 1976.

[219] N. H. Nahler, J. D. White, J. LaRue, D. J. Auerbach, and A. M. Wodtke, *In-*

verse velocity dependence of vibrationally promoted electron emission from a metal surface, Science **321**, 1191, 2008.

[220] N. Vanhaecke, U. Meier, M. Andrist, B. H. Meier, and F. Merkt, *Multistage Zeeman deceleration of hydrogen atoms*, Phys. Rev. A **75**, 031402, 2007.

Akademischer Lebenslauf

For reasons of data protection, the *Akademischer Lebenslauf* is not included in the online version.

List of publications

[1] M. Kirste, B. G. Sartakov, M. Schnell, and G. Meijer, *Nonadiabatic transitions in electrostatically trapped Ammonia molecules*, Phys. Rev. A **79**, 051401, 2009.

[2] M. Kirste, L. Scharfenberg, J. Kłos, F. Lique, M. H. Alexander, G. Meijer, and S. Y. T. van de Meerakker, *Low-energy inelastic collisions of OH radicals with He atoms and D_2 molecules*, Phys. Rev. A **82**, 042717, 2010.

[3] L. Scharfenberg, K. B. Gubbels, M. Kirste, G. C. Groenenboom, A. van der Avoird, G. Meijer, and S. Y. T. van de Meerakker, *Scattering of Stark-decelerated OH radicals with rare-gas atoms*, Eur. Phys. J. D **65**, 189, 2011.

[4] M. Kirste, X. Wang, G. Meijer, K. B. Gubbels, A. van der Avoird, G. C. Groenenboom, and S. Y. T. van de Meerakker, *Communication: Magnetic dipole transitions in the OH $A\,^2\Sigma^+ \leftarrow X\,^2\Pi$ system*, J. Chem. Phys. **137**, 101102, 2012.

[5] M. Kirste, X. Wang, H. C. Schewe, G. Meijer, K. Liu, A. van der Avoird, L. M. C. Janssen, K. B. Gubbels, G. C. Groenenboom, and S. Y. T. van de Meerakker, *Quantum-state resolved bi-molecular collisions of velocity-controlled OH with NO radicals*, Science **338**, 1060, 2012.

[6] M. Kirste, H. Haak, G. Meijer, and S. Y. T. van de Meerakker, *A compact hexapole state-selector for NO radicals*, unpublished manuscript.

[7] X. Wang, M. Kirste, G. Meijer, and S. Y. T. van de Meerakker, *Stark deceleration of NO molecular beam*, Z. Phys. Chem., unpublished manuscript.